New approaches for coherent and incoherent implementation of x-ray phase contrast imaging

Fabio Alessio Vittoria

Department of Medical Physics and Biomedical Engineering

UCL

A thesis submitted for the degree of

Doctor of Philosophy

December, 2015

I, Fabio Alessio Vittoria confirm that the work presented in this thesis is my own. Where information has been derived from other sources, I confirm that this has been indicated in the thesis.

Signed:

Abstract

Two new x-ray imaging modalities exploiting the phase delay electromagnetic waves experience when travelling through matter are introduced in this work. The first, called beam tracking, allows the measurement of three different physical properties of an object: absorption, refraction and ultra-small-angle scattering. This is achieved by tracking the variations induced to a reference beam by a sample through a multi-Gaussian interpolation. Beam tracking can be implemented with both monochromatic, coherent radiation (available at e.g. synchrotron facilities) and polychromatic, incoherent radiation produced by standard laboratory sources. The nature of the three extracted signals allows the implementation of beam tracking in computed tomography, resulting in the three-dimensional reconstruction of the real and imaginary part of the sample refractive index, alongside its local scattering power. The second proposed method, called one dimensional ptychography, exploits the coherent properties of synchrotron radiation to retrieve the sample complex refractive index. The peculiar feature of this method is the strongly asymmetric beam used to illuminate the sample. Unlike standard ptychographic techniques, this enables scanning the sample in one direction only, which can lead to a possible reduction in exposure time when large field of

views are covered. At the same time, ptychographic, sub-pixel resolution can be obtained only in the scan direction, while pixel-limited resolution is obtained in the orthogonal one. Prior to the introduction of these methods, the theoretical foundations are laid down, and the development of a fast and effective simulation software allowing their implementation is described.

. . . a mia madre

Acknowledgements

My most sincere gratitude and appreciation goes to my primary supervisor Prof. Alessandro Olivo. During the last three years he has been an incredible source of ideas and inspiration, and his continuous encouragement and enthusiasm have been essential for the results achieved in this thesis. I would also like to thank my secondary supervisors Prof. Ian Robinson and Dr. Paul Diemoz; their help, suggestions and contribution have been of primary importance for this work. A special thank goes to Dr. Marco Endrizzi and to Dr. Liberato De Caro for the fruitful discussions, their precious help and their continuous interest in my project.

Many thanks go to the UCL X-Ray Phase Contrast group, in particular to Gibril Kallon and Dario Basta for their support and contribution during the laboratory experiments, to Anna Zamir and Charlotte Hagen for their suggestions and assistance in the tomographic data analysis, to Peter Munro, Tom Millard, Alberto Astolfo and Peter Modregger for the useful discussions and suggestions.

I would also like to thank the scientists of the beamline I13 at the Diamond Light Source for their support during the synchrotron experiments, and of the SYRMEP beamline at Elettra for the data provided.

Finally I would like to express my deepest thanks and gratitude to my wife Mariele, my mother Laura, my brother Tiziano and all my family for their invaluable support and encouragements.

Contents

List of Figures **11**

List of Tables **20**

Introduction **21**

1 X-ray wave-field in free space and matter **25**

1.1 X-ray propagation in free space 25

1.2 X-ray propagation in matter 30

1.2.1 Absorption and refraction 33

1.3 Coherence 37

2 X-ray imaging **41**

2.1 Absorption-based imaging 42

2.2 Phase-contrast imaging 43

2.2.1 Free-space propagation 43

2.2.2 Grating interferometry 45

2.2.3 Analyser based imaging 48

2.2.4 Edge Illumination 51

2.3 Coherent diffraction imaging 54

3 Wave optics simulation 58

3.1 Theoretical framework 60

3.2 Implementation 63

3.2.1 Sampling considerations 64

3.2.2 Circular convolution considerations 69

3.3 Comparison with another algorithm 72

3.4 Comparison with experimental data 74

3.5 Chapter conclusions 76

4 From edge illumination to beam tracking 77

4.1 Quantitative edge illumination 78

4.2 Virtual edge illumination 81

4.3 Beam tracking 84

5 Beam tracking: laboratory implementation 90

5.1 Experimental apparatus 91

5.2 Phase retrieval with polychromatic radiation 93

5.3 Comparison with other phase retrieval methods 100

5.4 Simulation results 105

5.5 Experimental results 107

5.6 Discussion 111

6 Beam tracking: tomographic implementation 112

6.1 Mathematical background 113

6.2 Beam tracking tomography 116

6.3 Experimental results . . . 119
6.4 Discussion . . . 123

7 One-dimensional ptychography **125**
7.1 Preliminary considerations . . . 126
7.2 Reconstruction algorithm . . . 128
7.3 Simulations . . . 133
7.4 Experiments . . . 136
7.5 Spatial resolution . . . 142
7.6 Discussion . . . 146

Conclusions **148**

References **152**

List of Figures

1.1 Scheme of the reference frame used to calculate the effect of propagation in free space on electromagnetic waves. 30

1.2 Schematic representation of three beamlets travelling in free space (a), and of the effect of refraction caused by a sample (b). 35

1.3 Frame of reference for two waves emitted from $\mathbf{x}'_1$ and $\mathbf{x}'_2$, and superimposing in $\mathbf{x}$. 38

2.1 Schematic diagram of an absorption-based imaging system. 42

2.2 Schematic diagram of a free-space propagation imaging system. . 44

2.3 Schematic diagram of a grating-based imaging system. 46

2.4 Schematic diagram of a Talbot-Lau imaging system. 48

2.5 Schematic diagram of an analyser-based imaging system. 50

2.6 Schematic diagram of an edge illumination imaging system. 53

2.7 Schematic diagram of a coherent diffraction imaging system. . . . 55

3.1 Schematic diagram of an edge illumination setup. 60

3.2 Modulus of $\hat{H}_{z,eff}(\xi)$: the blue curve is calculated numerically, while the green curve is calculated analytically with the approximation discussed in the text. Parameters used in the simulation: $z = 2$ m, $L = 2$ mm, $\lambda = 0.31$ Å($E = 40$ KeV). 65

3.3 Simulations of profiles of a polypropylene wire with an edge illumination system, obtained with different numbers of sampling points: $\delta x_{blue} = 3.4$ nm is derived in accordance with Eq. (3.24), $\delta x_{green} = 15\,\delta x_{blue}$, $\delta x_{red} = 30\,\delta x_{blue}$. Only the first simulation (blue) provides correct results. Parameters used in the simulation: monochromatic Gaussian distributed source ($FWHM = 60$ μm, $E = 30$ KeV); $z_1 = 1.6$ m, $z_2 = 0.4$ m; sample mask with 12 μm apertures and a period of 80 μm; detector mask with 20 μm apertures and a period of 100 μm; 50% illuminated fraction; pixel size = 100 μm; wire diameter = 140 μm; number of dithering steps (number of sub-pixel sample displacements) = 10 (each step = 8 μm). 69

3.4 Simulations of profiles of a polypropylene wire with an edge illumination system, obtained using different dimensions for the sampled space. The blue curve is calculated considering a sampled space $L = L_D + R_{M1} + R_{Sr}$, which leads to correct results; the green curve is calculated with a sampled space $L = L_D$, which causes errors in the simulated profile. Parameters used in the simulation: monochromatic Gaussian distributed source ($FWHM = 1$ μm, E = 30 KeV); $z_1 = 100$ m, $z_2 = 0.1$ m; sample mask with 20 μm apertures and a period of 120 μm; detector mask with 20 μm apertures and a period of 120 μm; 50% illuminated fraction; pixel size = 120 μm; wire diameter = 160 μm; number of dithering steps = 10 (each step = 12 μm). 71

3.5 Comparison between simulated results obtained with the proposed algorithm (blue curves) and the one described in [1] (green curves). (a) Polypropylene wire: monochromatic Gaussian distributed source ($FWHM = 60$ μm, $E = 30$ KeV); $z_1 = 1.6$ m, $z_2 = 0.4$ m; sample mask with 20 μm apertures and 80 μm period; detector mask with 50 μm apertures and 100 μm period; 50% illuminated fraction; pixel size = 100 μm; wire diameter = 260 μm; number of dithering steps = 40 (each step = 2 μm). (b) Aluminium wire: monochromatic Gaussian distributed source ($FWHM = 1$ μm, E = 20 KeV); $z_1 = 0.1$ m, $z_2 = 1$ m; sample mask with 3.4 μm apertures and 13.6 μm period; detector mask with 75 μm apertures and 150 μm period; 50% illuminated fraction; pixel size = 150 μm; wire diameter = 14 μm; dithering steps = 40 (each step = 0.34 μm). 72

3.6 Ratio between the computational times for the algorithm described in [1] and the one presented here, as a function of the sample dimension. Parameters used in the simulation: monochromatic Gaussian distributed source ($FWHM$ = 60 μm, E = 30 KeV); z_1 = 1.6 m, z_2 = 0.4 m; sample mask with 40 μm apertures and 80 μm period; detector mask with 50 μm apertures and 100 μm period; 50% illuminated fraction; pixel size = 100 μm; polypropylene wire sample; dithering steps = 5 (each step = 16 μm). 73

3.7 Image of different wires acquired with synchrotron radiation using the edge illumination method. 74

3.8 Comparison between experimental data (intensity profiles along the black vertical line in Fig. 3.7) and simulation results. 74

4.1 Schematic diagram of an edge illumination setup. 81

4.2 Intensity pattern produced by the pre-sample slit and acquired with the high resolution detector without (a) and with (b) a sample present in the beam. The refraction induced by the sample is evident in the right part of the image in (b). 82

4.3 Refraction signals of a PEEK monofilament immersed in water using the real (a) and virtual (b) edge configurations, and the beam tracking (c) method. In (d), (e) and (f) a vertical profile extracted from each image is compared to the theoretical refraction angle. . 83

4.4 Comparison between experimental and interpolated beam intensity profile. 86

4.5 Absorption (a) refraction (b) and scattering (c) images of a bamboo wood slice obtained with the beam tracking method. 87

4.6 Colour rendering of the three signals in Fig. 4.5. Red represents absorption, blue the absolute value of refraction and green scattering. 88

5.1 Schematic diagram of the beam tracking setup implemented with a laboratory source. 91

5.2 Intensity pattern produced by the absorbing mask and acquired by the detector without (a) and with (b) a sample present in the beam. The period of the intensity pattern is equal to 4 pixels (200 μm). 92

5.3 Absorption ($-\log T$) (a,d), refraction (R/z_3) (μrad) (b,e), and scattering (σ_S^2/z_3^2) (μrad^2) (c,f) signals retrieved from the simulation. The sample is a glass sphere of 2.56 mm diameter for the profiles (a-c), while for (d-f) the same sphere is convolved with a Gaussian function of $\sigma = 50$ μm. The retrieved signal for the Fourier-analysis, Gaussian interpolation, and its modified version are shown in red (circular markers), blue (triangular markers), and green (square markers), respectively; while the expected signal is shown in black. 106

5.4 Absorption ($-\log T_1$) (a), refraction (R/z_3) (μrad) (b), and scattering (σ_S^2/z_3^2) (μrad^2) (c) signals retrieved from glass spheres using the proposed method. (d), (e) and (f) show the same signals retrieved using Fourier-analysis [2]. In (g), (h) and (i) line profiles are extracted from the images (blue line and triangular marker for our method, red line and circular marker for Fourier-analysis), and compared with the expected value (black line). 108

5.5 Absorption ($-\log T$) (a), refraction (R/z_3) (μrad) (b), and scattering (σ_S^2/z_3^2) (μrad^2) (c) signals retrieved from the leg of a beetle. 109

5.6 Absorption ($-\log T$) (a), refraction (R/z_3) (μrad) (b), and scattering (σ_S^2/z_3^2) (μrad^2) (c) signals retrieved from a wood section. . 110

6.1 Frame of reference for a rotating object in a tomographic configuration. 113

6.2 Schematic diagram of the experimental setup. 116

6.3 Intensity pattern produced by the absorbing mask and acquired by the high resolution detector without (a) and with (b) a sample present in the beam. The period of the intensity pattern is equal to 85 μm. 120

6.4 Reconstructed slices of (a) β and (b) δ from a test object made of three wires of different materials. In (c) the mean values calculated in the central region of each wire are compared with the theoretical ones (black). The error bars for the experimental data are equal to ± 1 standard deviation, while an error of $\pm 5\%$ is assumed on the theoretical values to account for potential impurities and density variations. Resolution is reduced by approximately a factor of 2 compared to the intrinsic resolution of the system (≈ 10 μm, equal to a mask aperture), due to the Gaussian filter applied to each projection to reduce noise in the final reconstruction (see text). . 121

6.5 Reconstructed slices of β (a), δ (b), and σ_s^2 (c) from a wood sample, and volume renderings of β and δ (d), β and σ_s^2 (e), δ and σ_ϕ^2 (f). The volume renderings has been sectioned to show three inner planes of the sample. Resolution is reduced by approximately a factor of 3 for (a) and (b), and 4 for (c), compared to the intrinsic resolution of the system (≈ 10 μm, equal to a mask aperture), due to the Gaussian filter applied to each projection to reduce noise in the final reconstruction (see text). 122

7.1 Schematic diagram of 1D-PIE methods. 128

7.2 Simulated sample amplitude (a) and phase shift (b) maps. Simulated beam amplitude (c) and phase (d) maps. Retrieved sample (e, f) and beam (g, h) in the case of 1% Gaussian noise. Retrieved sample (i, l) and beam (m, n) in the case of 10% Gaussian noise. All the original photographs used to simulate the sample amplitude and phase shift maps were taken by the author. 134

7.3 Evolution of the RMS error ϵ_n. The solid (blue) line refers to the case of 1% noise, the dashed (black) line refers to the case of 10% noise. 136

7.4 Reconstructed (dotted, green) and theoretical (solid, black) phase shift of a PEEK monofilament in water. 137

7.5 Reconstructed results of a spider leg. Retrieved sample amplitude (a) and phase shift (b) maps. Retrieved beam amplitude (c) and phase (d) maps. The lateral inserts show an enlargement of the regions in the white squares; red arrows show some small details (≈5μm) visible in the reconstructed images, and how these appear sharper in the phase image. 138

7.6 Evolution of the RMS error E_n. 139

7.7 Logarithm of the intensity pattern recorded by the detector using a thin wood section to increase the beam inhomogeneity without (a) and with (b) a sample present in the beam. 140

7.8 Reconstructed phase shift of the resolution star pattern. 141

7.9 (a) Division of the Fourier space for the calculation of the FRC curves. FRC curves (solid) and 2σ criterion (dashed) for 1% noise along x (b) and y (c), and for 10% noise along x (d) and y (e). . . 143

7.10 Mean radial Fourier spectrum of the spider leg transmission function (Fig. 7.5) along the x (a) and y (b) directions (solid lines) and relative thresholds (dashed lines) used to estimate the experimental resolution. 144

7.11 (a) Central region of the reconstructed image. Circles corresponding to a semi-period of the star pattern of 0.45 μm and 2.6 μm are shown, representing the final resolution in the x and y direction, respectively. Profiles of the phase modulation in the final reconstruction along the x (b) and y (c) directions (solid lines) and relative thresholds (dashed lines), used to estimate the experimental resolution, as a function of the semi-period of the star pattern. 145

List of Tables

3.1 Properties of wires highlighted in Fig. 3.7. PEEK stands for polyetheretherketone. The boron wire contains a thin tungsten core with an estimated diameter of 14 μm. 75

7.1 Estimated resolution values of the reconstructed sample transmission function for the simulated case, using the FRC and the 2σ criterion. 143

7.2 Estimated resolution values of the reconstructed sample transmission function for the experimental case. 146

Introduction

The term *x-ray* is used to identify a part of the electromagnetic spectrum characterised by small wavelength ($\lesssim$ 10 nm) and high energy ($\gtrsim$ 100 eV), just above the ultraviolet range. Depending on their energy, x-rays are usually classified as *soft* (energy $\lesssim$ 5 keV) and *hard* (energy $\gtrsim$ 5 keV). Photons belonging to the high energy part of the hard x-ray spectrum ($\gtrsim$ 100 keV) start on occasions to be referred to as *gamma rays.* The distinction between x-rays and gamma rays can be done with reference to their origin: while x-rays are generated by electrons, gamma rays are emitted by atomic nuclei, as the product of nuclear reactions. Hard x-rays are characterised by a large penetration depth in matter, which makes them an excellent tool to study and investigate the internal structures of materials in a large variety of fields. One of the main applications of hard x-rays is imaging. As they travel through matter x-rays are partially absorbed, and the amount of absorbed radiation depends on the chemical composition, density and thickness of the traversed material. By sending an x-ray beam trough a sample and measuring the fraction of transmitted radiation, in the plane perpendicular to the x-ray propagation direction, it is possible to visualise the internal structures of the sample on the basis of their different absorption properties. X-ray absorption imaging has been performed along this same principle since x-rays

were discovered in 1895 by Röntgen, with innovations mainly coming from technological improvement of sources and detectors. One of the main limitations of x-ray imaging is low contrast when light-absorbing materials are imaged. In this context, an important example is the low contrast obtained from soft tissue (i.e. muscles, cartilage) in medical imaging. An other important limitation is the radiation damage induced by x-rays to biological specimens. Due to their high energy x-rays can ionize atoms along their path, which can lead to biological damage. It is important to note that these two problems are strictly related: to reduce the radiation damage, less radiation should be absorbed by the sample, but this would affect the very mechanism at the basis of image formation and therefore reduce image quality.

In the last decades, different approaches have been developed to overcome the above problems. The common feature of these approaches is that they are not based on x-rays absorption as the main mechanism to generate contrast. X-rays, in fact, are not only absorbed in matter, but also refracted (i.e. deflected). Refraction is caused by variations in the phase shift that electromagnetic waves, like x-rays, experience when travelling in matter. For this reason this area of research is called *x-ray phase contrast imaging* (XPCi). XPCi techniques have greatly improved the performance of x-ray imaging, and they are currently implemented in several fields of research. Despite the important benefits brought by XPCi, there are still some important limitations that need to be addressed. The main limitation regards the implementation of XPCi methods with laboratory sources. XPCi performance, in fact, usually depends strongly on a particular feature of x-ray radiation called *coherence*. Coherent x-ray radiation is available at synchrotron facilities, or through microfocal x-ray sources. While synchrotron facilities are

large in size, usually hundreds of meters in diameter, and expensive, microfocal sources are characterized by a very low x-ray flux. In both cases, practical implementation in fields such as medical imaging or security is prevented. For this reason, one of the main aims in XPCi has become the development of techniques which could be implemented in x-ray imaging systems already in use for practical applications like the above. At the same time, more synchrotron facilities are being built and improved around the world, resulting in a fast growth of their performance. It is therefore still of primary importance to continue the development of new imaging techniques that can exploit the peculiar features offered by these sources, especially coherence.

The work presented here tackles both these aspects of XPCi. Starting from the underlying physical principles of an established XPCi technique, called *edge illumination*, two new approaches are developed, namely *beam tracking* and *one-dimensional ptychography*. Advantages and problems of these methods, together with strategies to further improve their performance, will be presented and discussed. In the first chapter, the wave theory of x-ray propagation in free space and matter is introduced, together with the concept of coherence. This will provide the basis for the theoretical considerations of the following chapters. The second chapter is focused on the description of existing x-ray imaging methods, with particular emphasis on XPCi. In the third chapter, a rigorous wave-optics simulation, and the problems arising from its numerical implementation, are discussed. In the forth chapter the beam tracking approach is presented in its first implementation, with synchrotron radiation. The fifth chapter is focused on the laboratory implementation of beam tracking, while its tomographic implementation, with synchrotron radiation, will be presented in the sixth chapter. Finally

one-dimensional ptychography is described in the seventh and last chapter.

1

X-ray wave-field in free space and matter

In this chapter elements of the classical theory of electromagnetic waves will be introduced. In particular we will focus our attention on the description of waves propagating in free-space and in matter, and on the concept of coherence. This subject is discussed in more detail in several textbooks [3, 4, 5], while here only the main results will be presented.

1.1 X-ray propagation in free space

The starting point to describe the evolution of electromagnetic waves in free space are the Maxwell equations, expressed here in the International System of Units

(SI), in vacuum and away from charges and currents [3]:

$$\nabla \cdot \mathbf{E}(x, y, z, t) = 0; \tag{1.1}$$

$$\nabla \cdot \mathbf{B}(x, y, z, t) = 0; \tag{1.2}$$

$$\nabla \times \mathbf{E}(x, y, z, t) = -\frac{\partial}{\partial t}\mathbf{B}(x, y, z, t); \tag{1.3}$$

$$\nabla \times \mathbf{B}(x, y, z, t) = \epsilon_0 \mu_0 \frac{\partial}{\partial t}\mathbf{E}(x, y, z, t). \tag{1.4}$$

$\mathbf{E}$ is the electric field, $\mathbf{B}$ the magnetic induction, ϵ_0 the electrical permittivity in vacuum, μ_0 the magnetic permeability in vacuum, (x, y, z) Cartesian coordinates in three-dimensional space, and t time. Bold letters are used to indicate vectors.

Applying the curl operator to Eq. 1.3, and using the operator identity $\nabla \times \nabla \times = \nabla\nabla \cdot -\nabla^2$ and Eqs. 1.1 and 1.4 in the obtained expression, it is possible to derive the following equation:

$$\left(\epsilon_0 \mu_0 \frac{\partial^2}{\partial t^2} - \nabla^2\right)\mathbf{E}(x, y, z, t) = 0. \tag{1.5}$$

Using a similar line of reasoning, one can obtain an identical equation for the magnetic induction $\mathbf{B}$:

$$\left(\epsilon_0 \mu_0 \frac{\partial^2}{\partial t^2} - \nabla^2\right)\mathbf{B}(x, y, z, t) = 0. \tag{1.6}$$

Equations 1.5 and 1.6 are the d'Alembert wave equations, and describe waves propagating at speed $c = 1/\sqrt{\epsilon_0 \mu_0}$. In the presented forms, Eqs. 1.5 and 1.6 are vector equations, however, each component of the electric field and magnetic induction satisfies a scalar form of the d'Alambert wave equation. It is therefore

possible to describe the electromagnetic field in free space by means of a single scalar wave equation:

$$\left(\frac{1}{c^2}\frac{\partial^2}{\partial t^2} - \nabla^2\right)\Psi(x, y, z, t) = 0, \tag{1.7}$$

where Ψ characterizes the electromagnetic field.

Let us consider, now, a monochromatic wave, i.e. a wave whose amplitude varies sinusoidally in time with a fixed frequency ω:

$$\Psi(x, y, z, t) = \psi_\omega(x, y, z)\exp(-i\omega t). \tag{1.8}$$

Substituting Eq. 1.8 in Eq. 1.7, we obtain, for the spatial component ψ_ω of the electromagnetic field Ψ, the following time-independent equation:

$$\left(\nabla^2 + k^2\right)\psi_\omega(x, y, z) = 0, \tag{1.9}$$

with $k = \omega/c$. Equation 1.9 is known as the Helmholtz equation. Let us assume a monochromatic wave is propagating in a portion of free space in the z direction, and that its wave function is known for each point of the plane $z = 0$, i.e. $\psi_\omega(x, y, 0)$ is known for each value of x and y. The Helmholtz equation can be used to determine the wave function $\psi_\omega(x, y, z)$ in any other plane. $\psi_\omega(x, y, z)$ can be expressed in terms of a two-dimensional Fourier integral:

$$\psi_\omega(x, y, z) = \frac{1}{2\pi}\iint \check{\psi}_\omega(k_x, k_y, z)\exp\left[i(k_x x + k_y y)\right]dk_x dk_y, \tag{1.10}$$

where $\check{\psi}_\omega(k_x, k_y, z)$ denotes the two dimensional Fourier transform of $\psi_\omega(x, y, z)$

with respect to x and y, and k_x, k_y are the Fourier space variable, conjugate to x and y. Substituting Eq. 1.10 in the Helmholtz equation 1.9, we obtain:

$$\frac{\partial^2}{\partial z^2}\check{\psi}_\omega(k_x, k_y, z) = -(k^2 - k_x^2 - k_y^2)\check{\psi}_\omega(k_x, k_y, z), \tag{1.11}$$

which has the following solution:

$$\check{\psi}_\omega(k_x, k_y, z) = \check{\psi}_\omega(k_x, k_y, 0) \exp\left(iz\sqrt{k^2 - k_x^2 - k_y^2}\right). \tag{1.12}$$

The electromagnetic field $\psi_\omega(x, y, z)$ can therefore be expressed as:

$$\psi_\omega(x, y, z) = \mathcal{F}^{-1}\left\{\mathcal{F}\left[\psi_\omega(x, y, 0)\right] \exp\left(iz\sqrt{k^2 - k_x^2 - k_y^2}\right)\right\}, \tag{1.13}$$

where $\mathcal{F}$ indicates the two dimensional Fourier transform with respect to x and y.

To obtain Eq. 1.13 we expressed the wave field $\psi_\omega(x, y, z)$ in terms of its two dimensional Fourier transform $\check{\psi}_\omega(k_x, k_y, z)$. $\psi_\omega(x, y, z)$ can also be expanded in its three dimensional Fourier transform:

$$\psi_\omega(x, y, z) = \frac{1}{(2\pi)^{3/2}} \iiint \widetilde{\psi}_\omega(k_x, k_y, k_z) \times \exp\left[i(k_x x + k_y y + k_z z)\right] dk_x dk_y dk_z. \tag{1.14}$$

The last equation is a solution of the Helmholtz equation if $\widetilde{\psi}_\omega(k_x, k_y, k_z) = 0$ for every vector (k_x, k_y, k_z) for which $k^2 \neq k_x^2 + k_y^2 + k_z^2$. A physical interpretation of Eq. 1.14 is that each wave function $\psi_\omega(x, y, z)$ can be seen as a superposition of plane waves $\exp\left[i(k_x x + k_y y + k_z z)\right]$ with different amplitude $\widetilde{\psi}_\omega(k_x, k_y, k_z)$.

$\psi_\omega(x, y, z)$ is therefore a solution of the Helmholtz equation if all its plane wave components that are different from 0 satisfy $k^2 = k_x^2 + k_y^2 + k_z^2$. For a plane wave, the vector (k_x, k_y, k_z) indicates its propagation direction; if we consider only waves whose propagation direction makes a small angle with respect to the z axis, then $k_z^2 \gg k_x^2 + k_y^2$ and $k_x^2 + k_y^2 \ll k^2$. In this situation we can do the following approximation:

$$\sqrt{k^2 - k_x^2 - k_y^2} \approx k - \frac{k_x^2 + k_y^2}{2k}, \tag{1.15}$$

and Eq. 1.13 becomes:

$$\psi_\omega(x, y, z) = \exp(ikz)\mathcal{F}^{-1}\left\{\mathcal{F}\left[\psi_\omega(x, y, 0)\right]\exp\left[-iz\frac{k_x^2 + k_y^2}{2k}\right]\right\}. \tag{1.16}$$

Equation 1.15 is referred to as *paraxial approximation.* Using the convolution theorem, it is possible to rewrite Eq. 1.16 as:

$$\psi_\omega(x, y, z) = \psi_\omega(x, y, 0) * H_z(x, y), \tag{1.17}$$

where $*$ indicates the convolution operation and:

$$H_z(x, y) = \frac{\exp(ikz)}{i\lambda z}\exp\left[\frac{ik}{2z}(x^2 + y^2)\right], \tag{1.18}$$

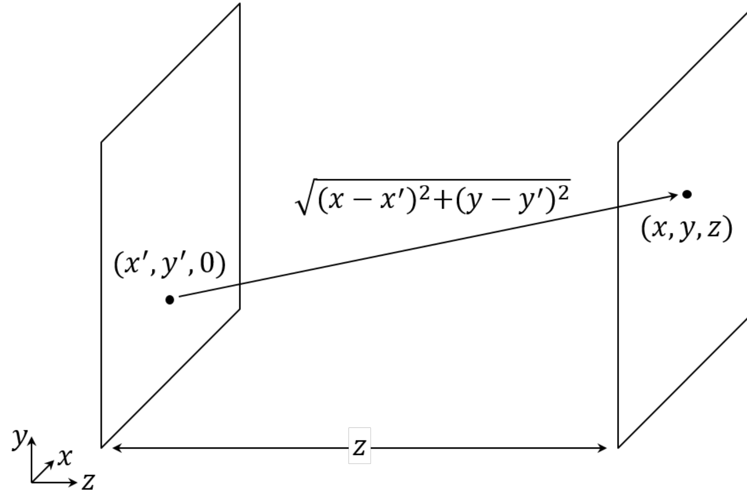

Figure 1.1: Scheme of the reference frame used to calculate the effect of propagation in free space on electromagnetic waves.

or explicitly as:

$$\psi_\omega(x, y, z) = \frac{\exp(ikz)}{i\lambda z} \iint \psi_\omega(x', y', 0) \times \exp\left\{\frac{ik}{2z}[(x-x')^2 + (y-y')^2]\right\} dx'dy'. \quad (1.19)$$

Eqation 1.19 is called *Fresnel diffraction integral*, and describe the wave propagation in free space in the paraxial approximation. Equations 1.13, 1.17 and 1.19 allow the calculation of the electromagnetic field at any plane (x, y) at a distance z from the origin (Fig. 1.1), provided that the field $\psi_\omega(x, y, 0)$ in the plane $z = 0$ is known.

1.2 X-ray propagation in matter

To describe how electromagnetic waves, and in particular x-rays, interact with matter we need to consider Maxwell equations in matter, away from charges and

currents [3]:

$$\nabla \cdot [\epsilon(x,y,z)\mathbf{E}(x,y,z,t)] = 0; \tag{1.20}$$

$$\nabla \cdot \mathbf{B}(x,y,z,t) = 0; \tag{1.21}$$

$$\nabla \times \mathbf{E}(x,y,z,t) = -\frac{\partial}{\partial t}\mathbf{B}(x,y,z,t); \tag{1.22}$$

$$\nabla \times \left[\frac{\mathbf{B}(x,y,z,t)}{\mu(x,y,z)}\right] = \epsilon(x,y,z)\frac{\partial}{\partial t}\mathbf{E}(x,y,z,t). \tag{1.23}$$

$\epsilon(x,y,z)$ and $\mu(x,y,z)$ are the electrical permittivity and the magnetic permeability of the material, respectively. In writing the above equations we implicitly assumed that the material is linear and isotropic and that its electrical permittivity and magnetic permeability are constant in time. Let us further assume that the material is non-magnetic, i.e. $\mu(x,y,z) = \mu_0$, and consider the following vector identity:

$$\nabla \cdot [\epsilon(x,y,z)\mathbf{E}(x,y,z,t)] = \epsilon(x,y,z)\nabla \cdot \mathbf{E}(x,y,z,t) + [\nabla\epsilon(x,y,z)] \cdot \mathbf{E}(x,y,z,t). \tag{1.24}$$

If $\epsilon(x,y,z)$ is slowly varying over length scales comparable to the wavelength of the radiation, the last term in the above equations can be neglected. Following the same procedure described in the previous section it is now possible to derive a single scalar wave equations to describe the electromagnetic field in a medium:

$$\left(\epsilon(x,y,z)\mu_0\frac{\partial^2}{\partial t^2} - \nabla^2\right)\Psi(x,y,z,t) = 0. \tag{1.25}$$

Considering a monochromatic wave $\Psi(x, y, z, t) = \psi_\omega(x, y, z) \exp(-i\omega t)$, and substituting it in Eq.1.25, we obtain the following inhomogeneous Helmholtz equation:

$$\left(\nabla^2 + n^2(x, y, z)k^2\right) \psi_\omega(x, y, z) = 0, \tag{1.26}$$

where $n(x, y, z) = c\sqrt{\epsilon(x, y, z)\mu_0}$ is the refractive index of the material.

Within the paraxial approximation, we can consider solutions of Eq. 1.26 of the form:

$$\psi_\omega(x, y, z) = \bar{\psi}_\omega(x, y, z) \exp(ikz). \tag{1.27}$$

This equation, in fact, can be seen as a plane wave $\exp(ikz)$ travelling in the z direction, perturbed by an envelope $\bar{\psi}_\omega(x, y, z)$, which will be assumed to vary slowly in z. Substituting Eq. 1.27 in Eq. 1.26 we obtain:

$$\left\{2ik\frac{\partial}{\partial z} + \nabla_\perp^2 + \frac{\partial^2}{\partial z^2} + k^2\left[n^2(x, y, z) - 1\right]\right\} \bar{\psi}_\omega(x, y, z) = 0, \tag{1.28}$$

where $\nabla_\perp^2 = \partial^2/\partial x^2 + \partial^2/\partial y^2$. In the paraxial approximation, $\bar{\psi}_\omega(x, y, z)$ varies slowly in z, compared to x and y, allowing us to neglect the term $\partial^2/\partial z^2$. The term $\nabla_\perp^2$ is responsible for variations along the x and y directions of the wave function $\bar{\psi}_\omega(x, y, z)$, during its propagation along the z direction. If, however, the object is thin enough, those effects can be neglected. This is called the *thin object approximation.* The previous equation becomes:

$$\frac{\partial}{\partial z}\bar{\psi}_\omega(x, y, z) = \frac{k}{2i}\left[1 - n^2(x, y, z)\right] \bar{\psi}_\omega(x, y, z), \tag{1.29}$$

which has the following solution:

$$\bar{\psi}_\omega(x,y,z) = \exp\left\{\frac{k}{2i}\int_0^z \left[1 - n^2(x,y,z')\right] dz'\right\} \bar{\psi}_\omega(x,y,0). \tag{1.30}$$

For x-rays, the refractive index is usually expressed in the form $n(x,y,z) = 1 - \delta(x,y,z) + i\beta(x,y,z)$, where δ and β are real, positive quantities, both much smaller than unity. It is therefore possible to approximate $1 - n^2(x,y,z') \approx 2[\delta(x,y,z) - i\beta(x,y,z)]$ and write:

$$\bar{\psi}_\omega(x,y,z) = \exp\left\{-ik\int_0^z \left[\delta(x,y,z') - i\beta(x,y,z')\right] dz'\right\} \bar{\psi}_\omega(x,y,0). \tag{1.31}$$

A part from a constant phase factor, the field in the plane after the sample can be expressed as the field on the plane before the sample multiplied by a complex transmission function $T(x,y)$:

$$T(x,y) = \exp\left[-ik\int_0^z \delta(x,y,z')dz'\right] \exp\left[-k\int_0^z \beta(x,y,z')dz'\right]. \tag{1.32}$$

The object will therefore introduce a phase shift in the incoming wave equal to $\phi(x,y) = k\int_0^z \delta(x,y,z')dz'$, and reduce its amplitude by a factor dependent on $M(x,y) = k\int_0^z \beta(x,y,z')dz'$.

1.2.1 Absorption and refraction

We will now interpret the equations derived in the previous sections in terms of two "simple" physical phenomena that are usually encountered in the ray theory of optics: absorption and refraction. Let us consider an object in the plane $z = 0$ illuminated by a paraxial wave propagating in the z direction. Let $\psi_0^i(x,y)$ be

the field on the plane $z = 0$ incident on the object. The field observed on the plane $z = D$, after the object, will be:

$$\psi_D^t(x,y) = \frac{\exp(ikD)}{i\lambda D} \iint \psi_0^i(x',y')T(x',y') \times \exp\left\{\frac{ik}{2D}[(x-x')^2 + (y-y')^2]\right\} dx'dy', \quad (1.33)$$

where $T(x,y) = \exp[-M(x,y) - i\phi(x,y)]$ is the complex transmission function of the object. The domain of integration in Eq. 1.33 can be divided into a series of squares A_n, centred around (x'_n, y'_n), so that:

$$\psi_D^t(x,y) = \sum_n \psi_{D,n}^t(x,y), \quad (1.34)$$

with:

$$\psi_{D,n}^t(x,y) = \frac{\exp(ikD)}{i\lambda D} \iint_{A_n} \psi_0^i(x',y')T(x',y') \times \exp\left\{\frac{ik}{2D}[(x-x')^2 + (y-y')^2]\right\} dx'dy'. \quad (1.35)$$

The propagated field, on the same plane, without the object, would instead be:

$$\psi_{D,n}^i(x,y) = \frac{\exp(ikD)}{i\lambda D} \iint_{A_n} \psi_0^i(x',y') \times \exp\left\{\frac{ik}{2D}[(x-x')^2 + (y-y')^2]\right\} dx'dy'. \quad (1.36)$$

$\psi_{D,n}^t(x,y)$ and $\psi_{D,n}^i(x,y)$ can be pictured as "beamlets" coming from the region A_n of the plane $z = 0$ (Fig. 1.2). The width of the squares can be chosen small enough so that, within each square, the following approximations can be

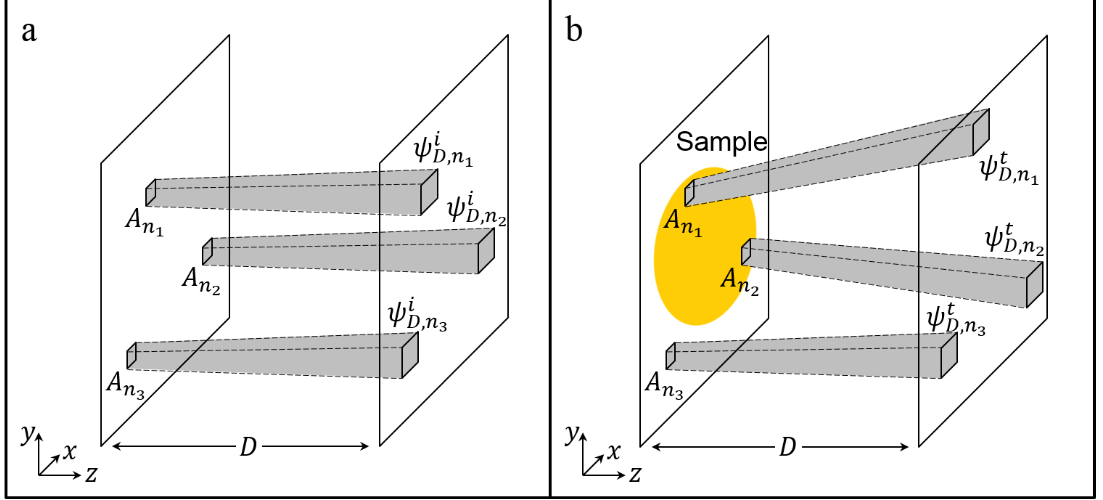

Figure 1.2: Schematic representation of three beamlets travelling in free space (a), and of the effect of refraction caused by a sample (b).

performed:

$$M(x',y') = M(x'_n, y'_n) = M_n, \tag{1.37}$$

$$\begin{aligned} \phi(x',y') &= \phi(x'_n,y'_n) + (x'-x'_n)\frac{\partial\phi}{\partial x'}(x'_n,y'_n) + (y'-y'_n)\frac{\partial\phi}{\partial y'}(x'_n,y'_n) = \\ &= \phi_n + (x'-x'_n)\partial_x\phi_n + (y'-y'_n)\partial_y\phi_n. \end{aligned} \tag{1.38}$$

Ignoring the constant phase factors in the expression for $\phi(x',y')$, it is possible to write:

$$\begin{aligned} \psi^t_{D,n}(x,y) = \frac{\exp(ikD)}{i\lambda D}\exp\left[-M_n\right] \\ \times \iint_{A_n}\psi^i_0(x',y')\exp\left[-i(x'\partial_x\phi_n + y'\partial_y\phi_n)\right] \\ \times\exp\left\{\frac{ik}{2D}[(x-x')^2+(y-y')^2]\right\}dx'dy'. \end{aligned} \tag{1.39}$$

Rearranging the terms in the exponentials of Eq. 1.39, it is possible to relate $\psi^t_{D,n}(x,y)$ and $\psi^i_{D,n}(x,y)$ with the following expression:

$$\psi^t_{D,n}(x,y) = \exp\left[-i(x\partial_x\phi_n + y\partial_y\phi_n)\right]\exp\left\{-i\frac{D}{2k}\left[(\partial_x\phi_n)^2 + (\partial_y\phi_n)^2\right]\right\} \times \exp\left[-M_n\right]\psi^i_{D,n}\left(x + D\frac{\partial_x\phi_n}{k}, y + D\frac{\partial_y\phi_n}{k}\right). \quad (1.40)$$

The field $\psi^t_{D,n}(x,y)$ resulting from the region A_n in presence of an object can be expressed as the field $\psi^i_{D,n}(x,y)$, observed without the object, shifted by the vector $(D\partial_x\phi_n/k, D\partial_y\phi_n/k)$ and with amplitude reduced by the factor $\exp[-M_n]$. The first exponential term in Eq. 1.40 ensures that a further propagation of the beam will result in an additional deflection, while the second exponential accounts for the additional path length of the deflected field with respect to the reference field, without the object. The lateral shift of the field corresponds to an angular deflection $\alpha_x = \partial_x\phi_n/k$ in the x direction and $\alpha_y = \partial_y\phi_n/k$ in the y direction. This is equivalent to the phenomenon of refraction encountered in ray optics. From Eq. 1.34 and 1.40, we can therefore interpret the total field at a distance D from an object as the superposition of a series of “beamlets” that are absorbed and refracted by the sample. The main difference between this interpretation and the ray optics one is that here the total intensity on the plane $z = D$ will, in general, be different from the sum of the intensities of all the “beamlets”, i.e. $\left|\sum_n \psi^t_{D,n}(x,y)\right|^2 \neq \sum_n \left|\psi^t_{D,n}(x,y)\right|^2$.

1.3 Coherence

The electromagnetic field emitted by a real source presents random fluctuations, due to the probabilistic nature of the processes that govern the emission of x-rays. The same experiment, repeated multiple times, will results in a different electromagnetic field $\psi(\mathbf{x}, t)$, where $\mathbf{x} = (x, y, z)$. Such an electromagnetic field can be considered a stochastic process. The set of all the possible realizations $\left\{\psi^{(i)}(\mathbf{x}, t)\right\}_i$ of the process is called ensemble, where $\psi^{(i)}(\mathbf{x}, t)$ indicates the i-th realization.

Let us define the two-point correlation function of the process as:

$$\Gamma(\mathbf{x}_1, \mathbf{x}_2, t_1, t_2) = \langle\psi(\mathbf{x}_1, t_1)\psi^*(\mathbf{x}_2, t_2)\rangle, \tag{1.41}$$

where the angle brackets indicates the average over the ensemble. Γ is usually called *mutual coherence function*, and indicates the correlation between the statistical fluctuation of the field in the points $(\mathbf{x}_1, t_1)$ and $(\mathbf{x}_2, t_2)$. It is useful, in this context, to introduce the so-called *complex degree of coherence*:

$$\gamma(\mathbf{x}_1, \mathbf{x}_2, t_1, t_2) = \frac{\Gamma(\mathbf{x}_1, \mathbf{x}_2, t_1, t_2)}{\sqrt{\Gamma(\mathbf{x}_1, \mathbf{x}_1, t_1, t_1)\Gamma(\mathbf{x}_2, \mathbf{x}_2, t_2, t_2)}}, \tag{1.42}$$

From the Schwarz inequality, it follows that:

$$|\gamma(\mathbf{x}_1, \mathbf{x}_2, t_1, t_2)| \leq 1. \tag{1.43}$$

If the fluctuations of the fields at $(\mathbf{x}_1, t_1)$ and $(\mathbf{x}_2, t_2)$ are completely uncorrelated, then $\langle\psi(\mathbf{x}_1, t_1)\psi^*(\mathbf{x}_2, t_2)\rangle = \langle\psi(\mathbf{x}_1, t_1)\rangle\langle\psi^*(\mathbf{x}_2, t_2)\rangle = 0$, and $|\gamma(\mathbf{x}_1, \mathbf{x}_2, t_1, t_2)| = 0$.

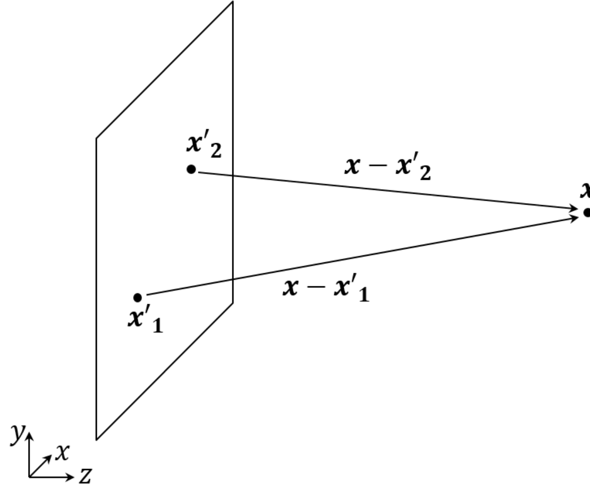

Figure 1.3: Frame of reference for two waves emitted from $\mathbf{x}'_1$ and $\mathbf{x}'_2$, and superimposing in $\mathbf{x}$.

In this case the field is said to be completely incoherent. On the other hand, for an ideal monochromatic plane wave $\psi(\mathbf{x}, t) = \exp\left[i(\mathbf{kx} - \omega t)\right]$, $|\gamma(\mathbf{x}_1, \mathbf{x}_2, t_1, t_2)| = 1$. In this case the field is said to be completely coherent.

To better understand the concept of coherence, let us consider Eq. 1.19. The field $\psi_\omega(x, y, z)$ can be seen as the superposition of spherical waves emitted from each point $(x', y', 0)$ of the plane $z = 0$ with amplitude $\psi_\omega(x', y', 0)$, and that have travelled a distance $r = \sqrt{(x - x')^2 + (y - y')^2 + z^2} \approx z + [(x - x')^2 + (y - y')^2]/(2z)$. With reference to Fig. 1.3, let us analyse the superposition of two of these waves, emitted from the points $\mathbf{x}'_1 = (x'_1, y'_1, 0)$ and $\mathbf{x}'_2 = (x'_2, y'_2, 0)$ on the plane $z = 0$, within the context of coherence, i.e. considering the electromagnetic field as a stochastic process. If a polychromatic wave is considered, it is possible to write the time-dependent field at the point $\mathbf{x} = (x, y, z)$ as [3]:

$$\Psi\left(\mathbf{x}, t\right) = K_1 \Psi\left(\mathbf{x}'_1, t_1\right) + K_2 \Psi\left(\mathbf{x}'_2, t_2\right), \tag{1.44}$$

where $t_1 = t - |\mathbf{x} - \mathbf{x}'_1|/c$, $t_2 = t - |\mathbf{x} - \mathbf{x}'_2|/c$, and K_1 and K_2 are pure imaginary numbers. The intensity $I(\mathbf{x})$ measured at the point $\mathbf{x}$ is equal to the time average of the square modulus of $\Psi(\mathbf{x}, t)$:

$$I(\mathbf{x}) = \left\langle |K_1 \Psi(\mathbf{x}'_1, t_1)|^2 \right\rangle_t + \left\langle |K_2 \Psi(\mathbf{x}'_2, t_2)|^2 \right\rangle_t + 2\,\mathrm{Re}\left[\langle K_1 K_2^* \Psi(\mathbf{x}'_1, t_1)\, \Psi^*(\mathbf{x}'_2, t_2)\rangle_t\right] \quad (1.45)$$

Let us define $I_1(\mathbf{x})$ as the intensity measured when only the wave coming from $\mathbf{x}'_1$ is present:

$$I_1(\mathbf{x}) = \left\langle |K_1 \Psi(\mathbf{x}'_1, t_1)|^2 \right\rangle_t, \quad (1.46)$$

with an analogous definition for $I_2(\mathbf{x})$. Let us assume now that the process is ergodic, so that the average over time can be replaced by the average over the ensemble. It is, then, possible to write:

$$\begin{aligned} I(\mathbf{x}) &= I_1(\mathbf{x}) + I_2(\mathbf{x}) + 2\sqrt{I_1(\mathbf{x}) I_2(\mathbf{x})}\,\mathrm{Re}\left[\gamma(\mathbf{x}'_1, \mathbf{x}'_2, t_1, t_2)\right] = \quad (1.47) \\ &= I_1(\mathbf{x}) + I_2(\mathbf{x}) + 2\sqrt{I_1(\mathbf{x}) I_2(\mathbf{x})}\,|\gamma(\mathbf{x}'_1, \mathbf{x}'_2, t_1, t_2)| \cos\left[\Phi(\mathbf{x}'_1, \mathbf{x}'_2, t_1, t_2)\right], \end{aligned}$$

where we used $\gamma(\mathbf{x}'_1, \mathbf{x}'_2, t_1, t_2) = |\gamma(\mathbf{x}'_1, \mathbf{x}'_2, t_1, t_2)| \exp\left[i\Phi(\mathbf{x}'_1, \mathbf{x}'_2, t_1, t_2)\right]$. The last term of Eq. 1.47 is usually called *interference term*, and expresses the variation between the total intensity $I(\mathbf{x})$ and the sum of the intensities $I_1(\mathbf{x})$ and $I_2(\mathbf{x})$. For a perfectly incoherent field, the interference term is equal to 0 and the total intensity in $\mathbf{x}$ can be expressed as the sum of the intensities produced by the fields in $\mathbf{x}'_1$ and $\mathbf{x}'_2$; this result can be generalized to an arbitrary number N of points $\{\mathbf{x}'_i\}$, with $i = 1, \ldots, N$. In a perfectly coherent field, instead, there are

no statistical fluctuations and the results obtained in the previous sections can be used to calculate the intensity distribution of a field in a given geometry.

2

X-ray imaging

In this chapter the main methods for x-ray imaging will be introduced and described in the theoretical framework developed in the previous chapter. First absorption-based imaging is discussed; this represents the most used x-ray imaging modality, with the simplest experimental setup. Then some of the most used phase-contrast imaging methods are introduced, each offering different advantages and capabilities. Last coherent diffraction imaging is described, where high resolution images can be obtained by solving an inverse problem. The focus here will be on methods currently employed in x-ray imaging, however it is important to note that the concept of phase contrast was first introduced in optical microscopy by Zernike [6], and that later other methods have been presented exploiting phase contrast with visible light [7]. Another important imaging modality not discussed in this chapter, which employs lenses to focus the beam on a small spot on the sample, is scanning x-ray microscopy [8, 9, 10, 11, 12].

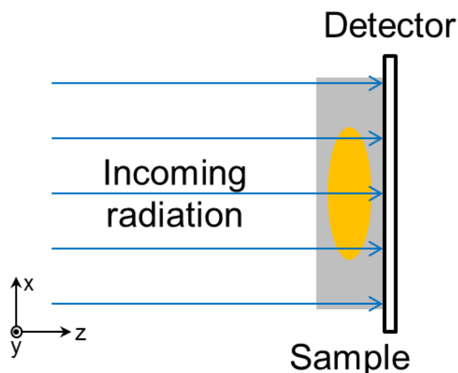

Figure 2.1: Schematic diagram of an absorption-based imaging system.

2.1 Absorption-based imaging

A typical setup for absorption-based x-ray imaging is shown in Fig. 2.1. An x-ray source is used to illuminate a sample of interest, and an x-ray detector is placed immediately after the sample to detect the transmitted intensity. Using Eq. 1.31, the ratio between the transmitted intensity I^t and the intensity incident on the sample I^i is:

$$\frac{I^t(x,y)}{I^i(x,y)} = \exp\left[-2k\int_0^l \beta(x,y,z)dz\right] = \exp\left[-2M(x,y)\right]. \tag{2.1}$$

where l is the sample thickness and $M(x,y) = k\int_0^l \beta(x,y,z)dz$. The last equation is the well-known Beer-Lambert law. Since x-ray detectors are only capable of measuring the wave intensity (proportional to the square modulus of the electromagnetic field), rather than its complex amplitude, the phase term in Eq. 1.31 is lost.

2.2 Phase-contrast imaging

Phase contrast imaging includes all the imaging modalities in which the phase term $\phi(x,y)$ of the object complex transmission function $T(x,y)$ contributes to image contrast.

2.2.1 Free-space propagation

In this imaging modality x-rays coming from a source and going through a sample, are detected at a certain distance D after the sample. A scheme of the setup is shown in Fig. 2.2; note that $D=0$ is equivalent to the absorption-based system described above. Let $\psi_0^i(x,y)$ be the field incident on the sample in the plane $z=0$, and $\psi_0^t(x,y)$ the field just after the sample in the same plane $z=0$. From Eq. 1.31, we have:

$$\psi_0^t(x,y) = \psi_0^i(x,y)\exp\left[-M(x,y) - i\phi(x,y)\right] \tag{2.2}$$

where $M(x,y) = k\int_0^l \beta(x,y,z)dz$, and $\phi(x,y) = k\int_0^l \delta(x,y,z)dz$. Propagating the electromagnetic field after the sample for a distance D in free space, we obtain:

$$\psi_D^t(x,y) = \exp(ikD)\mathcal{F}^{-1}\left\{\mathcal{F}\left[\psi_0^t(x,y)\right]\exp\left[-iD\frac{k_x^2+k_y^2}{2k}\right]\right\}, \tag{2.3}$$

If the propagation distance is small, it is possible to approximate $\exp[-iD(k_x^2 + k_y^2)/(2k)] \approx 1 - iD(k_x^2+k_y^2)/(2k)$, and Eq. 2.3 becomes:

$$\psi_D^t(x,y) = \exp(ikD)\left[1 + \frac{iD}{2k}\nabla^2\right]\psi_0^t(x,y), \tag{2.4}$$

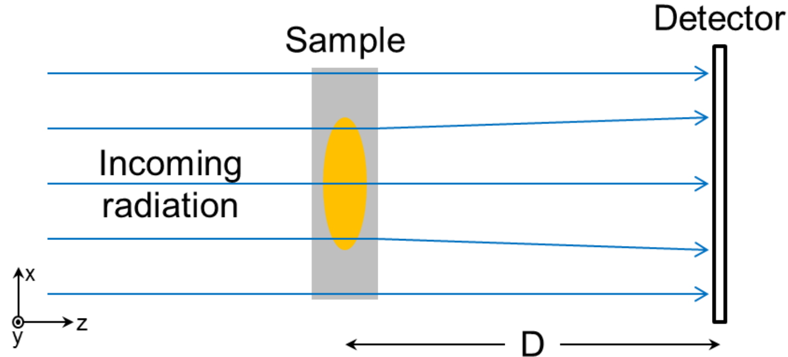

Figure 2.2: Schematic diagram of a free-space propagation imaging system.

and the intensity $I_D^t(x,y)$ measured at a distance D from the sample will be:

$$\begin{aligned} I_D^t(x,y) &= I_0^t(x,y) + \frac{D}{k}\nabla \cdot \left[I_0^t(x,y)\nabla\phi(x,y)\right] = \\ &= I_0^t(x,y) + \frac{D}{k}\left[\nabla I_0^t(x,y)\cdot\nabla\phi(x,y) + I_0^t(x,y)\nabla^2\phi(x,y)\right], \end{aligned} \tag{2.5}$$

where $I_0^t(x,y)$ is the intensity measured just after the sample. If $I_0^t(x,y)$ is slowly varying in x and y, the term proportional to its gradient can be neglected, and Eq. 2.5 can be simplified as:

$$\frac{I_D^t(x,y)}{I_0^i(x,y)} = \exp\left[-2M(x,y)\right]\left[1 + \frac{D}{k}\nabla^2\phi(x,y)\right], \tag{2.6}$$

where $I_0^i(x,y)$ is the intensity of the radiation incident on the sample. The recorded intensity differs from the absorption-based case for the presence of the phase term $\nabla^2\phi(x,y)$. This term has two important consequences: even for low absorbing materials ($\exp\left[-2M(x,y)\right] \approx 1$) the image contrast can be high due to the additional phase term; the effect of this term is particularly strong at the edges of sample structures, where the phase $\phi(x,y)$ varies rapidly. The resulting

image appears as an absorption image in which the boundaries between different materials are enhanced, due to the phase term. Free-space propagation x-ray phase contrast imaging was first demonstrated in 1995 [13] with synchrotron radiation and in 1996 with a polychromatic source [14]. Later several techniques have been developed to separate $M(x, y)$ and $\phi(x, y)$ from one or multiple images acquired at different propagation distances D; some important examples can be found in [15, 16, 17, 18]. The main advantage offered by this imaging modality is the simple experimental setup, and the increased image contrast due to the phase term. It is possible to show, however, that the increased contrast due to the phase term rapidly decreases, with respect to the absorption contrast, as a function of the source size and of the detector spatial resolution [12].

2.2.2 Grating interferometry

An interesting features of periodic objects, like gratings, is that the intensity distribution downstream of the object can replicate itself at some specific distances. Let us consider an absorption grating of period a illuminated by a plane wave, and let the width of the transmitting regions in the x direction be equal to $a/2$. Let $\psi_0^g(x, y)$ and $\psi_D^g(x, y)$ be the fields at a distance 0 and D after the grating, respectively:

$$\psi_D^g(x, y) = \exp(ikD)\mathcal{F}^{-1}\left\{\mathcal{F}\left[\psi_0^g(x, y)\right]\exp\left[-iD\frac{k_x^2 + k_y^2}{2k}\right]\right\}. \tag{2.7}$$

Because of its periodicity, the Fourier transform of $\psi_0^g(x, y)$ will be different from 0 only at some specific points in the Fourier space of coordinates $(k_x, k_y) = (2\pi p/a, 0)$, with $p \in \mathbb{Z}$. If the Fourier transform of the Fresnel propagator in these

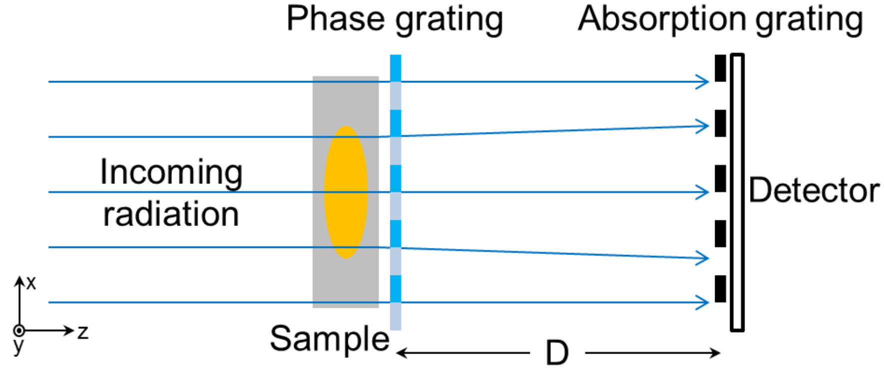

Figure 2.3: Schematic diagram of a grating-based imaging system.

points is equal to one, then the propagated field will be equal to the starting one:

$$\exp\left[-iD\frac{k_x^2+k_y^2}{2k}\right] = \exp\left[-i\frac{\pi\lambda D}{a^2}p^2\right] = 1. \tag{2.8}$$

The above condition is satisfied for propagation distances $D_n = nD_t$; where $D_t = 2a^2/\lambda$ is called the Talbot distance, and n is an integer. For these propagation distances, the intensity of the field is:

$$I^g_{D_n}(x,y) = I^g_0(x,y), \tag{2.9}$$

where $I^g_0(x,y) = |\psi^g_0(x,y)|^2$ is equal to a square wave of period a.

The same intensity distribution can be obtained using a phase grating (i.e. a grating which periodically modifies the phase of the incoming wave, rather than its amplitude). In this case the theoretical description is more complicated, and it depends on the amount of phase modulation imposed by the grating. When the phase shift oscillates by π, the characteristic intensity profile has period equal to $a/2$ and is formed at distances $D_n = nD_t/16$. When, instead, the phase shift

is $\pi/2$, the period is equal to a and the intensity pattern is formed at distances $D_n = nD_t/4$. In both the π and $\pi/2$ configurations, n in an odd integer.

The phenomenon just described can be used as the basis for the phase contrast imaging setup shown in Fig. 2.3. The first grating creates the periodic intensity pattern described before. The second grating, which has the same period as the intensity pattern, is used as an analyser. The absorption grating is scanned along x, and for each position the intensity is recorded by the detector. The curve describing the variation of the intensity with respect to the grating position is called *phase-stepping curve*. When an object is place just before or after the phase grating, the intensity profile is locally modified by absorption and refraction, as described in the previous chapter. This has a direct impact on the phase-stepping curve: the mean intensity will decrease due to absorption, and its lateral position will be shifted due to refraction. Note that the period of the intensity pattern and the shift induced by refraction are usually too small to be spatially resolved by standard detectors, which is why the absorption grating is required. By acquiring and comparing two phase-stepping curves, with and without the sample, it is possible to reconstruct the absorption $A(x, y)$ and refraction $R(x, y)$ signals, which can be related to the sample transmission function by the following equations:

$$A(x, y) = 2M(x, y), \tag{2.10}$$

$$R(x, y) = \frac{1}{k}\frac{\partial \phi}{\partial x}(x, y). \tag{2.11}$$

The firsts methods for x-ray phase contrast imaging exploiting the interference pattern created by a periodic grating were demonstrated in 2002 [19] and 2003

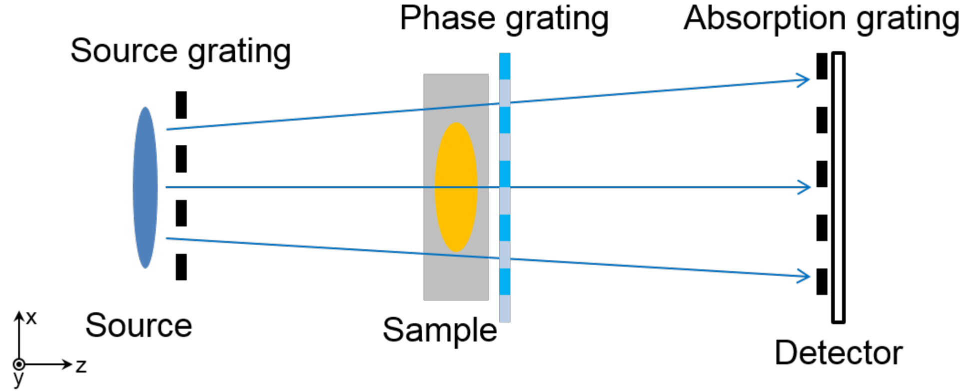

Figure 2.4: Schematic diagram of a Talbot-Lau imaging system.

[20]. The first demonstration with a laboratory source has been presented in 2006 [21]; in this case, a third absorption grating was used just after the source, in the so-called *Talbot-Lau* configuration (Fig. 2.4). If the wave illuminating the phase grating is not fully coherent, in fact, a decrease in the visibility of the intensity pattern at the detector plane is observed. The decrease in visibility, however, can be mitigated introducing the additional source grating.

2.2.3 Analyser based imaging

An ideal crystal is characterized by the periodic repetition, over a set of points (called crystal lattice) in the three dimensional space, of one or a group of atoms (called the unit cell). Due to this periodicity, it is possible to identify sets of parallel and equally spaced planes that pass through all the points of the crystal lattice. Let us consider one of these sets of planes, with inter-plane distance d, and a plane wave with wave-vector $\mathbf{k}_0$, forming an angle θ with the considered planes. It can be shown [3] that the wave is totally reflected by the crystal if the

following condition holds:

$$2d \sin\theta = m\lambda, \tag{2.12}$$

where $\lambda = 2\pi/|\mathbf{k}_0|$ is the wavelength of the plane wave, and m an integer. Equation 2.12 is the Bragg Law. Let us consider two frames of reference (x^i, y^i, z^i) and (x^t, y^t, z^t) (Fig. 2.5), so that z^i and z^t are the propagation directions of an incident and reflected wave which satisfy the Bragg law. To simplify the notation, we will omit the i and t subscripts in the coordinates, assuming that the (x^i, y^i, z^i) system is used for the incident wave, and (x^t, y^t, z^t) for the reflected wave. We will also assume that all the distances are small enough so that the effects of propagation on the wave front can be neglected. Let us consider a generic monochromatic wave of wavelength λ incident on the crystal. Its wave function on a plane perpendicular to its propagation direction can be expressed in terms of its Fourier components:

$$\psi^i(x, y) = \frac{1}{2\pi} \iint \check{\psi}^i(k_x, k_y) \exp\left[i(k_x x + k_y y)\right] dk_x dk_y, \tag{2.13}$$

with an analogous definition for the reflected wave $\psi^t(x, y)$. Of all the different Fourier components of $\psi^i(x, y)$, only the ones for which $k_x = 0$ satisfy the Bragg law; it is therefore possible to write:

$$\check{\psi}^t(k_x, k_y) = \check{\psi}^i(k_x, k_y) R(k_x) = \check{\psi}^i(k_x, k_y) \delta_D(k_x), \tag{2.14}$$

where we introduced the crystal transfer function $R(k_x)$, in this case equal to the Dirac delta $\delta_D(k_x)$. A more accurate description of the propagation of an electromagnetic wave in a crystal [3] shows that its transfer function is not exactly

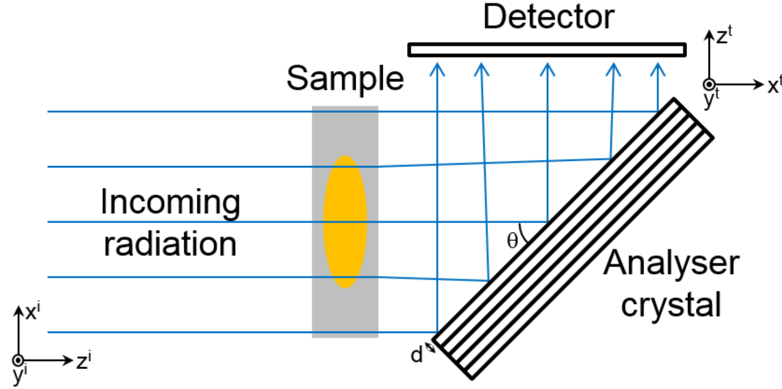

Figure 2.5: Schematic diagram of an analyser-based imaging system.

a Dirac delta, but a narrow function, of finite width, centred around $k_x = 0$. When k_x is close, but different from 0, waves will be diffracted by the crystal, but with a decreased intensity.

Let us now consider a simple object that absorbs and refract the incoming radiation with transfer function $T(x, y) = \exp[-M] \exp[-i\phi' x]$. If the object is placed just before the crystal, we will have, for the reflected wave:

$$
\begin{aligned}
\psi^t(x, y) &= \exp[-M]\, \mathcal{F}^{-1}\left[\check{\psi}^i(k_x + \phi', k_y) R(k_x)\right] = \\
&= \exp[-M] \exp[-i\phi' x]\, \mathcal{F}^{-1}\left[\check{\psi}^i(k_x, k_y) R(k_x - \phi')\right]. \qquad (2.15)
\end{aligned}
$$

Let us assume, for simplicity, that the incident wave on the sample is a plane wave propagating with a small angle with respect to the z direction, i.e. $\check{\psi}^i(k_x, k_y) = 2\pi\delta(k_x - \bar{k}_x, k_y)$. In this case we can derive a simple expression for the reflected

wave and its intensity:

$$\psi^t(x,y) = \exp\left[-M\right] \exp\left[-i\phi' x\right] R(\bar{k}_x - \phi') \tag{2.16}$$

$$I^t(x,y) = \exp\left[-2M\right] \left|R(\bar{k}_x - \phi')\right|^2 \tag{2.17}$$

As described in the previous chapter, the phase term $\exp\left[-i\phi' x\right]$ describes a refraction of the propagating beam. $|R(k_x)|^2$ has a maximum for $k_x = 0$ (the condition for which the Bragg law is satisfied), and decreases rapidly to 0 for $|k_x| > 0$. Assuming $|\phi'| < |\bar{k}_x|$, the role of ϕ' is to change the crystal reflectivity by bringing $\bar{k}_x - \phi'$ closer ($\phi' > 0$) or farther ($\phi' < 0$) from 0. In other words, a crystal can be used as a fine angular filter for the incoming radiation, so that small refraction angles induced by an object can be detected as intensity variations at the detector.

Analyser-based x-ray phase contrast imaging was first demonstrated in 1980 [22], but became popular only in the mid-nineties, especially thanks to the work presented in 1995 by Davis *et al* [23]. Later, algorithms able to separate the contribution of absorption and refraction from Eq. 2.17 have been developed [24]. When this technique is implemented with polychromatic sources, its main disadvantage is that the Bragg condition is satisfied only from one specific wavelength of the incoming radiation. The crystal acts therefore as monochromator and reflects only a small percentage of the radiation produced by the source.

2.2.4 Edge Illumination

The edge illumination setup is schematically represented in Fig. 2.6. A small, laminar beam is created using an absorbing slit placed before the sample (sample

slit). After the sample, and a propagation in free-space, the beam reaches a second slit, placed just before a single detector pixel. The two slits are usually misaligned, so that an edge of the detector slit absorbs half of the incident radiation, when the sample is not in the beam. Let us neglect the effects of propagation in the y direction; this is generally accurate in this imaging configuration as the blurring due to the finite source size and the limited detector resolution strongly limits the visibility of coherent effects caused by the free space propagation between the two slits. Let $\psi_0^i(x, y)$ be the field created by the slit, and incident on the sample, at the plane $z = 0$. If the sample transfer function varies slowly compared to the size of the slit in the x direction, it is possible to assume:

$$M(x, y) = M(x_0, y), \tag{2.18}$$

$$\phi(x, y) = \phi(x_0, y) + (x - x_0)\partial_x \phi(x_0, y), \tag{2.19}$$

and the field at the detector plane will be:

$$\psi_D^t(x, y) = \exp\left[-M(x_0, y)\right] \psi_D^i \left(x + D \frac{\partial_x \phi(x_0, y)}{k}, y \right), \tag{2.20}$$

where $\psi_D^i(x, y)$ is the field at the detector plane when the sample is removed. The sample reduces the amplitude of the beam and shifts its position along the x axis. The detector slit will allow only part of the beam to be detected; if $A(x)$ is the intensity transmission function of this slit, the intensity measured by the

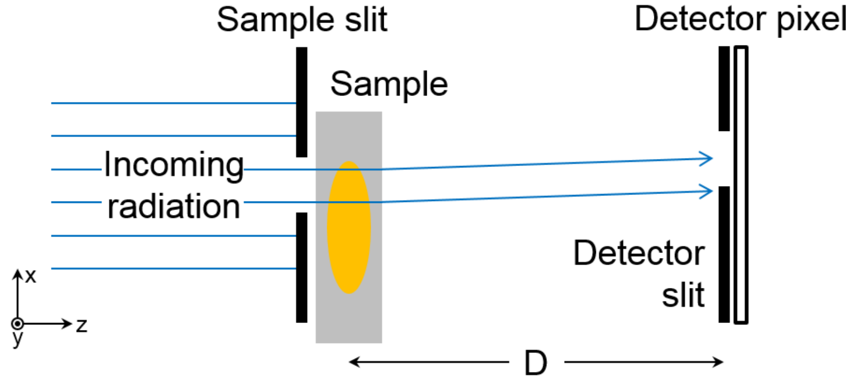

Figure 2.6: Schematic diagram of an edge illumination imaging system.

detector pixel is:

$$I_D^t(x_0,y_0) = \exp\left[-2M(x_0,y_0)\right] \int I_D^i\left(x + D\frac{\partial_x\phi(x_0,y_0)}{k}, y_0\right) A\left(x - p_0\right) dx = \\ = \exp\left[-2M(x_0,y_0)\right] I_C\left(p_0 + D\frac{\partial_x\phi(x_0,y_0)}{k}\right). \quad (2.21)$$

$I_D^i(x,y) = |\psi_D^i(x,y)|^2$; p_0 is the misalignment between the slits; (x_0,y_0) is the pixel position; $I_C(x) = \left[I_D^i \star A\right](-x)$, where $\star$ indicates the cross-correlation operator, is called the *illumination curve*, and is conceptually equivalent to the reflectivity curve $|R(k_x)|^2$ in Eq. 2.17. A refraction of the beam in the positive (negative) x direction will result in an increased (decreased) intensity detected by the pixel.

Edge illumination was first demonstrated in 2001 by Olivo *et al* [25], using synchrotron radiation, and has been later implemented with laboratory sources in 2007 [26]. Recently, algorithms capable of separating the contribution of absorption and refraction have been proposed [27, 28]. The main advantage of the edge illumination method is that it can work with standard incoherent [29], polychromatic [30] sources, and with large pixel sizes, overcoming the main limi-

tations of some of the alternative phase contrast methods described above, such as free-space propagation and analyser based imaging.

2.3 Coherent diffraction imaging

The imaging modalities described in the previous sections belong to the class of *direct imaging methods*. In all these modalities the measured intensity is directly related to the absorption properties of the sample ($M(x, y)$), or the first or second derivative of its phase ($\phi(x, y)$), or a combination of the two. Coherent diffraction imaging is, instead, an *indirect imaging method*, in the sense that the measured intensity does not directly represent features of the sample.

Let us consider the experimental setup in Fig. 2.7. Let $\psi_0^i(x, y)$ be the field incident on the sample, $\psi_0^t(x, y)$ the field after the sample at the plane $z = 0$, and $\psi_D^t(x, y)$ the field at the detector on the plane $z = D$. Using Eq. 1.19, it is possible to write:

$$\psi_D^t(x,y) = \frac{\exp(ikD)}{i\lambda D} \exp\left[\frac{ik}{2D}(x^2+y^2)\right] \iint \psi_0^t(x',y') \times \exp\left[\frac{ik}{2D}(x'^2+y'^2)\right] \exp\left[\frac{-ik}{D}(x'x+y'y)\right] dx'dy' \quad (2.22)$$

Let us suppose that the beam incident on the sample is spatially limited, for example by the presence of a pinhole (Fig. 2.7). If the propagation distance D is large enough so that $k(x'^2 + y'^2)/(2D) \ll 1$, for (x', y') within the pinhole aperture, the corresponding exponential term in Eq. 2.22 can be neglected, and

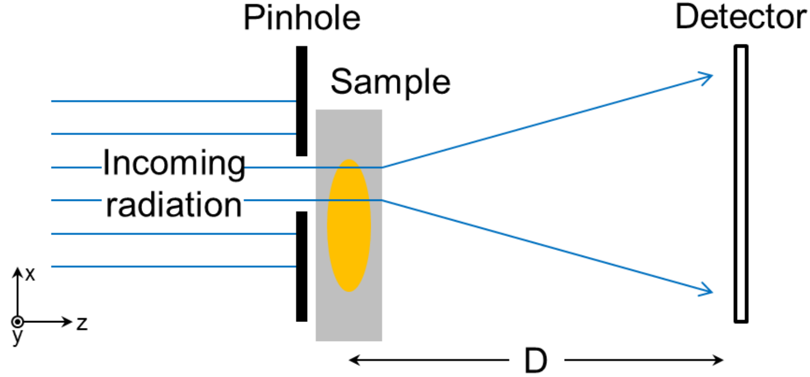

Figure 2.7: Schematic diagram of a coherent diffraction imaging system.

the detected intensity can be expressed as:

$$
\begin{aligned}
I_D^t(x, y) &= \left| \iint \psi_0^t(x', y') \exp\left[-\frac{ik}{D}(x'x + y'y) \right] dx'dy' \right|^2 = \\
&= \left| \mathfrak{F}\left[\psi_0^t\right] \left(\frac{kx}{D}, \frac{ky}{D} \right) \right|^2 .
\end{aligned} \tag{2.23}
$$

In the described configuration, it is therefore possible to directly measure the modulus of the Fourier transform of the field at the sample plane. The so called *phase problem* consists in reconstructing the function $\psi_0^t(x, y)$ from the measurement of the modulus of its Fourier transform $[I_D^t(x, y)]^{1/2}$. The phase problem is encountered not only in x-ray coherent diffraction imaging, but also in other fields such as electron microscopy, wave front sensing, astronomy and crystallography; more details can be found in [31, 32] and references therein. It is clear that the measured diffraction pattern alone is not sufficient to solve the phase problem, i.e. an infinite number of different wave functions exist that would result in the same diffracted intensity. To restrict the number of possible solutions, additional information about the function $\psi_0^t(x, y)$ needs to be available. Provided this ad-

ditional information is available, and that a unique solution exist, a method that combines the information provided by the diffraction pattern $I_D^t(x, y)$ with the *a priori* information about the function $\psi_0^t(x, y)$ is required to find the solution.

For example, the phase problem can be solved when $\psi_0^t(x, y)$ is equal to 0 outside a region S, called support, and if S is known and sufficiently small. The problem is then solved iteratively, through specific reconstruction algorithms [33, 34]. A different approach consists in acquiring multiple diffraction patterns from different, but partially overlapping, regions of the sample. This is achieved by shifting the sample with respect to the incident radiation between each acquisition. This approach is called *ptychography*, and the additional information comes from the fact that the same region of the sample contributes to more than one diffraction pattern. $\psi_0^t(x, y)$ is given by the product of the field incident on the sample $\psi_0^i(x, y)$ and the sample transmission function $T(x, y)$. In ptychography, each diffraction pattern $I_{D,n}^t(x, y)$ comes from a different wave $\psi_{0,n}^t(x, y)$, which can be expressed as $\psi_0^i(x, y)T(x - x_n, y - y_n)$. From a set of measurements $\left\{I_{D,n}^t(x, y)\right\}$, specifically designed algorithms [35, 36] can be use to retrieve both the illumination function $\psi_0^i(x, y)$ and the sample complex transfer function $T(x, y)$. The peculiar features of coherent diffraction imaging are that:

- it makes possible to retrieve $T(x, y)$, providing direct access to the quantities $M(x, y)$ and $\phi(x, y)$,
- the final resolution of the reconstructed function does not depend on the detector resolution, as it is usually the case with direct imaging methods.

The measurement, in fact, happens in the Fourier space, i.e. the modulus of the Fourier transform of $\psi_0^t(x, y)$ is measured, and the final resolution depends

on the largest angle for which the diffraction pattern is measured. Alternative ways to increase the resolution beyond the limits imposed by the detector pixel size consist in the use of lenses to create a magnified image of the sample on the detector. In this case the final resolution is usually limited by the numerical aperture of the lens. This can represent an important limitation in x-ray imaging, where lenses with high numerical aperture are difficult to fabricate. Coherent diffraction imaging removes this limitation and it is, therefore, a valuable tool for high resolution x-ray imaging, allowing resolutions of the order of few nanometers [37]. Another important possibility offered by coherent diffraction imaging is its implementation in tomography [38, 39, 40], allowing high resolution three-dimensional reconstructions of the sample refractive index.

3

Wave optics simulation

In this chapter we describe a framework for the simulation of the x-ray phase contrast imaging systems discussed in the previous chapter. The simulation of x-ray propagation in vacuum and of their interaction with matter can be performed with different methods, which can be divided in two main groups: ray tracing and wave optics. In ray tracing, the electromagnetic field is described in terms of *rays*, or *photons*. The simulation starts at the source focal spot where photons are created with a random position and propagation direction. Each photon is then propagated in empty space and matter, until, if it is not absorbed by the sample or any component of the experimental setup, it is detected. The final intensity measured by the detector is given by the sum of all the intensities of the individual photons. The main advantage of ray tracing methods is that each photon is independent from the others, and the simulation can be easily parallelized on multi-CPU or GPU systems. The main disadvantage of standard ray tracing simulations is that they are based on geometrical optics and cannot take coherence effects into account, i.e. interference between waves is neglected.

Recently, however, new methods are being developed to include coherence effects in ray tracing simulations [41]. On the other hand, wave optics simulations are developed to numerically solve the diffraction integrals described in the first chapter. This approach is more accurate than ray tracing, especially when coherent radiation is considered, and can predict experimental results with high accuracy. Care has to be taken with regards to the specific implementation parameters used in wave optics simulations, otherwise they can result in significant artefacts, as discussed below.

In the following we will focus our attention on the simulation of an edge illumination system. Our study, however, can be easily adapted to different phase contrast imaging systems. The results discussed in this chapter are based on the work presented in [42]. In the previous chapter, we described the edge illumination system for a single row of detector pixels (Fig. 2.6). In this configuration, an image can be obtained by scanning the sample through the beam. The system, however, can be parallelized for use with a two dimensional area detector, and the edge illumination condition can be repeated for each row of the detector pixels, as shown in Fig. 3.1. The first mask (sample mask) creates a series of secondary beams each of which propagates towards a single detector pixel; the second mask (detector mask) acts as a series of edges that intercept a fixed portion of each beam. When a sample is placed between the two masks, each secondary beam is deflected by an angle α (in the direction x perpendicular to the mask lines) proportional to $\partial\phi/\partial x$, where ϕ is the phase shift caused by the sample; this increases or decreases the signal of each pixel in proportion with $\partial\phi/\partial x$. At the same time, each beam is partially absorbed by the sample and its total intensity decreases.

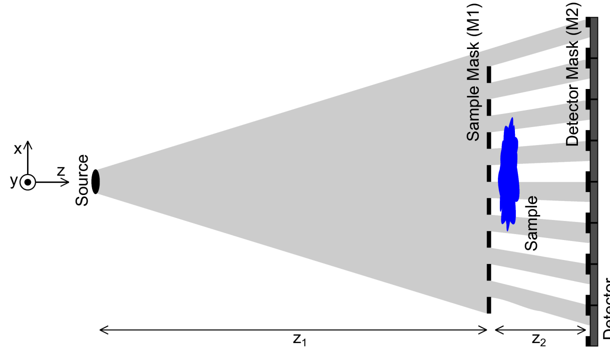

Figure 3.1: Schematic diagram of an edge illumination setup.

3.1 Theoretical framework

The system shown in Fig. 3.1 can be effectively described as a series of free space propagations and transmissions through objects (an "object" being a mask or the sample). Let us consider, in the reference frame shown in Fig. 3.1, a monochromatic wave with wavelength λ propagating in the z direction. Free space propagation can be described by means of the Fresnel diffraction integral (Eq. 1.19), so that if $\psi_A(x, y)$ and $\psi_B(x, y)$ are the complex amplitude of the electromagnetic field on two planes $z = z_A$ and $z = z_B$ respectively, with no objects in between, it is possible to write:

$$\psi_B(x, y) = \psi_A(x, y) * H_{\Delta z}(x, y), \tag{3.1}$$

where $\Delta z = z_B - z_A$, $*$ indicates the convolution operation, and H_z is the Fresnel propagator:

$$H_z(x, y) = \frac{\exp(ikz)}{i\lambda z} \exp\left(ik\frac{x^2 + y^2}{2z}\right), \tag{3.2}$$

with $k = 2\pi/\lambda$. For an edge illumination setup, Eq. (3.1) allows us to describe the free space propagation of x-rays between the source and the sample mask and

between the two masks.

The propagation through an object can be taken into account through its complex transfer function T_{obj}:

$$\psi_{out}(x,y) = T_{obj}(x,y)\psi_{in}(x,y), \tag{3.3}$$

where ψ_{in} and ψ_{out} are the complex amplitudes of the incoming and outgoing fields, respectively. For an ideal mask, $T_M(x,y) = 1$ within the apertures and $T_M(x,y) = 0$ in the absorbing septa.

Let us assume, for simplicity's sake, that the system we want to describe has no dependence upon y; in this case, by neglecting a constant factor arising from the integration over y [1], we can consider the one-dimensional case ($y = 0$). With reference to Fig. 3.1, it is possible to write the expression for the complex amplitude of the electromagnetic field at the detector mask, in the case of a point source placed in the position $x_s = 0$ ($\psi_0(x) = A_0\delta_D(x)$, where δ_D is the Dirac delta), as:

$$\psi_{M2}(x) = A_0\left[H_1(x)T_{M1}(x)T_{obj}(x)\right] * H_2(x), \tag{3.4}$$

where $H_1 \equiv H_{z_1}$, $H_2 \equiv H_{z_2}$, and the object and the sample mask are assumed to be in the same plane. In the general case of $x_s \neq 0$, $H_1(x)$ must be replaced with $H_1(x - x_s)$ to obtain the complex amplitude of the electromagnetic field on the detector mask $\psi_{M2}(x, x_s)$. Noting that:

$$H_z(x - x_s) = \frac{i\lambda z}{\exp(ikz)} H_z(x)H_z(x_s)\exp(-ikxx_s/z), \tag{3.5}$$

it is possible to express $\psi_{M2}(x, x_s)$ in terms of $\psi_{M2}(x)$ as:

$$\psi_{M2}(x, x_s) = C(x)\psi_{M2}\left(x + \frac{z_2}{z_1}x_s\right), \tag{3.6}$$

where $C(x)$ is a phase factor:

$$C(x) = \exp\left[i\frac{k}{2z_1}\left(1 - \frac{z_2}{z_1}\right)x_s^2 - i\frac{k}{z_1}xx_s\right]. \tag{3.7}$$

Eq. (3.6) can be used to take into account an incoherent source of finite size; in this case, in fact, the intensity on the detector can be expressed as the sum of the intensities coming from each point of the source:

$$I_D(x) = \int_{-\infty}^{\infty} S(x_s)|\psi_{M2}(x, x_s)T_{M2}(x)|^2 dx_s, \tag{3.8}$$

where $S(x_s)$ is the source spatial intensity distribution. Indicating by $I_p(x) = |\psi_{M2}(x)|^2$ the intensity that would be measured on the detector mask with a point source placed in $x_s = 0$, and with $S_r(x) = (z_1/z_2)S(-xz_1/z_2)$ the rescaled source intensity distribution, Eq. (3.8) becomes:

$$I_D(x) = [S_r(x) * I_p(x)]\,|T_{M2}(x)|^2 \tag{3.9}$$

and the final intensity measured by the n-th pixel will be given by:

$$I_n = \int_{x_n}^{x_n+P} I_D(x)dx, \tag{3.10}$$

where x_n is the pixel position and P is the pixel dimension.

It is therefore possible to describe the entire edge illumination setup by means of a series of convolutions and products. Finally, it is important to remember that the convolution theorem allows calculating convolutions as products by means of the Fourier Transform (FT):

$$f(x) * g(x) = \mathcal{F}^{-1}\left\{\mathcal{F}\left[f(x)\right]\mathcal{F}\left[g(x)\right]\right\}, \tag{3.11}$$

where $\mathcal{F}$ is the FT operator. The convolution theorem plays a basic role in the development of a computationally efficient simulation.

3.2 Implementation

To simulate an edge illumination experiment it is necessary to solve Eq. (3.4), Eq. (3.9) and Eq. (3.10); this can be done by sampling each of the considered functions and performing convolutions and products numerically, rather than analytically. Convolutions can be performed by means of the Fast Fourier Transform (FFT) algorithm, which is computationally very efficient. Nonetheless, it is important to pay attention to some problems that are typically encountered when using this approach. In the following sections of this chapter, we will adopt the following definition of Fourier transform:

$$\hat{f}(\xi) = \int f(x)\exp\left(-2\pi i\xi x\right)dx, \tag{3.12}$$

where $\hat{f}(\xi)$ is the Fourier transform of $f(x)$. This definition, in fact, is the analogous of the discrete FFT, used in numerical calculations.

3.2.1 Sampling considerations

Let us consider a bandlimited function $f(x)$ and let W_f be the width of its frequency spectrum. Sampling $f(x)$ at a rate $1/\Delta x$ implies that its FFT is confined to the frequency range $[-1/(2\Delta x), 1/(2\Delta x)]$ of width $1/\Delta x$: if $1/\Delta x < W_f$, aliasing will occur [43]. One way to avoid aliasing problems is to increase the sampling rate until $1/\Delta x > W_f$. The first step is thus to identify the frequency bandwidth of each function considered in the algorithm, in order to set a sufficiently high sampling rate.

Let us consider the Fresnel propagator and its Fourier transform:

$$H_z(x) \propto \exp\left(i2\pi\frac{x^2}{2z\lambda}\right); \qquad \hat{H}_z(\xi) \propto \exp\left(-i\pi z\lambda\xi^2\right); \tag{3.13}$$

$\hat{H}_z(\xi)$ is not bandlimited, which means that it should not be possible to use the FFT without altering the original frequency spectrum. Since $H_z(x)$ is an imaginary exponential of argument x^2, the frequency at which it varies increases with the position x; however, the simulated object and masks typically have finite dimensions, so that only a limited portion of space needs to be considered in the simulation. We can therefore assume that the frequency spectrum we are considering is effectively limited.

Mathematically, it is possible to describe the limited portion of space by introducing the $\mathrm{rect}(x)$ function, which is equal to 1 for $|x| \leq 0.5$ and 0 for $|x| > 0.5$. If the width of the simulated space is L, the function we are dealing with is:

$$H_{z,eff}(x) \propto \exp\left(i2\pi\frac{x^2}{2z\lambda}\right)\mathrm{rect}\left(\frac{x}{L}\right) \tag{3.14}$$

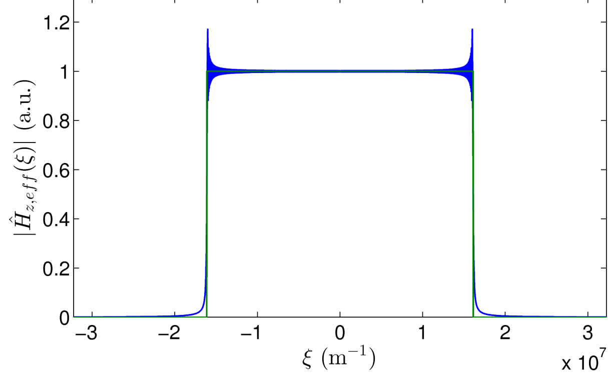

Figure 3.2: Modulus of $\hat{H}_{z,eff}(\xi)$: the blue curve is calculated numerically, while the green curve is calculated analytically with the approximation discussed in the text. Parameters used in the simulation: $z = 2$ m, $L = 2$ mm, $\lambda = 0.31$ Å($E = 40$ KeV).

and thus:

$$\hat{H}_{z,eff}(\xi) \propto \exp\left(-i\pi z\lambda\xi^2\right) * \frac{\sin(\pi L\xi)}{\pi\xi} = \\ = \int_{-\infty}^{\infty} \exp\left[-i\pi z\lambda(\xi-\eta)^2\right] \frac{\sin(\pi L\eta)}{\pi\eta}\,\mathrm{d}\eta. \tag{3.15}$$

We are interested in calculating $\hat{H}_{z,eff}(\xi)$ for high frequency values (i.e. $\gg 1/L$); at the same time, due to the $\sin(\pi L\eta)/(\pi\eta)$ term, the main contribution inside the integral is due to values of η of the order of $1/L$. We can then make the approximation $(\xi-\eta)^2 \approx \xi^2 - 2\xi\eta$ for small values of η, and the modulus of Eq. (3.15) becomes:

$$\left|\hat{H}_{z,eff}(\xi)\right| \propto \left|\int_{-\infty}^{\infty} \exp\left(i2\pi z\lambda\xi\eta\right) \frac{\sin(\pi L\eta)}{\pi\eta}\,\mathrm{d}\eta\right| = \mathrm{rect}\left(\frac{z\lambda\xi}{L}\right). \tag{3.16}$$

The convolution product in the Fourier space acts here as a “low-pass” filter with a cut-off frequency $\xi_{cut} = L/(2z\lambda)$.

Fig. 3.2 shows a comparison between the functions $|\hat{H}_{z,eff}(\xi)|$ (calculated

numerically) and $\mathrm{rect}(z\lambda\xi/L)$; the approximation made to perform the analytical calculation does not allow describing the oscillations of $|\hat{H}_{z,eff}(\xi)|$ around its mean value, but it does allow the correct derivation of its average behaviour. Furthermore, it provides an important parameter, $\xi_{cut} = L/(2z\lambda)$, which is the frequency at which $|\hat{H}_{z,eff}(\xi)|$ reaches half its average value near $\xi = 0$. For frequency values greater than $2\xi_{cut}$, $|\hat{H}_{z,eff}(\xi)|$ can be effectively considered equal to 0; for this reason, we consider the frequency bandwidth of the effective Fresnel propagator to be:

$$W_H = 2L/(z\lambda). \tag{3.17}$$

Let us consider now the complex transfer function of a sample mask with a single aperture of width A and its Fourier transform:

$$T_M(x) = \mathrm{rect}\left(\frac{x}{A}\right); \qquad \hat{T}_M(\xi) = \frac{\sin(\pi A\xi)}{\pi\xi}; \tag{3.18}$$

$\hat{T}_M(\xi)$ is also a non-bandlimited function. However, $|\hat{T}_M(\xi)| < 10^{-3}|\hat{T}_M(0)|$ for $\xi > 10^3/(\pi A)$; hence, the error made by neglecting frequencies greater than $10^3/(\pi A)$ can be considered negligible. This leads us to set:

$$W_M = \frac{2 \times 10^3}{\pi A}. \tag{3.19}$$

The above condition still holds for the general case of a mask with several apertures of width A. Note that the selected threshold ($10^{-3}|\hat{T}_M(0)|$) is arbitrary, and other values can in principle be used. A higher threshold would result in a less restrictive condition for Δx, but also in possible numerical artefacts.

Let us now consider a general object obtained as the convolution of a rect

function with a Gaussian function and its Fourier transform:

$$T_{obj}(x) \propto \exp\left(-\frac{x^2}{2\sigma_o^2}\right) * \mathrm{rect}\left(\frac{x}{O}\right);$$
$$\hat{T}_{obj}(\xi) \propto \exp\left(-2\pi^2\sigma_o^2\xi^2\right)\frac{\sin(\pi O\xi)}{\pi\xi}; \tag{3.20}$$

the rect function allows us to take into account the object dimension O, while the Gaussian function does the same for its smoothness through σ_o. Following the previous argument, $|\hat{T}_{obj}(\xi)| < 10^{-3}|\hat{T}_{obj}(0)|$ if $\xi > 10^3/(\pi O)$ and/or $\xi > [3\ln 10/(2\pi\sigma_o^2)]^{1/2}$. We can then set:

$$W_{obj} = \min\left\{\frac{2\times 10^3}{\pi O}, \left[\frac{6\ln 10}{\pi\sigma_o^2}\right]^{1/2}\right\}. \tag{3.21}$$

Comparing Eq. (3.19) and Eq. (3.21), we can see that W_M is greater than W_{obj} if $A < O$ and/or if $A \lesssim 300\,\sigma_o$. In a typical edge illumination setup, $A \approx 1 \div 50$ μm and we can therefore conclude that, for objects with micrometric and/or larger internal structures, $W_{obj} < W_M$; in the following this condition will be assumed to be true.

Let us finally consider a Gaussian distributed source with standard deviation σ_s. The rescaled source intensity distribution is then:

$$S_r(x) \propto \exp\left(-\frac{x^2}{2\sigma_r^2}\right); \qquad \hat{S}_r(\xi) \propto \exp\left(-2\pi^2\sigma_r^2\xi^2\right); \tag{3.22}$$

where $\sigma_r = (z_2/z_1)\sigma_s$. Following the previous argument, it is then possible to set:

$$W_{Sr} = \left[\frac{6\ln 10}{\pi\sigma_r^2}\right]^{1/2}. \tag{3.23}$$

Studying every function separately does not ensure that aliasing problems are avoided; when we multiply two functions, in fact, the frequency bandwidth changes. Let us consider two bandlimited function $f(x)$ and $g(x)$ and the product $h(x) = f(x)g(x)$; in the Fourier space, $\hat{h}(\xi) = \hat{f}(\xi) * \hat{g}(\xi)$, and $W_h = W_f + W_g$. In this case it is then necessary that $(W_f + W_g) < 1/\Delta x$. Taking into account all the multiplications in the algorithm, one obtains the following conditions:

$$\begin{aligned} \max\left(W_{H1} + 2W_{M1}, W_{H2}, W_{Sr}\right) &< 1/\Delta x, \\ W_{Ip} = 2\min\left(W_{H1} + 2W_{M1}, W_{H2}\right) &< 1/\Delta x, \\ \min\left(W_{Sr}, W_{Ip}\right) + 2W_{M2} &< 1/\Delta x. \end{aligned} \tag{3.24}$$

In the first inequality, the term $W_{H1} + 2W_{M1}$ is derived from the multiplication of H_1, T_{M1} and T_{obj} in Eq. (3.4), having applied the condition $W_{obj} < W_{M1}$; W_{H2} and W_{Sr} take into account H_2 and S_r in Eq. (3.4) and Eq. (3.9), respectively. In the second equation, W_{Ip} is the bandwidth of I_p: the factor of 2 derives from the square modulus of E_{M2}, while the minimum between $W_{H1} + 2W_{M1}$ and W_{H2} is taken because of the convolution product in Eq. (3.4). The last equation derives from Eq. (3.9).

Fig. 3.3 shows a comparison among various simulations of the same experimental conditions, the only difference being the sampling rate. As the sampling rate decreases, aliasing increasingly alters the original signal, and only when the conditions expressed in Eq. (3.24) are satisfied, correct results are obtained.

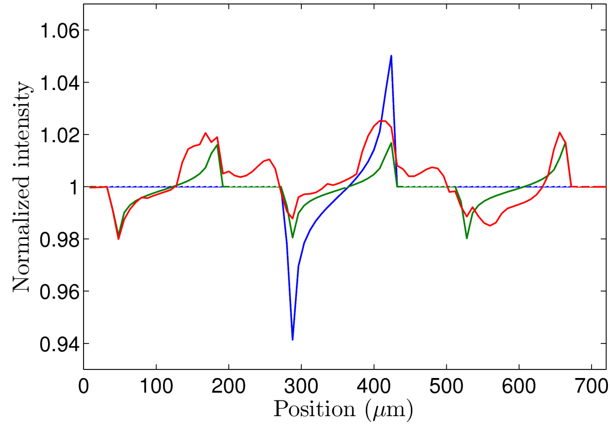

Figure 3.3: Simulations of profiles of a polypropylene wire with an edge illumination system, obtained with different numbers of sampling points: $\delta x_{blue} = 3.4$ nm is derived in accordance with Eq. (3.24), $\delta x_{green} = 15\,\delta x_{blue}$, $\delta x_{red} = 30\,\delta x_{blue}$. Only the first simulation (blue) provides correct results. Parameters used in the simulation: monochromatic Gaussian distributed source ($FWHM$ = 60 μm, E = 30 KeV); z_1 = 1.6 m, z_2 = 0.4 m; sample mask with 12 μm apertures and a period of 80 μm; detector mask with 20 μm apertures and a period of 100 μm; 50% illuminated fraction; pixel size = 100 μm; wire diameter = 140 μm; number of dithering steps (number of sub-pixel sample displacements) = 10 (each step = 8 μm).

3.2.2 Circular convolution considerations

Let us consider Eq. (3.11) and let $f_l = f(l\Delta x)$ and $g_l = g(l\Delta x)$ be sampled version of the functions f and g, with $-N/2 \leq l \leq N/2 - 1$; where the number of sampling points N is assumed to be even. The discretized version of the convolution theorem can be expressed as:

$$f_l \bar{*} g_l = FFT^{-1}\left\{FFT\left[f_l\right] FFT\left[g_l\right]\right\}; \tag{3.25}$$

where $\bar{*}$ indicates a type of discrete convolution operation, called circular convolution. Circular convolution implicitly assumes periodicity at the boundaries of the sampled space: rather than a sampled version of $f * g$, $f_l \bar{*} g_l$ is a sampled version

of $f_p * g_p$, where f_p is a periodic function consisting of the repetition of a series of infinite copies of $f(x)\text{rect}(x/L)$ shifted by the length $L = N\Delta x$ of the sampled space, i.e. $f_p(x) = \sum_n f(x - nL)\text{rect}(x/L - n)$, while $g_p(x) = g(x)\text{rect}(x/L)$. The presence of the $\text{rect}(x/L)$ term in the previous equations derives from having sampled a limited portion of space of width L.

Thus, the result of the discrete convolution between f and g, performed through the discrete Fourier transform, is $f_p * g_p$ rather that $f * g$. To obtain correct results from the simulation, it is thus necessary to understand in which circumstances $f_p * g_p = f * g$.

Let the supports of f and g be finite, and let R_f and R_g be the widths of their supports; if the support of one of the functions, for example f, is not finite or is greater than L, the sampling procedure allows us to consider $R_f = L$. When $R_f + R_g < L$, $f_p * g_p = f * g$ in every point of the sampled space. If the last condition is not met, $f_p * g_p \neq f * g$ in two regions at the boundaries of the sampled space, where the different copies in f_p interfere with each other due to the convolution with g_p; the total width of these regions is equal to $R_f + R_g - L$.

In the case of our simulations, two convolution products are performed in Eq. 3.4 and in Eq. 3.9. In Eq. 3.4 the support of $H_1 T_{M1} T_{obj}$ is equal to the dimension of the sample mask R_{M1}, while H_2 extends over the entire sampled space L; in this condition, the width of the region of error is equal to R_{M1}. In Eq. 3.9, the support R_{Sr} of the rescaled source intensity distribution S_r is limited due to the finite source size, while I_p extends over the entire sampled space L; the width of the region of error here is then equal to R_{Sr}. Let L_D be the width of the detector we want to simulate. In order for the simulation to give a correct result, it is then necessary to extend the sampled space width L until the entire detector length

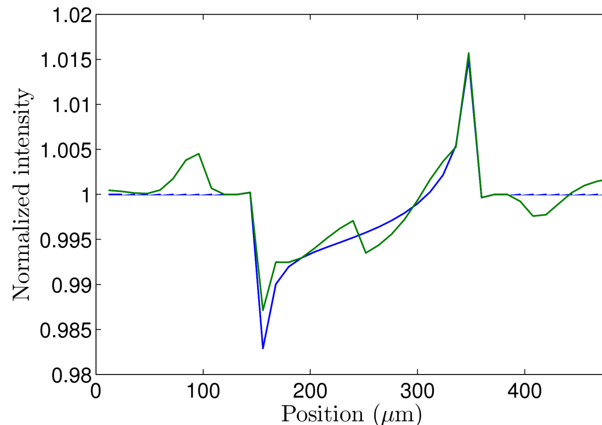

Figure 3.4: Simulations of profiles of a polypropylene wire with an edge illumination system, obtained using different dimensions for the sampled space. The blue curve is calculated considering a sampled space $L = L_D + R_{M1} + R_{Sr}$, which leads to correct results; the green curve is calculated with a sampled space $L = L_D$, which causes errors in the simulated profile. Parameters used in the simulation: monochromatic Gaussian distributed source ($FWHM$ = 1 μm, E = 30 KeV); z_1 = 100 m, z_2 = 0.1 m; sample mask with 20 μm apertures and a period of 120 μm; detector mask with 20 μm apertures and a period of 120 μm; 50% illuminated fraction; pixel size = 120 μm; wire diameter = 160 μm; number of dithering steps = 10 (each step = 12 μm).

L_D is contained in the zone within which circular and conventional convolution provide the same result, so that Eq. (3.10) can be evaluated correctly. It is easy to demonstrate that, if $L > L_D + R_{M1} + R_{Sr}$, the simulation gives correct results.

Fig. 3.4 shows a comparison between results obtained by simulating the same experimental conditions, with the only difference being the sampled space. Artefacts induced by circular convolution are evident in the profile calculated using an insufficient sampled space (green curve), while they do not affect the profile calculated with a sufficiently large sampled space (blue curve). By appropriately handling sampling and circular convolution problems along the lines described above, we can ensure that numerical implementation errors do not affect the results of our simulations.

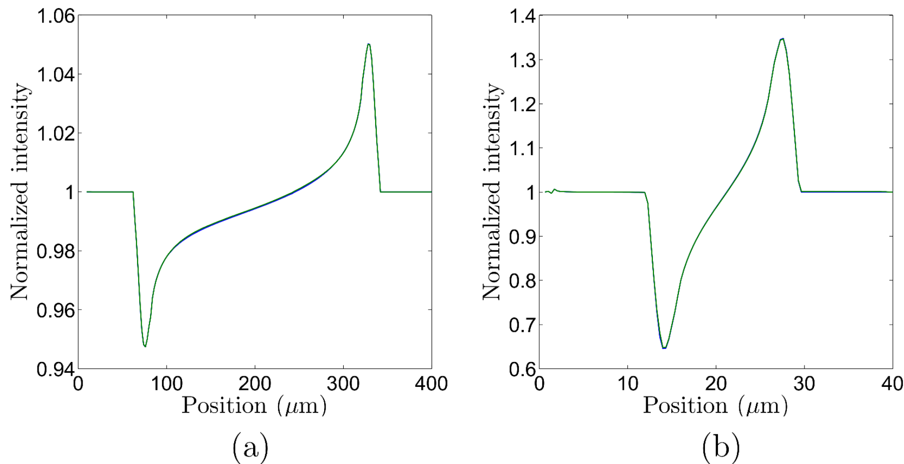

Figure 3.5: Comparison between simulated results obtained with the proposed algorithm (blue curves) and the one described in [1] (green curves). (a) Polypropylene wire: monochromatic Gaussian distributed source ($FWHM = 60$ μm, $E =$ 30 KeV); $z_1 = 1.6$ m, $z_2 = 0.4$ m; sample mask with 20 μm apertures and 80 μm period; detector mask with 50 μm apertures and 100 μm period; 50% illuminated fraction; pixel size = 100 μm; wire diameter = 260 μm; number of dithering steps = 40 (each step = 2 μm). (b) Aluminium wire: monochromatic Gaussian distributed source ($FWHM = 1$ μm, $E = 20$ KeV); $z_1 = 0.1$ m, $z_2 = 1$ m; sample mask with 3.4 μm apertures and 13.6 μm period; detector mask with 75 μm apertures and 150 μm period; 50% illuminated fraction; pixel size = 150 μm; wire diameter = 14 μm; dithering steps = 40 (each step = 0.34 μm).

3.3 Comparison with another algorithm

In this section, we compare our algorithm with the one described in reference [1], which is also based on wave optics. The most important difference between the two algorithms is the way in which the forward propagation in free space is computed. The propagation in free space is described by Eq. 3.4, and in the presented implementation is solved in Fourier space using the convolution theorem. In the algorithm presented in [1], instead, the convolution product is solved in the real space (see Eq. 1.19) using numerical integration.

Although different samples and acquisition conditions are considered in Fig.

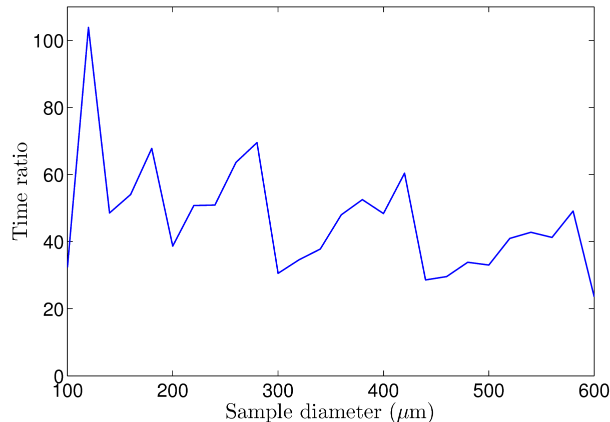

Figure 3.6: Ratio between the computational times for the algorithm described in [1] and the one presented here, as a function of the sample dimension. Parameters used in the simulation: monochromatic Gaussian distributed source ($FWHM$ = 60 μm, E = 30 KeV); z_1 = 1.6 m, z_2 = 0.4 m; sample mask with 40 μm apertures and 80 μm period; detector mask with 50 μm apertures and 100 μm period; 50% illuminated fraction; pixel size = 100 μm; polypropylene wire sample; dithering steps = 5 (each step = 16 μm).

3.5, no appreciable differences can be seen between the results provided by the two algorithms. Such comparison has been repeated for a large number of cases simulating a wide range of different experimental conditions, and the same agreement was obtained. This is an expected result, as the algorithm described in reference [1] was validated experimentally several times; rather than different results, we are aiming here for achieving the same results with a substantial gain in computation time, as well as higher flexibility and adaptability to different experimental conditions.

Fig. 3.6 shows the ratio between the computation times required by the two algorithms as a function of the dimensions of the simulated sample: for the investigated cases, the time reduction obtained through the new algorithm was between 20 and 110 fold. The algorithm in [1], in fact, uses Gaussian quadrature numerical integration to solve diffraction integrals, which is computationally

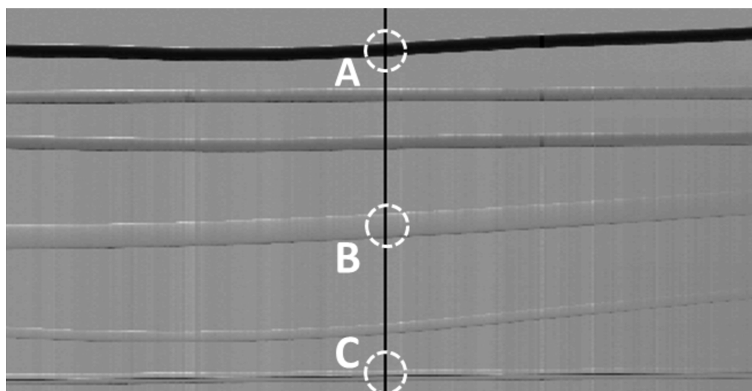

Figure 3.7: Image of different wires acquired with synchrotron radiation using the edge illumination method.

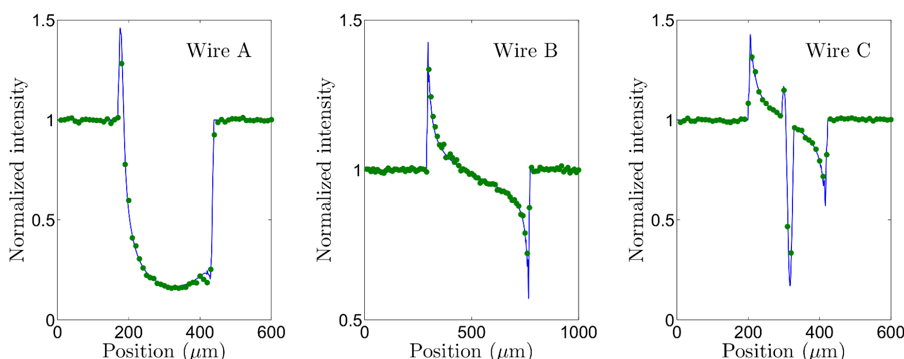

Figure 3.8: Comparison between experimental data (intensity profiles along the black vertical line in Fig. 3.7) and simulation results.

inefficient compared to computing convolution products using FFT.

The gain in terms of computational time is higher than one order of magnitude, which is crucial when the sample dimension increases or when it is necessary to simulate a large number of images like, for example, in computed tomography.

3.4 Comparison with experimental data

Finally, we compare the results of our simulation with experimental measurements performed at the SYRMEP beamline of the Elettra synchrotron facility (Trieste,

Table 3.1: Properties of wires highlighted in Fig. 3.7. PEEK stands for polyetheretherketone. The boron wire contains a thin tungsten core with an estimated diameter of 14 μm.

Wire	Material	Nominal diameter (μm)	Estimated diameter (μm)	δ [44]	β [44]
A	Titanium	250 ± 10 %	250	2.19×10^{-6}	3.46×10^{-8}
B	PEEK	450 ± 20 %	464	7.15×10^{-7}	2.74×10^{-10}
C	Boron	200 ± 20 %	204	1.12×10^{-6}	2.84×10^{-10}

Italy). A detailed description of the used experimental setup and acquisition conditions can be found in reference [27].

Fig. 3.7 shows an image acquired for a series of different wires. These were chosen as their symmetry properties enable a straightforward comparison with the one-dimensional simulation approach described here.

The vertical FWHM of the virtual x-ray source was 80 μm, and a Si (1,1,1) crystal reflection was used to select a quasi-monochromatic beam with an energy of 20 KeV (bandwidth $\approx$ 0.2%). The image was acquired through a scanning procedure [27], and two single slits were used as sample and detector masks with apertures in the vertical direction equal to 20 μm and 150 μm, respectively. The source to sample distance was 20 m, the sample to detector distance was 0.55 m, and the detector featured a single row of pixels with dimensions equal to 300×50 μm^2 in the vertical and horizontal directions, respectively. The specifications for the wires highlighted with white circles in Fig. 3.7 are listed in Table 3.1.

To test the developed method under a wide range of conditions, we selected wires with very different characteristics: titanium presents very strong absorption, PEEK is almost transparent, and the boron wire presents an additional

complication in the fact that it contains a tungsten core. The comparison between the intensity measured along the black vertical line in Fig. 3.7 and the intensity simulated with our code is shown in Fig. 3.8; a very good agreement is found for all considered wires.

3.5 Chapter conclusions

The developed simulation algorithm, based on Fresnel wave optics, has been proven to be capable of correctly simulating an edge illumination setup. The method is very general and can be easily adapted to a wide range of other x-ray imaging techniques. Numerical implementation problems such as sampling rate and sampled space have been studied in detail, and simple rules to avoid simulation errors and artefacts have been provided.

Comparisons with both a previously validated, different algorithm [1] and experimental data [27] have been carried out, resulting in very good agreement in both cases. The presented algorithm is therefore able to accurately predict experimental results, and presents the advantage of a gain greater than one order of magnitude in terms of computation time compared to previous implementations.

The discussed simulation framework has been the main tool for the preliminary investigation of the alternative implementations of x-ray phase contrast imaging developed in this project and that will be presented in the following chapters.

4

From edge illumination to beam tracking

In this chapter more details about the edge illumination method will be discussed and, from the same principles, a new imaging approach will be presented, called *beam tracking*. In edge illumination, three different physical processes contribute to the image contrast, namely absorption, refraction and ultra-small-angle scattering. These quantities can be retrieved through specific algorithms, which will be described in the next section. It will be then demonstrated how, by using a high resolution detector, the same information can be retrieved without the need of an absorbing mask placed before the detector. This can result in a reduction of exposure time and delivered dose, together with a simplified experimental setup. The results presented in this chapter are based on the work presented in [45]. In this chapter, the concept of *ultra-small-angle x-ray scattering* is introduced and used to describe the sample together with the concepts of absorption and refraction introduced in chapter 1. It is important to clarify that even if

x-ray scattering and refraction contribute differently to the signal detected, as it will be shown in the following sections, they are ultimately generated from the same physical mechanism: the diffraction of electromagnetic waves perturbed by a phase variation due to the sample.

4.1 Quantitative edge illumination

In the second chapter we described how the signal recorded in the edge illumination configuration can be expressed, for the n-th pixel, as:

$$I_n = \exp\left[-2M_n\right] I_C \left(p_0 + D\frac{\partial_x \phi_n}{k}\right) = T_n I_C \left(p_0 - \Delta x_n\right). \tag{4.1}$$

It is important to note that the measured intensity depends not only on the absorption (T_n) and refraction (Δx_n) caused by the sample, but also on the relative position p_0 between the two slits. To be able to extract quantitative information about the sample, it is important to retrieve T_n and Δx_n; this procedure is usually called *phase retrieval*. Let us consider the case in which two intensities are recorded for two different positions p_1 and p_2 of the detector slit with respect to the sample slit:

$$I_n^{(1)} = T_n I_C \left(p_1 - \Delta x_n\right); \tag{4.2}$$

$$I_n^{(2)} = T_n I_C \left(p_2 - \Delta x_n\right). \tag{4.3}$$

The two measured intensities can be combined to obtain:

$$\frac{I_n^{(1)} - I_n^{(2)}}{I_n^{(1)} + I_n^{(2)}} = \frac{I_C\left(p_1 - \Delta x_n\right) - I_C\left(p_2 - \Delta x_n\right)}{I_C\left(p_1 - \Delta x_n\right) + I_C\left(p_2 - \Delta x_n\right)} = F_{p_1,p_2}\left(\Delta x_n\right). \tag{4.4}$$

If the illumination curve I_C is known and the function F_{p_1,p_2} is injective, the last equation can be solved inverting the function F_{p_1,p_2} [27]:

$$\Delta x_n = F^{-1}_{p_1,p_2}\left(\frac{I_n^{(1)} - I_n^{(2)}}{I_n^{(1)} + I_n^{(2)}}\right); \tag{4.5}$$

substituting this value in Eq. 4.2, T_n can be calculated as:

$$T_n = \frac{I_n^{(1)}}{I_C\left(p_1 - \Delta x_n\right)}. \tag{4.6}$$

Other approaches can be used to retrieve T_n and Δx_n [28, 46], but in all cases two images with two different relative positions between the absorbing slits are required.

Equation 4.1 describes the effect of the sample in terms of absorption (T_n) and refraction (Δx_n). This description is correct if the sample transmission function varies slowly within the aperture. A third effect can appear when the sample is inhomogeneous on a scale smaller than the aperture; this is called ultra-small-angle x-ray scattering or *dark-field* signal. Each inhomogeneity within the aperture can be seen as a source of further refraction of the beam:

$$I_n = T_n I_C\left(p_0 - \Delta x_n - r\right), \tag{4.7}$$

where r describes the additional refraction from the inhomogeneity. The con-

tribution of all the inhomogeneities can be considered by summing over all the possible r values, each with a specific weight $S_n(r)$:

$$I_n = T_n \int I_C \left(p_0 - \Delta x_n - r\right) S_n(r) dr = T_n \left[I_C * S_n\right] \left(p_0 - \Delta x_n\right); \tag{4.8}$$

$S_n(r)$ is also called scattering distribution. Let us assume that the illumination function I_C can be approximated by a Gaussian function:

$$I_C(p_0) = A_0 \exp\left[-\frac{p_0^2}{2\sigma_0^2}\right]; \tag{4.9}$$

that the scattering distribution S_n is a normalized Gaussian function with standard deviation σ_n, and that three acquisitions are performed with $p_0 = [-x_1, 0, x_1]$:

$$I_n^{(1)} = TA_0\sqrt{\frac{\sigma_0^2}{\sigma_0^2+\sigma_n^2}} \exp\left[-\frac{(-x_1-\Delta x_n)^2}{2(\sigma_0^2+\sigma_n^2)}\right]; \tag{4.10}$$

$$I_n^{(2)} = TA_0\sqrt{\frac{\sigma_0^2}{\sigma_0^2+\sigma_n^2}} \exp\left[-\frac{(-\Delta x_n)^2}{2(\sigma_0^2+\sigma_n^2)}\right]; \tag{4.11}$$

$$I_n^{(3)} = TA_0\sqrt{\frac{\sigma_0^2}{\sigma_0^2+\sigma_n^2}} \exp\left[-\frac{(x_1-\Delta x_n)^2}{2(\sigma_0^2+\sigma_n^2)}\right]. \tag{4.12}$$

T_n, Δx_n and σ_n^2 can be found from the following analytical equations [47]:

$$T_n = \sqrt{\frac{2x_1^2}{\sigma_0^2(C+D)}}\frac{I_2}{A_0} \exp\left[\frac{(C-D)^2}{16(C+D)}\right]; \tag{4.13}$$

$$\Delta x_n = \frac{x_1}{2}\frac{C-D}{C+D}; \tag{4.14}$$

$$\sigma_n^2 = \frac{2x_1^2}{C+D} - \sigma_0^2; \tag{4.15}$$

where $C = -2\log\left[I_n^{(1)}/I_n^{(2)}\right]$ and $D = -2\log\left[I_n^{(3)}/I_n^{(2)}\right]$. In this case three images

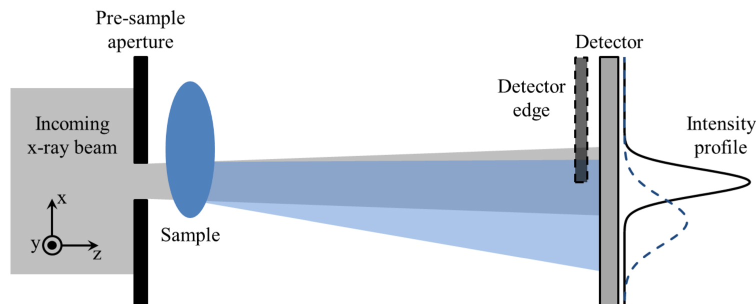

Figure 4.1: Schematic diagram of an edge illumination setup.

are required, instead of two, with three different misalignment between the sample and detector slits to extract the three parameters T_n, Δx_n and σ_n^2.

4.2 Virtual edge illumination

Figure 4.1 shows the scheme of an edge illumination setup. Here we assume that the detector slit aperture is much larger than the beam incident on the detector, so that only the effect of the edge that intercepts the beam is relevant. The importance of the detector edge comes from the fact that refraction induced by samples is usually too small to be resolved with standard detectors. When a high resolution detector is available, however, this is no longer true, and the intensity profile can be directly measured. In this configuration the detector edge can be physically removed, and its effect can be simulated through a multiplication of the intensity profile by an Heaviside function. The resulting profile can then be integrated along the x direction, providing the same result as a standard edge illumination system. The main advantage of this approach is that it is possible, from a single sample exposure, to simulate all the possible relative positions between this "virtual" edge and the beam by shifting and/or inverting the Heaviside

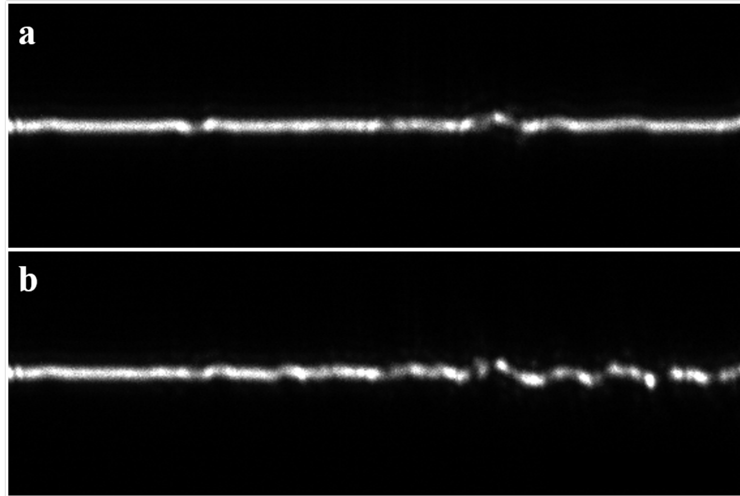

Figure 4.2: Intensity pattern produced by the pre-sample slit and acquired with the high resolution detector without (a) and with (b) a sample present in the beam. The refraction induced by the sample is evident in the right part of the image in (b).

function. Figure 4.2 shows an example of the intensity pattern acquired in the experimental configuration described below, and how this changes when a sample is introduced in the beam. Figures 4.3 (a) and (b) show a comparison between the refraction signals of a polyetheretherketone (PEEK) monofilament of 160 μm diameter immersed in water, retrieved from data acquired in the "classical" (i.e., with an absorbing edge physically present) and virtual edge illumination configurations. Experimental data were acquired at the beam line I13 (Coherence branch) of the Diamond Synchrotron Radiation (SR) facility (Didcot, UK) [48]. An x-ray energy of 9.7 keV was selected through a Si(111) crystal monochromator and a 10 μm slit was used as pre-sample aperture. The detector, placed at 58 cm from the sample, consisted of a scintillation screen, an 8$\times$ magnifying visible light optics and a PCO Edge sCMOS camera, with effective pixel size of 0.8 μm. The difference in absorption between PEEK and water at 9.7 keV is only 0.02

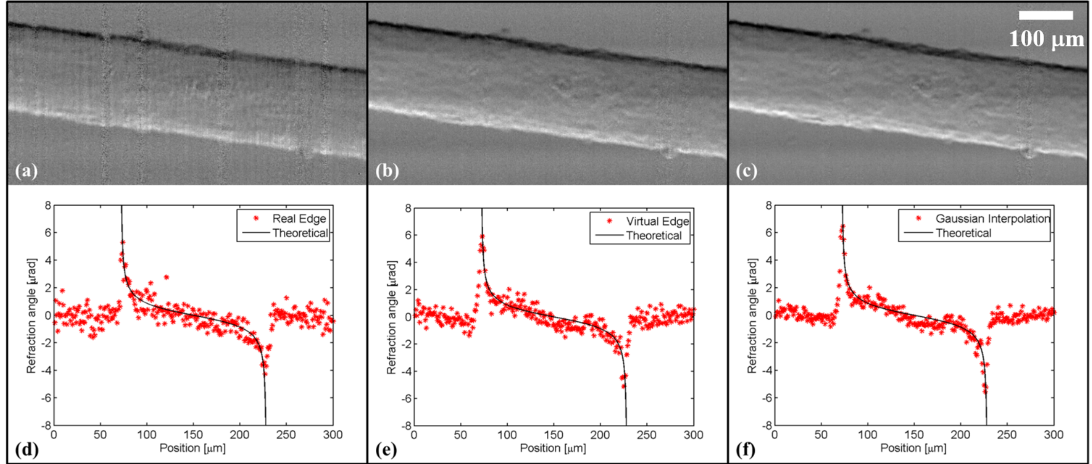

Figure 4.3: Refraction signals of a PEEK monofilament immersed in water using the real (a) and virtual (b) edge configurations, and the beam tracking (c) method. In (d), (e) and (f) a vertical profile extracted from each image is compared to the theoretical refraction angle.

%, and, for the sample in Fig. 4.3, the absorption signal is below the noise level in our acquisitions. Scattering is assumed to be negligible, and the procedure described in [46] was used for the retrieval. This retrieval procedure can be seen as a particular case of the more general retrieval approach described in the previous section, and considers the situation in which the detector slit aperture is larger than the incident beam. With reference to Fig. 4.1, two different images are required, one in which the upper edge of the detector slit absorbs the upper half of the incident beam and vice versa [46]. Two separate scans of the sample are therefore needed with the classical edge illumination, while with the virtual edge approach two different Heaviside functions are applied to the same experimental dataset. This results in a similar image quality, but with a reduction of exposure time and delivered dose by a factor of 2 in the latter case. Most importantly, a single scan of the sample is performed, which minimizes the effects of possible sample movements (e.g. for *in vivo* or dynamic applications). Figs.

4.3 (d) and (e) show the comparison between a vertical profile of the images (a) and (b), respectively, and the theoretical refraction angle: in both cases, a good agreement is found. The described approach has the advantage of being easily implementable in previously developed techniques for absorption and refraction retrieval [27, 28, 46].

4.3 Beam tracking

The edge illumination technique was designed to detect beam variations on the detector by using an edge as analyser [25], and the virtual edge approach implements the same concept via software. However, the beam intensity profile, and the changes it suffers when a sample is introduced, can be detected directly by an high resolution detector. By tracking the beam variations in the x direction (with respect to Fig. 4.1) through interpolation techniques it is possible to reconstruct absorption, refraction and scattering maps of the sample. A similar concept was presented in a 1995 patent by Wilkins [49], where he proposed an adaptation of the Shack-Hartmann wavefront sensor for x-ray radiation, and in the works presented in [2, 50], using, however, different phase retrieval approaches. More recently, other techniques have been proposed to track the changes introduced by a sample to a known reference field by means of a high resolution detector [51, 52, 53, 54]. More details about these methods will be discussed in the next chapter.

In our case, with reference to Fig. 4.1, following a similar analysis to the one that lead to Eq. 4.8, the effects of absorption, refraction and scattering on the

recorded intensity profile can be expressed as:

$$I(x) = T\,[I_0 * S]\,(x - \Delta x), \tag{4.16}$$

where I and I_0 are the intensity patterns measured by the detector with and without the sample, respectively; T is the fraction of the beam transmitted through the sample, Δx is the lateral shift of the beam at the detector plane caused by refraction, and the effect of scattering is described by means of a convolution with the scattering function S. It is worth noting that the illumination curve I_C in Eq. 4.8 is equal to the intensity profile incident on the detector convolved with the intensity transmission function of the detector mask. The intensity profile I_0 in Eq. 4.16, instead, is equal to the same intensity profile incident on the detector, convolved this time with the detector point spread function. With the pixel point spread function playing the role of the detector mask aperture, beam tracking is therefore mathematically equivalent to edge illumination. The aperture position p_0 in Eq. 4.8 corresponds to the pixel position x in Eq. 4.16, and the illumination curve I_C to the intensity I_0 measured without the sample. In reference [47], a normalized Gaussian distribution is assumed for $S(x)$, with standard deviation σ_S, and a Gaussian profile is also assumed for I_C; under these hypotheses, Eq. 4.8 can be solved analytically for T, Δx, and σ_S by measuring the intensity I_n for three different values of p_0. If the same hypothesis is applied to Eq. 4.16, i.e. I_0 and S are assumed to be Gaussian functions, then also the intensity I will be a Gaussian function. In this case, through a Gaussian interpolation of the experimental intensity profiles acquired with (I) and without (I_0) the sample, it is possible to determine T, Δx, and σ_S. In the more general case, I_0 can be

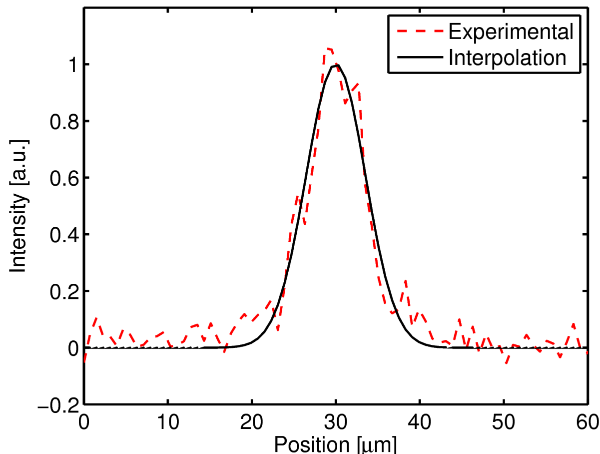

Figure 4.4: Comparison between experimental and interpolated beam intensity profile.

effectively approximated by a sum of Gaussian terms:

$$I_0(x) = \sum_{n=1}^{N} A_n \exp\left[-\frac{(x-\mu_n)^2}{2\sigma_n^2}\right], \tag{4.17}$$

with the total number of terms N depending on the specific case. In the assumption of a normalized Gaussian distribution for $S(x)$, Eq. 4.16 becomes:

$$I(x) = T\sum_{n=1}^{N} A_n \sqrt{\frac{\sigma_n^2}{\sigma_n^2+\sigma_s^2}} \exp\left[-\frac{(x-\mu_n-\Delta x)^2}{2\left(\sigma_n^2+\sigma_S^2\right)}\right]. \tag{4.18}$$

T can be calculated from the ratio between the integrals of I and I_0 along x, while a N-Gaussian interpolation of I and I_0 allows retrieving Δx and σ_S. Usually the summations in Eq. 4.17 and Eq. 4.18 present one dominant term which describes the general shape of the intensity profile, while the other terms provide a refinement of the interpolation. In principle, a better description of I and I_0 can be obtained by increasing the number of terms in Eq. 4.17 and Eq. 4.18.

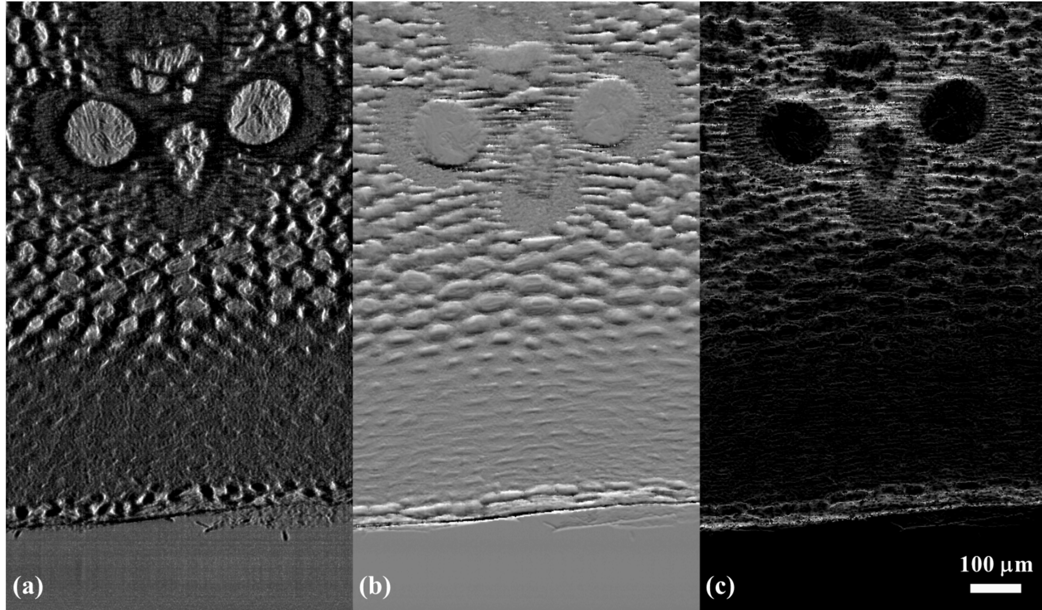

Figure 4.5: Absorption (a) refraction (b) and scattering (c) images of a bamboo wood slice obtained with the beam tracking method.

However, in the practical cases we explored, one Gaussian term was sufficient to accurately interpolate the beam profile. An example of the adequacy of this approximation is shown in Fig. 4.4, where an experimental beam intensity profile is compared with the corresponding Gaussian fit.

We first applied the beam tracking method to the PEEK monofilament immersed in water. Figures 4.3 (c) and (f) show the retrieved refraction image and the comparison with the theoretical value, demonstrating good agreement. We finally tested the method on a more complex sample, a slice of bamboo wood with approximately 500 μm thickness from a "nature-inspired" engineering project currently underway at UCL. In this case, a 3 μm slit was used as pre-sample aperture, and the sample to detector distance was reduced to 30 cm. Fig. 4.5 shows the reconstructed absorption, refraction and scattering signals. These images could also be fused together in, for example, a single RGB image (Fig. 4.6),

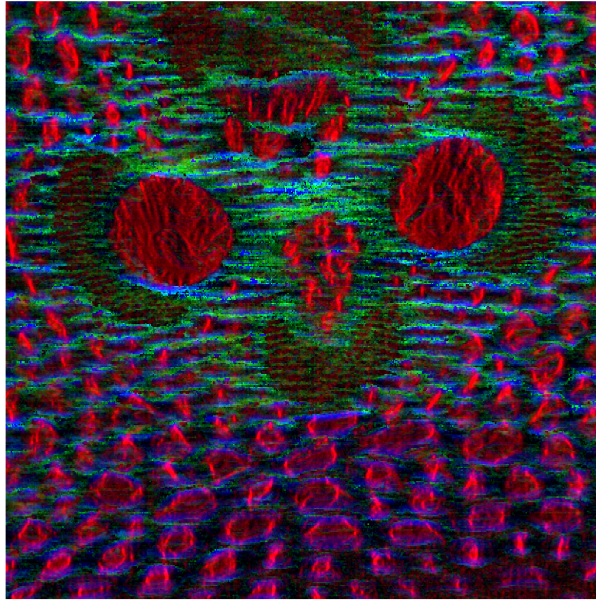

Figure 4.6: Colour rendering of the three signals in Fig. 4.5. Red represents absorption, blue the absolute value of refraction and green scattering.

to better appreciate the different contributions of the three signals. Each signal is in fact sensitive to different features of the object: usually absorption signal offers the best contrast for the low frequency part of the image, refraction is stronger at the edges of the sample structures, and scattering reveals the presence of strong variations in the sample transmission function not resolved in the absorption and refraction images. Given the relatively small thickness of the object, other techniques might be used to investigate its properties as, for example, visible light or electron microscopy, that are sensitive to the surface structures of the sample. The use of x-rays, however, opens the possibility to investigate thicker samples. In particular, a tomographic implementation of the technique would allow the extraction of the same type of images showed in Fig. 4.5 from a much thicker sample, without the need to physically section it in thin slices.

In summary, the beam tracking approach, through a simple modification of the

edge illumination setup, provides an effective method to retrieve absorption, refraction and scattering signals of a sample from the beam intensity profile acquired through a high resolution detector. Additionally, it simplifies the experimental setup and reduces the total number of images required to retrieve absorption, refraction and scattering. Like edge illumination, beam tracking does not rely on coherence to generate contrast, which allows its implementation with laboratory sources.

5

Beam tracking: laboratory implementation

In this chapter we will discuss the implementation of the beam tracking approach with a laboratory setup. The main differences with the synchrotron implementation described before are that the projected source size on the detector and the detector pixel size are considerably larger, and the radiation is polychromatic. While the first point is important for the design of the experimental apparatus, polychromaticity plays an important role in the physical information contained in the retrieved signals (absorption, refraction and scattering). In particular it will be shown that, if the model used in the synchrotron case is not properly modified to account for polychromatic radiation, the retrieved signals are affected by artefacts. A method to correct for these artefacts is here proposed, and tested through simulations and experiments. The results presented in this chapter are based on the work presented in [55].

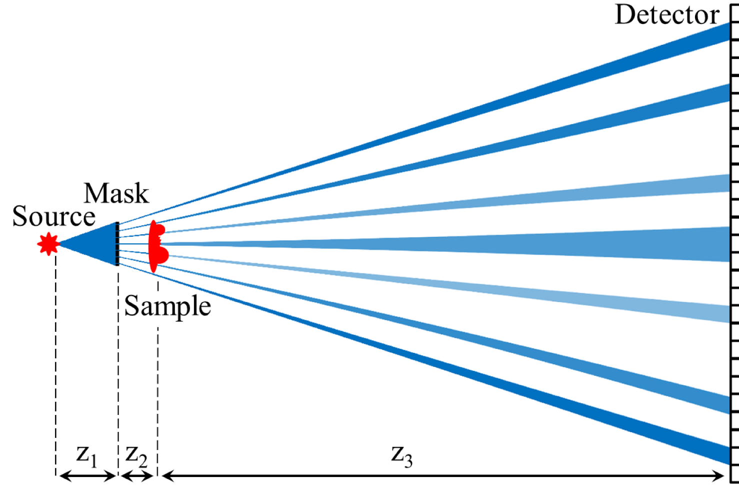

Figure 5.1: Schematic diagram of the beam tracking setup implemented with a laboratory source.

5.1 Experimental apparatus

As for the edge illumination method, the beam tracking approach is implemented in a laboratory system using an absorbing mask with a series of apertures (Fig. 5.1). In this configurations, x-rays emitted from the source create a magnified image of the mask on the detector, when no sample is present. From simple geometrical considerations, it can be shown that the magnification between the mask and the detector is $M = (z_1 + z_2 + z_3)/z_1$, which can be modified by varying the relative positions of source, mask and detector. When a high resolution detector is not available, a high magnification between mask and detector is needed in order to track each beam (Fig. 5.1). High magnification configurations have been extensively studied in the past for absorption-based x-ray microscopy [56]. It is however important to remember that the intensity measured at the detector plane is given by the one produced by a point source convolved with the rescaled source intensity distribution (Eq. 3.9). This means that the source

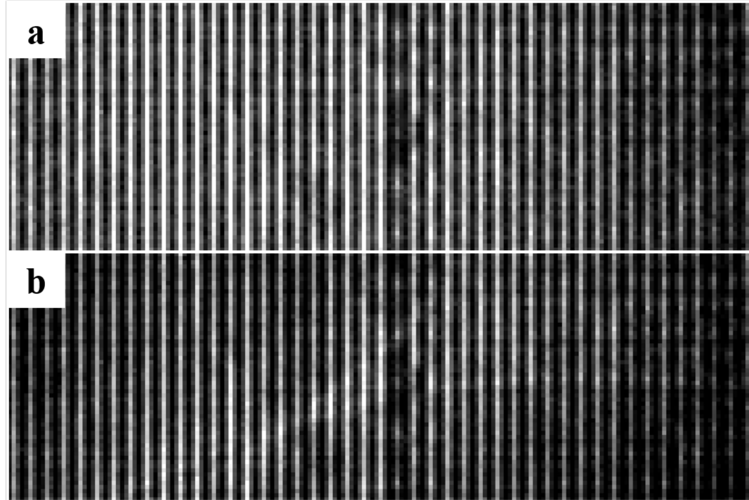

Figure 5.2: Intensity pattern produced by the absorbing mask and acquired by the detector without (a) and with (b) a sample present in the beam. The period of the intensity pattern is equal to 4 pixels (200 μm).

is effectively magnified on the detector by a factor equal to $(M - 1)$. A high magnification, therefore, implies a large projected source on the detector plane. To avoid possible ambiguity in the retrieval procedure, it is important that the beamlets created by the different apertures, and blurred due to the finite source size, remain physically separated. This results in the need of a small, micro-focal source when high magnification is used in the beam tracking approach.

The experimental setup is based on a microfocus transmission tungsten target x-ray tube, operating at 80 kVp with source size of about 3 μm. The employed distances are: source to mask $z_1 = 13.2$ cm, mask to sample $z_2 = 2.1$ cm, and sample to detector $z_3 = 116.7$ cm. The mask is made of a 200 μm thick gold layer on a silicon substrate, with aperture size and period of 3 μm and 20 μm, respectively. The detector is a passive pixel CMOS sensor (Hamamatsu Photonics C9732DK), with pixel size of 50 μm. The geometrical magnification between the mask and the detector is $M = 10$. The period of the intensity pattern at the de-

tector plane is thus 200 μm, equal to four pixels (Fig. 5.2). The system is aligned so that each beamlet hits the center of a pixel by using compact piezoelectric motors [57], and five pixels are used to track the variations of each beam.

5.2 Phase retrieval with polychromatic radiation

In this section we will analyse the role of polychromaticity in the recorded signal. This will be done by first considering the monochromatic case, for which the same image formation model derived in the previous chapter is used, and then by summing the contributions of all the energy components of the polychromatic spectrum. By doing so, we will see how radiation that is partially transmitted through the absorbing septa of the mask (due to a physical limitation of its maximum thickness) is characterized by a different spectrum with respect to the radiation that travels through the mask apertures, and it is therefore affected by the sample in a different way. This difference, if not properly considered, can be the cause of artefacts in the retrieved signals, which will be analysed in detail.

Let us first consider monochromatic radiation of energy E. An ideal absorbing mask can be described by the following complex transmission function:

$$G(x, E) = \sum_n rect\left[(x - nP)/W\right], \tag{5.1}$$

where P is the period of the mask, W is the dimension of the mask aperture, and $rect(x)$ is equal to 1 for $|x| < 1/2$ and 0 elsewhere. The transmission function of an ideal mask does not depend on the energy E of the incoming radiation;

however, when a real mask is used, part of the beam can be transmitted through the absorbing septa. Referring for simplicity to one aperture only, the intensity transmitted through a real mask can be expressed as:

$$|G(x,E)|^2 = [1 - o(E)]\, rect\, [x/W] + o(E). \tag{5.2}$$

where $o(E) = \exp\left[-2k\beta_m(E)T_m\right]$, with $\beta_m(E)$ the imaginary part of the mask refractive index, T_m the mask thickness, and $k = 2\pi/\lambda$, with λ the x-ray wavelength. In the geometrical optics approximation, which is sufficiently accurate for our experimental setup [29], the intensity recorded by each pixel can be expressed as:

$$i(x,E) = p'(E)i_f(x,E) + p''(E) \tag{5.3}$$

where $p'(E) = p(E)\,[1 - o(E)]$, $p''(E) = p(E)o(E)$, and $i_f(x,E) = rect\,[x/(MW)] * PSF(x,E)$. $p(E)$ describes the source spectral distribution combined with the detector response at energy E, and $*$ indicates the convolution with respect to the x variable. $PSF(x,E)$ is the convolution between the source intensity distribution projected at the detector plane and the detector point spread function, normalized such that $\int PSF(x,E)dx = 1$. When a sample is introduced, the intensity distribution measured by the detector can be expressed as [45]:

$$\begin{aligned} i'(x,E) &= t(E)\,[i(x-\Delta(E),E) * S(x,E)] = \\ &= t(E)p'(E)i_f(x-\Delta(E),E) * S(x,E) + t(E)p''(E), \end{aligned} \tag{5.4}$$

where $t(E)$ is the transmission through the sample, $\Delta(E)$ the shift of the beam caused by refraction, and $S(E)$ the sample scattering function. $S(E)$ is assumed

as a normalized Gaussian with standard deviation $\sigma_S(E)$. The intensities measured in the polychromatic case, with and without the sample, are then calculated by integrating Eqs. 5.3 and 5.4 over energy:

$$I(x) = \int p'(E) i_f(x, E) dE + \int p''(E) dE = I_F(x) + C_F, \tag{5.5}$$

$$I'(x) = \int t(E) p'(E) i_f(x - \Delta(E), E) * S(x, E) dE + \int t(E) p''(E) dE = I_D(x) + C_D. \tag{5.6}$$

The intensity $I(x)$ ($I'(x)$) is expressed as the sum of a function $I_F(x)$ ($I_D(x)$) that approaches 0 as x approaches $\pm\infty$, and a constant offset C_F (C_D). For the case when the sample is not present, let us consider the total intensity A_F, mean value μ_F and variance σ_F^2 of $I_F(x)$, defined as follow:

$$A_F = \int I_F(x) dx, \tag{5.7}$$

$$\mu_F = \frac{\int x I_F(x) dx}{\int I_F(x) dx}, \tag{5.8}$$

$$\sigma_F^2 = \frac{\int x^2 I_F(x) dx}{\int I_F(x) dx} - \mu_F^2. \tag{5.9}$$

For A_F we have:

$$A_F = \int I_F(x) dx = \int p'(E) \left[\int i_f(x, E) dx \right] dE. \tag{5.10}$$

From the definition of $i_f(x, E)$ and the properties of convolution, it follows that:

$$\int i_f(x,E)dx = \int rect\left[x/(MW)\right]dx \int PSF(x,E)dx = MW, \qquad (5.11)$$

and finally:

$$A_F = MW \int p'(E)dE. \qquad (5.12)$$

To calculate μ_F, let us first consider the following integral:

$$\int xI_F(x)dx = \int p'(E)\left[\int xi_f(x,E)dx\right]dE. \qquad (5.13)$$

Assuming that $PSF(x,E)$ is a symmetric function of x, $\int xi_f(x,E)dx = 0$ and:

$$\mu_F = 0. \qquad (5.14)$$

To calculate σ_F^2, let us consider:

$$\int x^2 I_F(x)dx = \int p'(E)\left[\int x^2 i_f(x,E)dx\right]dE. \qquad (5.15)$$

With the following definition:

$$\sigma_f^2(E) = \frac{\int x^2 i_f(x,E)dx}{\int i_f(x,E)dx}, \qquad (5.16)$$

we have:

$$\sigma_F^2 = \frac{\int p'(E)\sigma_f^2(E)dE}{\int p'(E)dE}. \qquad (5.17)$$

Let us now consider the total intensity A_D, mean value μ_D and variance σ_D^2

of $I_D(x)$ when the sample is present. For A_D we have:

$$A_D = \int I_D(x)dx = \int t(E)p'(E)\left[\int i_f(x-\Delta(E),E)dx\right] \times \left[\int S(x,E)dx\right] dE = MW \int t(E)p'(E)dE. \quad (5.18)$$

To calculate μ_D, let us consider:

$$\int xI_D(x)dx = \int t(E)p'(E)\left\{\int x\left[i_f(x-\Delta(E),E) * S(x,E)\right]dx\right\} dE. \quad (5.19)$$

The term in curly brackets can be expressed as:

$$\int x \int i_f(y-\Delta(E),E)S(x-y,E)dydx = = \int i_f(y-\Delta(E),E)\left[\int xS(x-y,E)dx\right] dy = = \int yi_f(y-\Delta(E),E)dy = \int (z+\Delta(E))i_f(z,E)dz = MW\Delta(E), \quad (5.20)$$

where we used $\int xS(x-y,E)dx = y$. Substituting the last result in Eq. 5.19, we have:

$$\int xI_D(x)dx = MW \int t(E)p'(E)\Delta(E)dE, \quad (5.21)$$

and:

$$\mu_D = \frac{\int t(E)p'(E)\Delta(E)dE}{\int t(E)p'(E)dE}. \quad (5.22)$$

To calculate σ_D^2, let us consider:

$$\int x^2 I_D(x)dx = \int t(E)p'(E)\left\{\int x^2\left[i_f(x-\Delta(E),E) * S(x,E)\right]dx\right\} dE. \quad (5.23)$$

The term in curly brackets can be expressed as:

$$\int x^2 \int i_f(y-\Delta(E),E)S(x-y,E)dydx = \\ = \int i_f(y-\Delta(E),E)\left[\int x^2 S(x-y,E)dx\right]dy. \quad (5.24)$$

The integral over x can be written as:

$$\int x^2 S(x-y,E)dx = \int (z+y)^2 S(z,E)dz = \\ = \int z^2 S(z,E)dz + y^2 = \sigma_S^2(E) + y^2, \quad (5.25)$$

where $\sigma_S^2(E) = \int z^2 S(z,E)dz$ is the variance of $S(z,E)$. Substituting the last result in Eq. 5.24, we have:

$$\int x^2 \int i_f(y-\Delta(E),E)S(x-y,E)dydx = \\ = \int y^2 i_f(y-\Delta(E),E)dy + MW\sigma_S^2(E) = \\ = \int (z+\Delta(E))^2 i_f(z,E)dz + MW\sigma_S^2(E) = \\ = \int z^2 i_f(z,E)dz + MW\Delta^2(E) + MW\sigma_S^2(E), \quad (5.26)$$

and:

$$\sigma_D^2 = \frac{\int t(E)p'(E)\sigma_f^2(E)dE}{\int t(E)p'(E)dE} + \frac{\int t(E)p'(E)\Delta^2(E)dE}{\int t(E)p'(E)dE} \\ + \frac{\int t(E)p'(E)\sigma_S^2(E)dE}{\int t(E)p'(E)dE} - \left[\frac{\int t(E)p'(E)\Delta(E)dE}{\int t(E)p'(E)dE}\right]^2. \quad (5.27)$$

The variations between these parameters can be used to retrieve the sample

transmission (T), refraction (R) and scattering (σ_S^2) signals, given by the following expressions:

$$T = \frac{A_D}{A_F} = \frac{\int t(E)p'(E)dE}{\int p'(E)dE}, \tag{5.28}$$

$$R = \mu_D - \mu_F = \frac{\int t(E)p'(E)\Delta(E)dE}{\int t(E)p'(E)dE}, \tag{5.29}$$

$$\begin{aligned} \sigma_S^2 = \sigma_D^2 - \sigma_F^2 = & \frac{\int t(E)p'(E)\sigma_s^2(E)dE}{\int t(E)p'(E)dE} \\ & + \frac{\int t(E)p'(E)\Delta^2(E)dE}{\int t(E)p'(E)dE} - \left[\frac{\int t(E)p'(E)\Delta(E)dE}{\int t(E)p'(E)dE}\right]^2 \\ & + \frac{\int t(E)p'(E)\sigma_f^2(E)dE}{\int t(E)p'(E)dE} - \frac{\int p'(E)\sigma_f^2(E)dE}{\int p'(E)dE}. \end{aligned} \tag{5.30}$$

T is the ratio between the total intensity of the beam with and without the sample, and is effectively the weighted average of $t(E)$ over the spectrum $p'(E)$. R indicates the average shift of the beam induced by refraction, and is equal to the weighted average of $\Delta(E)$ over the spectrum $p'(E)$ multiplied by $t(E)$, which can be seen as an "effective spectrum" in the presence of the sample. The expression for the scattering signal is more complex, and consists of different terms. The first term in the first line of Eq. 5.30 is the weighted average of $\sigma_S^2(E)$ over the effective spectrum $t(E)p'(E)$, and represents the "pure" scattering term. The second line of Eq. 5.30 is equal to the variance of $\Delta(E)$ calculated over the effective spectrum $t(E)p'(E)$, and explains how the variation of the refraction angle with energy results in an overall broadening of the beam, which will be measured as a scattering signal. The third line of Eq. 5.30 is a residual error in the normalization by the flat field signal σ_F^2, and depends on the difference in the spectrum without ($p'(E)$) and with ($p'(E)t(E)$) the sample. For a non-absorbing

sample this term would be equal to 0.

Let us assume that $I_F(x)$ and $I_D(x)$ can be approximated by Gaussian functions [45, 47], that the system is aligned so that $\mu_F = 0$, and that A_F and σ_F are known from an independent measurement without the sample. With these hypotheses, it is possible to retrieve T, R and σ_S^2 by interpolating the intensity distribution $I'(x)$ measured by the detector with a Gaussian function, representing $I_D(x)$, plus a constant term, representing C_D.

5.3 Comparison with other phase retrieval methods

In chapter 2 we described some of the main phase contrast imaging methods. Recently, however, alternative "single-shot" methods have been proposed [51, 52, 53, 54], in which a reference pattern is created using either a sheet of sandpaper or the Talbot self-image from a phase grating, and correlation methods are used to analyse the local pattern distortions caused by a sample. While most of these were implemented at synchrotrons, Zanette *et al* [54] extracted absorption, refraction, and dark-field (i.e. scattering) signals from a speckle pattern using a laboratory setup. However, a speckle pattern will, in general, have a wide range of features with different size and intensity, resulting in a change of resolution and sensitivity across the image which could be difficult to control. This is not the case if the Talbot self-image of a grating is used; however, gratings employed at x-ray wavelengths typically have pitches of few micron, and a very high resolution detector is needed to resolve the intensity pattern. Moreover, the distance from

the grating at which the self-image is created is energy dependent, resulting in a reduced pattern visibility when polychromatic sources are used.

Methods similar to beam tracking have also been proposed [2, 50], using, however, different phase retrieval approaches. In the method proposed by Krejci *et al* [50], two pixels per beam are illuminated (four in the 2-D case), and analytical formulae are derived to calculate absorption and refraction. These, however, are based on a simplified description of the experimental setup that does not take into account important parameters such as source size, transmission through the mask, and pixel point spread function. In the method proposed by Wen *et al* [2], the above signals plus dark-field are retrieved by performing a Fourier-analysis of the intensity pattern.

Let us consider in more details this method. The Fourier-analysis considers the entire intensity pattern measured by the detector, while in beam tracking each individual beam is analysed independently from the others. The intensity pattern created by a perfect mask is periodic, and its Fourier transform is different from zero only for spatial frequencies multiples of the basic harmonic $\bar{\xi} = 1/(MP)$. Let us indicate this intensity pattern with $I_w(x)$, and its Fourier transform with $\hat{I}_w(\xi)$. It is possible to write:

$$\hat{I}_w(\xi) = \sum_{n=-\infty}^{\infty} c_n \delta_D \left(\xi - n\bar{\xi}\right), \tag{5.31}$$

where δ_D is the Dirac delta, and:

$$c_n = \bar{\xi} \int_0^{1/\bar{\xi}} I_w(x) \exp\left(-2\pi i n \bar{\xi} x\right) dx. \tag{5.32}$$

It is important to stress that $I_w(x)$ indicates the intensity measured by the entire detector, while for the beam tracking case $I(x)$ was used to indicate the local intensity distribution generated by one aperture of the mask. Absorption, refraction and scattering caused by the sample distort the periodic pattern. Let us consider the simple case in which only absorption is present; in the Fourier-analysis method this is modelled as a multiplication by a sample transmission function. In this case the intensity pattern $I'_w(x)$ and its Fourier transform $\hat{I}'_w(\xi)$ can be written as:

$$I'_w(x) = T_w(x) I_w(x), \tag{5.33}$$

$$\hat{I}'_w(\xi) = \hat{T}_w(\xi) * \hat{I}_w(\xi) = \sum_{n=-\infty}^{\infty} c_n \hat{T}_w\left(\xi - n\bar{\xi}\right) = \sum_{n=-\infty}^{\infty} \hat{I}'_{w,n}\left(\xi - n\bar{\xi}\right), \tag{5.34}$$

where $T_w(x)$ indicates the sample transmission function, and $\hat{T}_w(\xi)$ its Fourier transform. $\hat{I}'_w(\xi)$ is equal to the sum of the *harmonic spectra* $\hat{I}'_{w,n}(\xi)$, each shifted by a quantity $n\bar{\xi}$. If the different harmonic spectra do not overlap, i.e. if the bandwidth of each spectrum is smaller than $\bar{\xi}$, it is possible to retrieve the n-th spectrum by isolating a region of width $\bar{\xi}$ around $n\bar{\xi}$. By performing an inverse Fourier transform of the n-th harmonic spectrum one obtains an *harmonic image* $I'_{w,n}(x)$ of the sample. In the simple example considered, in which the sample only absorbs radiation, all the harmonic spectra are equal, apart from a constant factor, to the Fourier transform $\hat{T}_w(\xi)$ of the sample transmission function $T_w(x)$, and all the harmonic images will therefore be proportional to the sample transmission function. The harmonic images will in general be different when

transmission, refraction and scattering are considered, and these quantities can be extracted using the following equations:

$$T_w(x) = \frac{I'_{w,0}(x)}{c_0}; \tag{5.35}$$

$$R_w(x) = -\frac{1}{2\pi i\bar{\xi}}\arg\left[\frac{I'_{w,1}(x)}{I'_{w,0}(x)}\frac{c_0}{c_1}\right]; \tag{5.36}$$

$$\sigma^2_{S,w}(x) = -\frac{1}{2\pi^2\bar{\xi}^2}\log\left[V_w(x)\right]; \tag{5.37}$$

where:

$$V_w(x) = \text{abs}\left[\frac{I'_{w,1}(x)}{I'_{w,0}(x)}\frac{c_0}{c_1}\right]. \tag{5.38}$$

In the above equations the transmission T_w corresponds to a local variation of the mean value of the periodic pattern, the refraction R_w is equal to the local lateral displacement of the pattern caused by the sample, while the scattering signal is derived from the quantity V_w. In a simplified case in which the intensity distribution can be expressed as $I_w(x) = a_0 + a_1 \sin(2\pi\bar{\xi}x + \phi_1)$, V_w is equal to the variation of the *visibility* of this intensity distribution, which is defined as $V = (I_{w,max} - I_{w,min})/(I_{w,max} + I_{w,min})$, with $I_{w,max}$ and $I_{w,min}$ the maximum and minimum values of the intensity pattern, respectively. When this model is applied to the theoretical framework developed in the previous section, it implies that locally the intensity distribution with and without the sample can be related by the following equation:

$$I'_w(x) = T_w I_w(x - R_w) * S_w(x), \tag{5.39}$$

where S_w is the scattering function. Equation 5.39 is used here to describe the

effect of the sample on a limited region of the intensity pattern, on the order of one period of the mask, so that T_w, R_w and the standard deviation $\sigma^2_{S,w} = \int x^2 S_w(x)dx$ can all be considered constant. Note that the loss in visibility, as described for the Fourier-analysis, comes naturally from the convolution with the scattering function S_w. Equation 5.39 is equivalent to Eq. 5.4, the main difference being that Eq. 5.4 refers to a single, monochromatic component of the electromagnetic radiation, while Eq. 5.39 describes the full polychromatic spectrum. Let us write Eq. 5.39 as:

$$I'_w(x) = T_w I_F(x - R_w) * S_w(x) + T_w C_F = I_D(x) + C_D. \tag{5.40}$$

The quantity R in Eq. 5.29 is equivalent to R_w, as both represent the difference in the mean values between I_F and I_D. It is importance to note, instead, how in the Fourier-analysis method the reduction due to absorption between I_F and I_D and between C_F and C_D is the same, equal to T_w. In our model, the absorption between I_F and I_D (T) and between C_F and C_D are, in general, different. Let us compare the two models in a simplified case in which no refraction and/or scattering are present. In this case our model predicts:

$$I'(x) = T I_F(x) + T_0 C_F, \tag{5.41}$$

with $T_0 = \int t(E)p''(E)dE / \int p''(E)dE$. The Fourier-analysis model predicts:

$$I'_w(x) = T_w I_F(x) + T_w C_F. \tag{5.42}$$

According to our model, when $T \neq T_0$ the visibility between $I'(x)$ and $I(x)$ varies,

and this visibility variation is not related to the presence of a scattering signal. In the Fourier-analysis method, however, it is implicitly assumed $T = T_0 = T_f$, and any variation in the visibility of the intensity pattern will be retrieved as a scattering signal. Finally, it is important to note that the model expressed in Eq. 5.39 is also assumed in other phase contrast methods such as grating interferometry [58] and edge illumination [47].

5.4 Simulation results

We compared our phase retrieval method and the Fourier-analysis on simulated data. The simulation is based on the wave theory of x-ray propagation in matter and free space described in chapter 2. We considered a tungsten target x-ray source operating at 80 kVp with 3 μm FWHM, placed at 13.2 cm from the mask and 132 cm from the detector. The sample, a 2.56 mm diameter glass sphere, is assumed to be in the same plane as the mask. The mask period and aperture size are 20 μm and 3 μm, respectively. The absorbing septa are assumed to be made of a 200 μm thick gold layer. The detector pixel size is 50 μm. The intrinsic resolution of the system is comparable to the aperture width of the mask [59, 60], and is therefore smaller than the mask period (which represents the rate at which the signal is sampled in a single exposure). To illuminate all the sample and avoid aliasing, a 16-step sub-pixel scan along the direction orthogonal to the aperture lines is simulated. This scan procedure is called *dithering*, and is very often used in edge illumination systems. The steps were then averaged in groups of 4 and recombined together in a single, oversampled, image. While the average of the dithering steps is not necessary, it was performed to simulate the

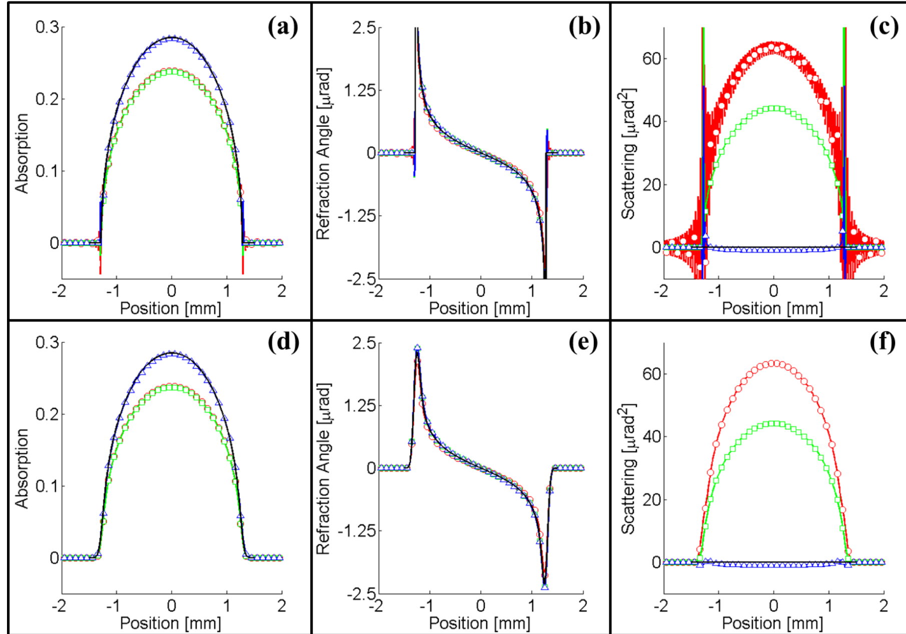

Figure 5.3: Absorption ($-\log T$) (a,d), refraction (R/z_3) (μrad) (b,e), and scattering (σ_S^2/z_3^2) (μrad^2) (c,f) signals retrieved from the simulation. The sample is a glass sphere of 2.56 mm diameter for the profiles (a-c), while for (d-f) the same sphere is convolved with a Gaussian function of $\sigma = 50$ μm. The retrieved signal for the Fourier-analysis, Gaussian interpolation, and its modified version are shown in red (circular markers), blue (triangular markers), and green (square markers), respectively; while the expected signal is shown in black.

experimental acquisition described in the next section. All the parameters used in the simulation, in fact, are chosen to resemble the experimental conditions of the data presented in the next section.

The simulated data are then processed with three different phase retrieval algorithms: the Fourier-analysis method, the Gaussian interpolation described above, and a modified version in which we assume that the absorption T between $I_D(x)$ and $I_F(x)$, and T_0 between C_D and C_F are equal. The Fourier-analysis method assumes that the harmonic spectra of the measured periodic pattern do not overlap [2]. To understand how the retrieved signal is altered when this condition is not satisfied, we performed two series of simulations: one simulating

a perfect sphere, and one in which the sphere projected thickness is convolved with a Gaussian function of $\sigma = 50$ μm. In the first case we expect the harmonic spectra to overlap due to the sharp thickness variation at the edges of the sphere, while in the second case the smoothing effect of the convolution with the Gaussian allows us to avoid this. The results and the comparison with the expected values are presented in Fig. 5.3. Figs. 5.3 (a-c) show the results obtained for the perfect sphere, while Figs. 5.3 (d-f) show those for the "smoothed" sphere. The retrieved signals for the Fourier-analysis, Gaussian interpolation, and its modified version are shown in red (circular markers), blue (triangular markers), and green (square markers), respectively; while the expected signal is shown in black. As expected, when the Fourier-analysis is applied to the perfect sphere case, artefacts coming from the overlap of the Fourier spectra are visible in the reconstructed profiles as high frequency oscillations; those are particularly evident in the scattering profile. The main shape of the signal, however, remains unchanged. Most importantly, a spurious scattering signal is observed with the Fourier-analysis method and with the modified version of the Gaussian interpolation both in the perfect and smoothed sphere case; as explained before, this depends on the assumption $T = T_0$. It is also possible to note how the retrieved absorption signal is lower than the expected one for these two methods, while the refraction signal is correctly retrieved in all cases.

5.5 Experimental results

We tested our method on a series of glass spheres, the leg of a beetle, and a wood sample. A 16-step sub-pixel scan along the direction orthogonal to the aperture

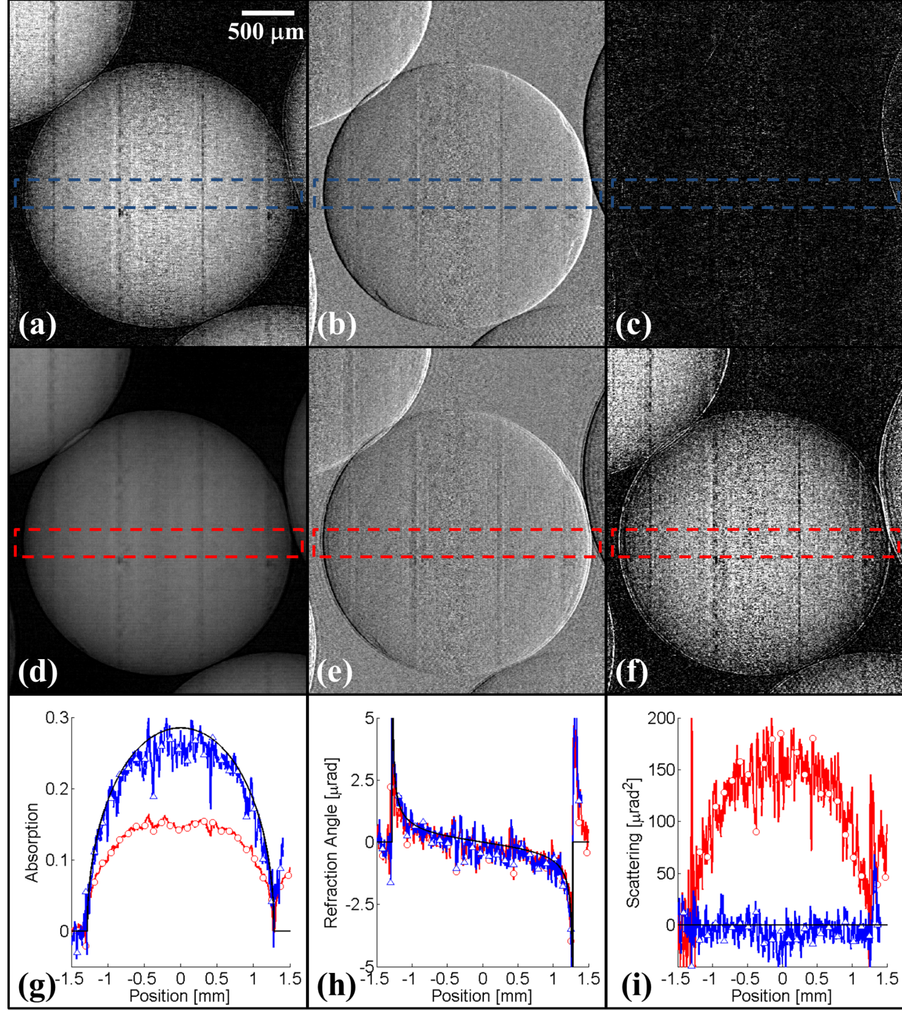

Figure 5.4: Absorption ($-\log T_1$) (a), refraction (R/z_3) (μrad) (b), and scattering (σ_S^2/z_3^2) (μrad^2) (c) signals retrieved from glass spheres using the proposed method. (d), (e) and (f) show the same signals retrieved using Fourier-analysis [2]. In (g), (h) and (i) line profiles are extracted from the images (blue line and triangular marker for our method, red line and circular marker for Fourier-analysis), and compared with the expected value (black line).

lines was performed (dithering). The steps were then averaged in groups of 4, to obtain a final image with equal sampling step in the two directions (5.8 μm), and to reduce the noise. While this means that more than one exposure was acquired, the sub-pixel scan can be avoided in those cases where a final resolution in the

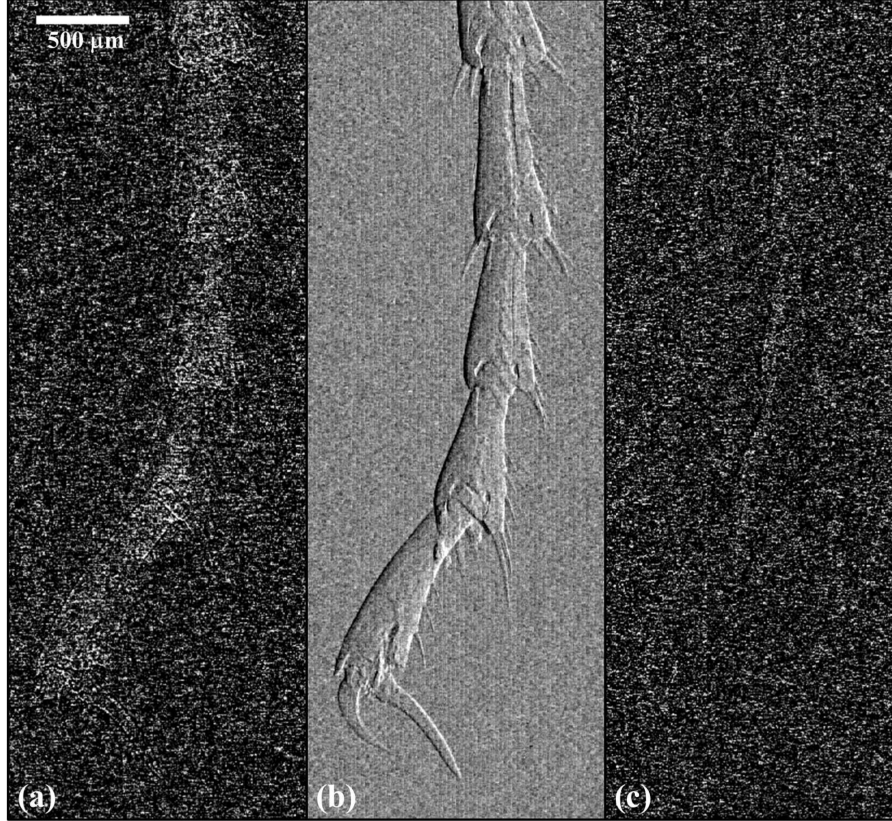

Figure 5.5: Absorption ($-\log T$) (a), refraction (R/z_3) (μrad) (b), and scattering (σ_S^2/z_3^2) (μrad^2) (c) signals retrieved from the leg of a beetle.

scanning direction equal to the mask period can be accepted. 20 exposures of 10 s were acquired for each step. Two flat field images were acquired, one before and one after the sample acquisition, with 40 exposures of 10 s each. I_F was measured by scanning the sample mask over 20 μm (one mask period) with 12 steps of 10 s each. The detector dark current was estimated by averaging 10 exposures of 10 s without x-rays, then subtracted from all the acquired images. To reduce artefacts from mask imperfections, the images acquired with the sample were normalized by the flat field.

The result of the retrieval procedure using the Gaussian interpolation on the

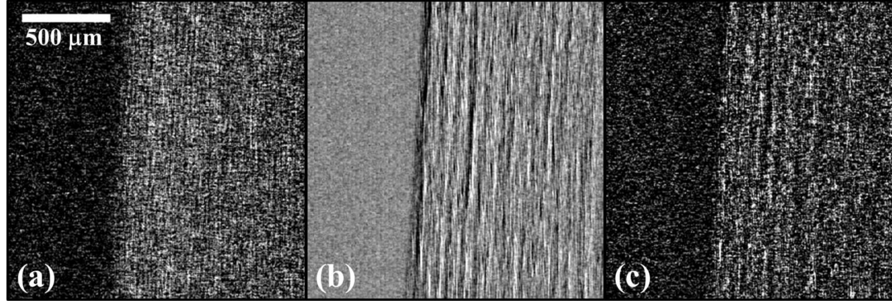

Figure 5.6: Absorption ($-\log T$) (a), refraction (R/z_3) (μrad) (b), and scattering (σ_S^2/z_3^2) (μrad^2) (c) signals retrieved from a wood section.

spheres sample is shown in Figs. 5.4 (a-c). No scattering signal is visible, as expected for a homogeneous sample. The results obtained with the Fourier-analysis are shown in Fig. 5.4 (d-f). A quantitative comparison between retrieved and theoretical signals is shown in Fig. 5.4 (g-i), with transmission and refraction calculated using Eqs. 5.28 and 5.29, and the theoretical scattering signal assumed to be 0. While our method yields good agreement, Fourier-analysis provides a signal lower than expected in absorption, and a relatively strong spurious scatter signal. As explained in the previous sections, this is an artefact caused by the visibility variation caused by absorption.

Fig. 5.5 shows the results obtained from the beetle leg. No scattering signal is visible, and absorption is very weak; however, a strong refraction signal is detected, highlighting the importance of phase-contrast imaging for low absorbing materials. Finally, Fig. 5.6 shows the signals extracted from the wood sample, which we imaged because it is known to contain structures at different length scales. This results in features with dimensions smaller than the mask aperture producing the signal visible in the scatter image, while larger features produce a refraction signal.

5.6 Discussion

Our study shows how the beam tracking approach can be implemented with a laboratory setup. For this proof-of-concept experiment, a micro-focal source was used with a high magnification, primarily to use a standard detector with 50 μm pixel size. This results in long exposure times and relatively noisy final images. The method, however, can be easily extended to lower magnification values by using a detector with a smaller pixel size. Future studies will be directed towards the optimization of the experimental parameters, with the aim to establish the optimum trade-off between source size and detector resolution.

An important result obtained in our study regards the role of polychromaticity on the retrieved values of absorption, refraction and scattering. We showed, in particular, how the model generally used to describe the effect of the sample on the reference beam can result in severe artefacts when polychromatic radiation is used, and we proposed a new model which corrects for these artefacts.

The high magnification used in the presented setup results in a relatively high final resolution, of the order of ≈ 3 μm (equal to the mask aperture). Similar and even better resolution values can be easily achieved with other imaging techniques, and in particular in visible light microscopy. However, the key advantage of the proposed method is the possibility to investigate the internal structure of samples that are not transparent to visible light.

6

Beam tracking: tomographic implementation

Computed tomography is a technique which is extensively used in standard absorption-based x-ray imaging, from which it is possible to reconstruct the three-dimensional map of the imaginary part of the sample refractive index $\beta(x, y, z)$. As described in chapter 2, a single image acquired in the absorption-based configuration provides the quantity $M(x, y) = k \int_0^l \beta(x, y, z)dz$, where $k = 2\pi/\lambda$, λ is the x-ray wavelength, l is the object thickness, and z is the x-ray propagation direction. $M(x, y)$ is usually called "projection", as it is the result of a line integral of $\beta(x, y, z)$ along the x-ray propagation direction. In computed tomography several projections $M_\theta(x, y)$ are acquired rotating the sample along an axis perpendicular to the x-ray propagation direction, for different values of the rotation angle θ. From this set of projections, it is then possible to reconstruct $\beta(x, y, z)$.

Computed tomography is not only implemented in standard absorption imaging, but also in phase contrast and ultra-small-angle-scattering imaging. In this

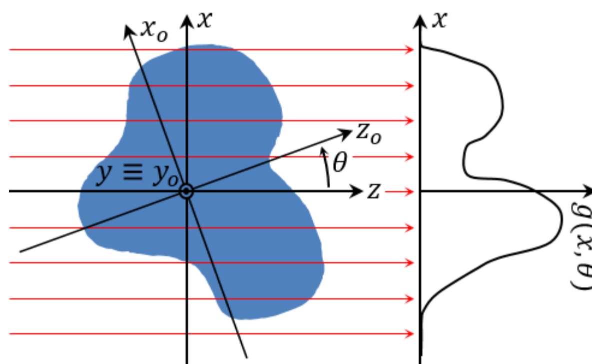

Figure 6.1: Frame of reference for a rotating object in a tomographic configuration.

chapter we will present the tomographic implementation of the beam-tracking approach using synchrotron radiation. The results shown are based on the work presented in [61]. In particular, we will show how the three signals retrieved from a single projection can all be used to reconstruct three dimensional maps of three complementary properties of the sample.

6.1 Mathematical background

We introduce here the main mathematical concepts of tomographic reconstructions. A more detailed description can be found in standard textbooks [62, 63, 64]. Let us consider an object and two frames of reference (x, y, z) and (x_o, y_o, z_o) as shown in Fig. 6.1. (x_o, y_o, z_o) is obtained by rotating (x, y, z) by an angle θ around the y axis; note that $y_0 \equiv y$. The object rotates together with the (x_o, y_o, z_o) reference frame, and let us assume that the function $f(x_o, y_o, z_o)$ describes a particular property of the object (for example f could be equal to the imaginary part β of the complex refractive index). In the (x, y, z) reference frame the object can be described by a function $f_\theta(x, y, z)$, which varies with the rotation angle θ. Let us

consider a single plane $y \equiv y_o = \bar{y}$ and let us assume that in this plane, for any value of the angle θ, we can measure the integral over every line parallel to the z axis of f:

$$\begin{aligned} \mathcal{R}\left[f(x_o, z_o)\right](x, \theta) = g(x, \theta) = \int f_\theta(x, z)dz = \\ = \int f(x\cos\theta - z\sin\theta, x\sin\theta + z\cos\theta)dz. \end{aligned} \quad (6.1)$$

where the dependency on $y \equiv y_o = \bar{y}$ has been omitted. g is called the *Radon transform*, or *sinogram*, of f and is indicated here with the operator $\mathcal{R}$. The problem of computed tomography consists in inverting the Radon transform operator in order to reconstruct the function f from the knowledge of its Radon transform g. An analytical solution to this problem is offered by the *filtered back projection* operator, defined as follow:

$$\begin{aligned} f(x_o, z_o) = FBP\left[g(x, \theta)\right](x_o, z_o) = \\ = \frac{1}{2\pi}\int_0^\pi \mathcal{F}_k^{-1}\left\{|k|\mathcal{F}_x\left[g(x, \theta)\right](k)\right\}(x_o\cos\theta + z_o\sin\theta)d\theta, \end{aligned} \quad (6.2)$$

where FBP indicates the filtered back projection operator, and $\mathcal{F}_x$ and $\mathcal{F}_k^{-1}$ indicate the Fourier transform with respect to the x variable and the inverse Fourier transform with respect to the k variable, respectively. Introducing the function:

$$h(x, \theta) = \mathcal{F}_k^{-1}\left\{|k|\mathcal{F}_x\left[g(x, \theta)\right](k)\right\}(x), \quad (6.3)$$

Eq. 6.2 can be written as:

$$f(x_o, z_o) = \frac{1}{2\pi} \int_0^{\pi} h(x_o \cos\theta + z_o \sin\theta, \theta) d\theta. \tag{6.4}$$

$h(x, \theta)$ can be seen as a sinogram obtained by filtering $g(x, \theta)$ in the Fourier space using the so-called Ram-Lak filter $|k|$. Equation 6.4 is usually called back projection, and represents the dual operator of $\mathcal{R}$.

Alternative approaches exists, which solve the tomographic problem within the theory of linear inverse problems, using iterative reconstruction algorithms. Iterative methods can offer substantial advantages over filtered back projection, at the cost of a more complex and computationally demanding reconstruction procedure. Investigating the use of iterative methods was considered beyond the scope of this work, and the more conventional approach based on the FBP operator will be used, instead.

The key point of x-ray tomography is that, provided we can measure a quantity that can be expressed as a line integral along the photons path of a function f describing a fundamental property of the sample, it is possible to reconstruct the three dimensional map of the function f, by performing a series of acquisition varying the angle between the photons path and the sample. In the next section it will be shown how tomographic reconstructions can be applied to all three signal extracted with the beam tracking method.

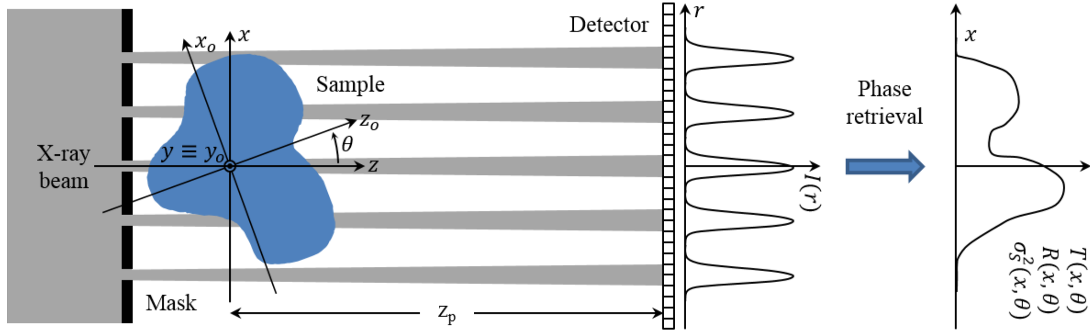

Figure 6.2: Schematic diagram of the experimental setup.

6.2 Beam tracking tomography

Let us consider the beam tracking setup in Fig. 6.2. Each beam, created by the absorbing mask, passes through the object and, after a propagation z_p, is recorded by a high resolution detector. The sample is allowed to rotate around the y axis. From the analysis of each beam, it is possible to reconstruct the transmission T, refraction R, and scattering σ_S^2 signals of the sample. These quantities are calculated assuming that for each individual beam the intensity profile $I(r)$, measured with the sample, and $I_0(r)$, measured without the sample, can be related by the following equation:

$$I(r) = TI_0(r - R) * S(r), \tag{6.5}$$

where r is the coordinate of the detector pixels, used to measure the beam profile, and σ_S^2 is the variance of the scattering distribution S.

Let us consider a single plane $y = \bar{y}$, which allows us to omit the dependency on y in the following equations. For a given angle θ, let $T(x, \theta)$, $R(x, \theta)$ and $S(x, \theta, r)$ be the transmission, refraction and scattering distribution, respectively,

relative to a beam passing through the sample in the x position. $T(x,\theta)$ can be used to calculate the absorption coefficient $\mu(x,\theta)$, which can be expressed as:

$$\begin{aligned}\mu(x,\theta) &= -\log T(x,\theta) = \frac{4\pi}{\lambda}\int \beta_\theta(x,z)dz = \\ &= \frac{4\pi}{\lambda}\int \beta(x\cos\theta - z\sin\theta, x\sin\theta + z\cos\theta)dz = \frac{4\pi}{\lambda}\mathcal{R}\left[\beta(x_o,z_o)\right](x,\theta),\end{aligned} \tag{6.6}$$

from which it follows:

$$\beta(x_o,z_o) = FBP\left[-\frac{\lambda}{4\pi}\log T(x,\theta)\right](x_o,z_o). \tag{6.7}$$

Similarly, from the lateral shift $R(x,\theta)$ of the beam it is possible to calculate the refraction angle $\alpha(x,\theta)$, which can be expressed as:

$$\begin{aligned}\alpha(x,\theta) &= \frac{R(x,\theta)}{z_p} = \frac{\partial}{\partial x}\int \delta_\theta(x,z)dz = \\ &= \frac{\partial}{\partial x}\int \delta(x\cos\theta - z\sin\theta, x\sin\theta + z\cos\theta)dz = \frac{\partial}{\partial x}\mathcal{R}\left[\delta(x_o,z_o)\right](x,\theta).\end{aligned} \tag{6.8}$$

The above relationship can be written in the Fourier space as:

$$\mathcal{F}_x\left[\alpha(x,\theta)\right](k) = ik\mathcal{F}_x\left\{\mathcal{R}\left[\delta(x_o,z_o)\right](x,\theta)\right\}(k). \tag{6.9}$$

Substituting the above equation in the FBP formula (Eq. 6.2) for $\delta(x_o,z_o)$, we find that:

$$\delta(x_o,z_o) = \frac{1}{2\pi}\int_0^\pi \mathcal{F}_k^{-1}\left\{H(k)\mathcal{F}_x\left[\alpha(x,\theta)\right](k)\right\}(x_o\cos\theta + z_o\sin\theta)d\theta, \tag{6.10}$$

where $H(k) = -i\ \mathrm{sign}(k)$ is called the Hilbert filter. $\mathrm{sign}(k) = |k|/k$ for $k \neq 0$ and

$\text{sign}(k) = 0$ for $k = 0$. This result was first derived in 1988 for beam-deflection optical tomography [65], and later applied to x-ray phase contrast imaging in 2007 [66]. The above equation is conceptually equivalent to the FBP formula, with the exception that the Ram-Lak filter is replaced with the Hilbert filter. We can rewrite Eq. 6.10 as:

$$\delta(x_o, z_o) = FBP_H \left[\frac{R(x, \theta)}{z_p} \right] (x_o, z_o), \tag{6.11}$$

where FBP_H indicates a filtered back projection performed using the Hilbert filter instead of the Ram-Lak filter.

Following the work in [67], the scattering distribution $S(x, \theta, r)$ can be interpreted as the probability density function of a photon to be scattered at an angle r/z_p from its original direction. Let us divide the photon path within the sample in a series of small regions $[z_i, z_i + dz_i]$, with $i = 1, \ldots, N$, in each of which the scattering properties of the object can be considered homogeneous. The probability density function of a photon to be scattered at an angle r/z_p when passing through the i-th region can be written as $S_\theta(x, z_i, r) = s_\theta(x, z_i, r)dz_i$. The total probability density function $S(x, \theta, r)$ is equal to the convolution of all the local probability density functions $S_\theta(x, z_i, r)$:

$$S(x, \theta, r) = s_\theta(x, z_1, r) * s_\theta(x, z_2, r) * \ldots * s_\theta(x, z_N, r)dz_1 dz_2 \ldots dz_N. \tag{6.12}$$

The variance $\sigma_S^2(x, \theta)$ of the total probability density function $S(x, \theta, r)$ is equal to the sum of the variances of the local probability density functions $S_\theta(x, z_i, r)$;

in the limit for $dz_i \to 0$, this can be written as:

$$\sigma_S^2(x,\theta) = \int \sigma_{s,\theta}^2(x,z)dz = \\ = \int \sigma_s^2(x\cos\theta - z\sin\theta, x\sin\theta + z\cos\theta)dz = \Re\left[\sigma_s^2(x_o,z_o)\right](x,\theta), \tag{6.13}$$

from which it follows:

$$\sigma_s^2(x_o,z_o) = FBP\left[\sigma_S^2(x,\theta)\right](x_o,z_o). \tag{6.14}$$

The same process can be applied to all the planes perpendicular to the y axis, thus making it possible to reconstruct the three dimensional maps $\beta(x_o,y_o,z_o)$, $\delta(x_o,y_o,z_o)$ and $\sigma_s^2(x_o,y_o,z_o)$, describing the absorption, phase shift and scattering properties of the sample.

6.3 Experimental results

The tomographic implementation of the beam tracking method was experimentally validated at the I13 (Coherence branch) beamline of the Diamond Synchrotron Radiation facility (Didcot, UK) [48]. A scheme of the experimental setup is shown in Fig. 6.2. A Si(111) crystal monochromator was used to select an x-ray energy of 9.7 keV. The mask is made of a gold layer electroplated on a graphite substrate, with aperture size and period of 10 μm and 85 μm, respectively. The detector consisted of a scintillation screen, an 8× magnifying visible light optics and a PCO 4000 CCD camera, with effective pixel size of 1.1 μm. An example of the intensity pattern produced by the mask at the detector in shown

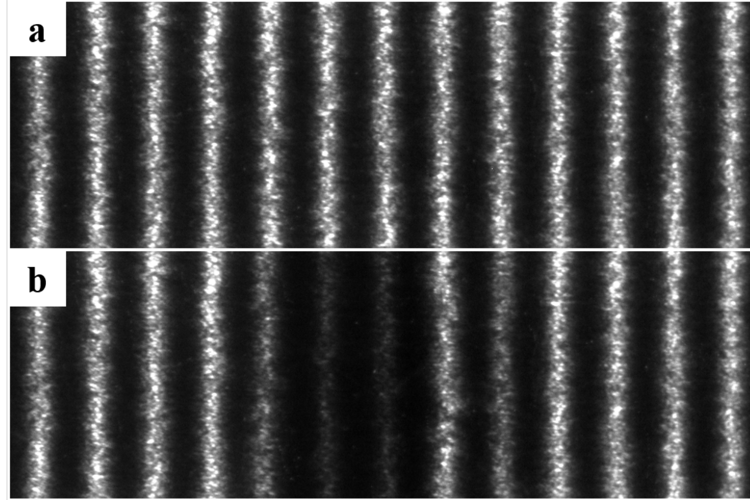

Figure 6.3: Intensity pattern produced by the absorbing mask and acquired by the high resolution detector without (a) and with (b) a sample present in the beam. The period of the intensity pattern is equal to 85 μm.

in Fig. 6.3. Projections were acquired in the angular range [0° 180°], as required by the FBP operator (see Eq. 6.4), with 3 s exposure time per projection. For each angular position, 10 dithering steps were performed. This results in an effective sampling step of 8.5 μm along the x axis. Data were re-binned by a factor of 8 in the y direction in order to obtain an effective sampling step of 8.8 μm along this axis. Three dimensional reconstructions of the parameters of interest were performed through a numerical implementation of the FBP operator, resulting in a final voxel size of 8.5×8.8×8.5 μm^3 in x, y and z, respectively.

We first tested the quantitativeness of the method on a sample made of three cylindrical test objects of different, but known, materials: polyetheretherketone (PEEK), aluminium and sapphire. For this sample, 181 projections were acquired with 1° step, and the distance between the detector and the sample was 18.5 cm. The value of absorption, refraction and scattering were extracted from a multi-gaussian interpolation of each beam created by the absorbing mask. To reduce

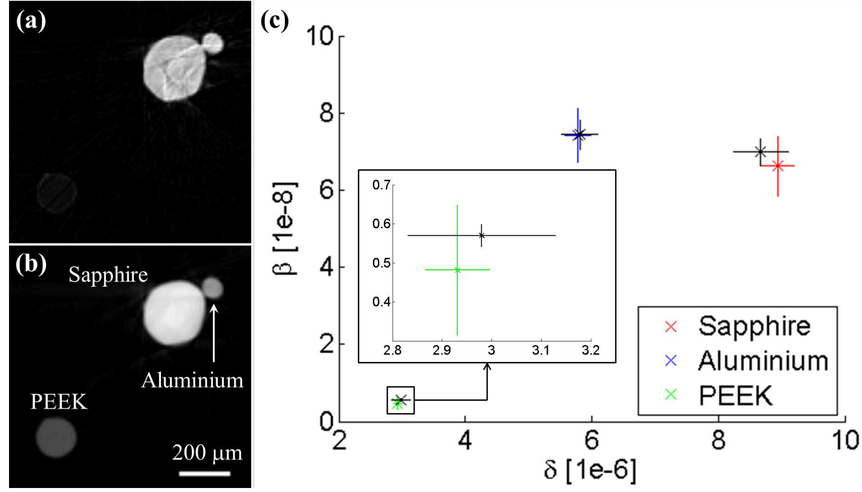

Figure 6.4: Reconstructed slices of (a) β and (b) δ from a test object made of three wires of different materials. In (c) the mean values calculated in the central region of each wire are compared with the theoretical ones (black). The error bars for the experimental data are equal to ± 1 standard deviation, while an error of $\pm 5\%$ is assumed on the theoretical values to account for potential impurities and density variations. Resolution is reduced by approximately a factor of 2 compared to the intrinsic resolution of the system (≈ 10 μm, equal to a mask aperture), due to the Gaussian filter applied to each projection to reduce noise in the final reconstruction (see text).

high-frequency noise in the reconstructed slices, a Gaussian filter was applied to the retrieved signals. The standard deviation of the Gaussian filter, chosen in relation to the noise level in the retrieved projection, is equivalent to 8.5 μm. Results of the retrieval procedure and CT reconstruction are shown in Fig. 6.4. Figures 6.4 (a) and (b) show a reconstructed slice of β and δ, respectively. Figure 6.4 (c) shows a quantitative comparison between the retrieved values in the central region of each wire, and the theoretical ones. A good agreement is found for all materials, proving that the parameters extracted from the three dimensional reconstructions are quantitatively reliable.

The second sample we imaged was a piece of wood, which contains a complex internal structure arranged on different length scales. This sample was chosen

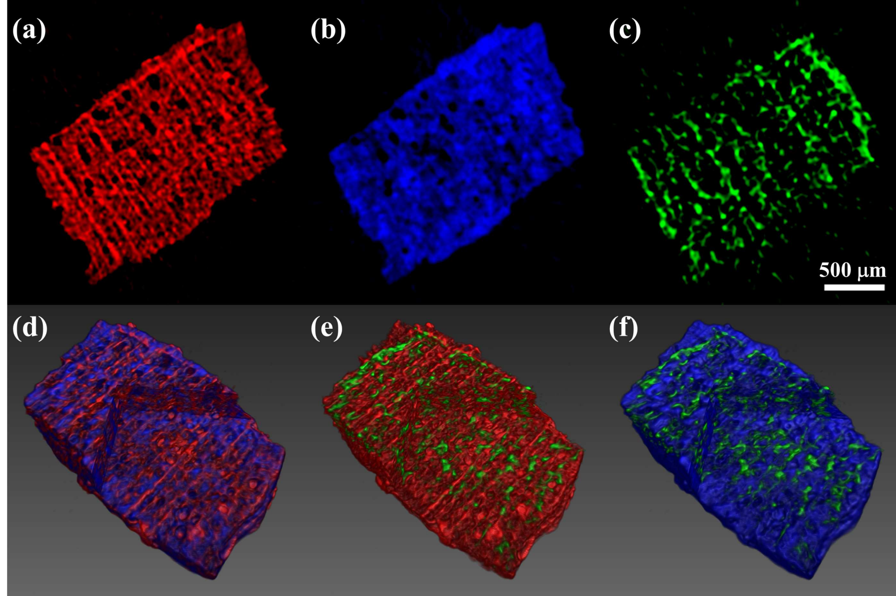

Figure 6.5: Reconstructed slices of β (a), δ (b), and σ_s^2 (c) from a wood sample, and volume renderings of β and δ (d), β and σ_s^2 (e), δ and σ_ϕ^2 (f). The volume renderings has been sectioned to show three inner planes of the sample. Resolution is reduced by approximately a factor of 3 for (a) and (b), and 4 for (c), compared to the intrinsic resolution of the system ($\approx$10 μm, equal to a mask aperture), due to the Gaussian filter applied to each projection to reduce noise in the final reconstruction (see text).

because its sub-micrometric structures are expected to show a strong scattering signal, which might significantly distort the incoming beamlets. In this situation other methods [51, 54], based on the tracking of a speckle pattern, might present problems. The distortions induced by the sample on the reference pattern might, in fact, be so severe as to make it impossible to track the original speckle effectively. The advantage of our method, in this case, is to create a known, periodic reference pattern through a non-interferometric technique, whose variations can be tracked even for high values of the refraction and scattering signals. In this case 361 projections were acquired with 0.5° step, with sample-to-detector distance of 17.5 cm. The standard deviation of the Gaussian filter for this sample is

equivalent to 12.75 μm for the absorption and refraction signals, and 17 μm for the scattering signal. Figures 6.5 (a), (b) and (c) show reconstructed slices of β, δ and σ_s^2, respectively, displayed with different colors. As expected, absorption and phase present similar features, as both these signals are ultimately related to the electron density of the sample. However, the contrast between different parts of the sample is locally different, and can be used to better identify regions of different composition within the sample. The scattering signal is not uniformly distributed within the sample. This signal, in fact, originates only from regions in which the refractive index is inhomogeneous on a scale smaller than the mask aperture. To better display the fact that these three channels provide complementary information about the sample, three volume renderings are shown in Figs. 6.5 (d), (e) and (f), where absorption, phase and scattering are superimposed in pairs.

6.4 Discussion

The obtained results show how the beam tracking approach can be used to perform quantitative x-ray phase-contrast and ultra-small-angle scattering computed tomography. The method presents the advantages of a simple experimental setup, with only one optical element placed before the sample, and that absorption, refraction and scattering can be extracted from a single exposure of the sample, without the need to scan or even displace the optical element. A scan of the sample, instead, is needed to increase the final resolution and avoid possible aliasing artefacts. As has been demonstrated in the previous chapter, the presented method does not rely on spatial and/or temporal coherence to generate

contrast, suggesting the possibility of a future CT implementation with laboratory sources [55]. Attention, however, should be paid to possible beam-hardening artefacts that might arise when the tomographic implementation is performed with polychromatic radiation. In this case, in fact, the retrieved signals are weighted averages over the energy spectrum of the corresponding monochromatic ones, and they can no longer be expressed as line integrals along the photon paths of fundamental properties of the sample.

The quantitative accuracy of the method was experimentally tested on a sample consisting of three different objects of known composition and size, and a good agreement was found between the retrieved and the theoretical value of the sample refractive index. Finally, a CT reconstruction from a complex sample was presented, showing the robustness of the method against highly scattering materials, and that the three different signals can highlight different properties of the sample.

For this proof-of-concept experiment, each beam was tracked with a relatively large number of pixels, through a Gaussian fit. Future developments will involve using masks with smaller apertures and periods; this will result in a higher final resolution of the reconstructed images, and higher sensitivity to refraction and scattering signals. The assumption of a Gaussian profile was sufficiently accurate for the present experimental conditions, as the quantitative agreement in Fig. 6.4 (c) demonstrates; however, this might not always be true in the general case. The use of more refined fitting functions and of alternative retrieval method (e.g. through direct deconvolution of the beam profiles) will be investigated in future developments.

7

One-dimensional ptychography

The beam tracking approach, as presented in chapter 4, consists in creating a small laminar beam through an absorbing slit and using a high resolution detector to track its variations, induced by a sample. To be able to extract quantitative information about the sample a model that describes its interaction with the beam is needed. In beam tracking the same model used in edge illumination and other phase contrast imaging techniques is employed, which describes the sample in terms of absorption, refraction and ultra-small-angle scattering. In this model it is assumed that absorption and refraction are constant within the slit aperture. However, it should be noted that the scattering signal comes from a violation of this assumption, and it describes variations of the complex refractive index on a scale smaller than the aperture. In this chapter we will present an alternative method, that aims at retrieving the complex transmission function of the sample at a resolution higher than the aperture size, which is the resolution limit in beam tracking. This is possible by formulating the problem within the theory of coherent diffraction imaging. After a description of this new approach, results

based on simulations and experiments are presented and discussed. These results are based on the work presented in [68].

7.1 Preliminary considerations

In the field of coherent diffraction imaging, the term *phase retrieval* indicates all those techniques aimed at reconstructing the phase of a complex electromagnetic wave impinging on a detector from the measured intensity [33, 34]. Once the phase has been retrieved, it is possible to back propagate the wave to the sample plane to obtain the complex transmission function of the sample, which describes the absorption and the phase shift it introduced on the x-ray beam. Coherent diffraction algorithms allow the retrieval of the phase from a single diffraction pattern, provided that some conditions are met: namely, the sample [33, 69] or the illuminating beam [70] must be isolated and small enough to avoid the so called *undersampling* problem at the detector plane. Moreover, some degree of *a priori* knowledge must normally be available, such as, for example, the support of the isolated sample or beam. These limitations can be overcome in ptychography by acquiring several diffraction patterns of different and partially overlapping regions of the sample. This is achieved by scanning a small pencil beam, called probe, through the sample and measuring the corresponding diffraction pattern. All collected patterns are then combined by means of a suitable reconstruction algorithm [35, 36], from which the complex transmission function of the area of the sample scanned by the probe, and the probe itself are retrieved. The degree of overlapping between the different regions of the sample is a key factor in ptychography. The lack of information coming from measuring only the amplitude

of the diffracted field, and not its phase, is overcome by the fact that a certain region of the sample contributes to more than one diffraction pattern. This creates a "redundancy" of information that enables the solution of the phase problem. The main advantage of ptychography is that it enables imaging extended objects at high resolution without requiring any *a priori* information on the sample or the probe.

Ptychography is normally implemented in the *far-field* regime, i.e. when the propagation distance is large enough as to enable the diffracted field at the detector plane to be expressed as the Fourier transform of the field at the sample plane. This configuration allows the achievement of very high and virtually noise-limited resolution. More recently, an extension to the near-field regime has been proposed [71], in which the resolution is limited by the (demagnified) pixel size. While in the far-field case a small, pencil beam, created through one or more optical elements (lenses, mirrors, pinholes) is used to illuminate the sample, in the near-field one the beam is not limited, and the sample is completely illuminated. In the beam tracking setup, described in chapter 4, a small, laminar beam is created by means of an absorbing slit. This beam is strongly asymmetric: the sample is completely illuminated along one direction, while only a small portion of it is covered along the orthogonal one. The sample is then scanned through the beam, and several intensity pattern are recorded. If the scanning step is small enough, the overlap between the regions illuminated by the beam in two successive acquisitions can enable the adopting of a ptychographic approach to retrieve the complex transmission function of the sample. Due to the asymmetric shape of the beam, this configuration requires a "mixed" approach that combines far-field and near-field ptychography. Since the sample is completely illuminated

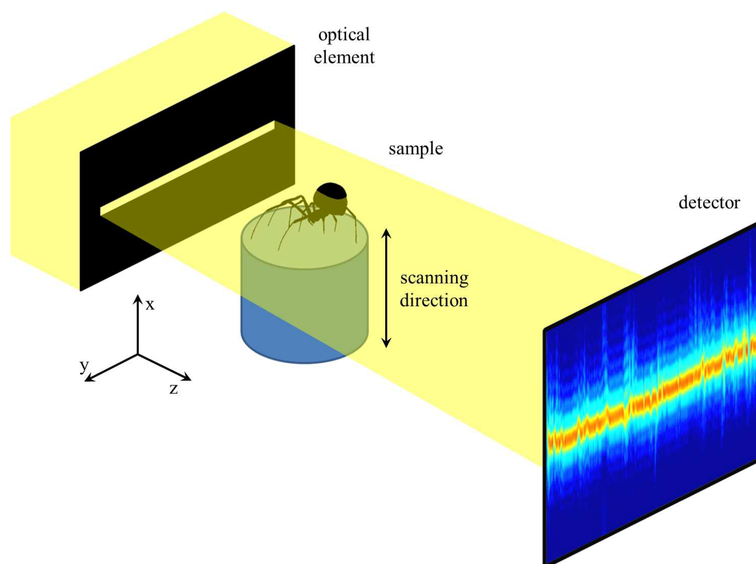

Figure 7.1: Schematic diagram of 1D-PIE methods.

in the horizontal direction, in fact, only a one-dimensional scan is required; at the same time, noise-limited resolution can be achieved only in the scan direction. In the following, we will refer to this approach as "1D-PIE" (one dimensional ptychographic iterative engine).

7.2 Reconstruction algorithm

Figure 7.1 shows a schematic representation of a typical experimental setup for 1D-PIE. An x-ray beam, asymmetrically shaped by one or more optical elements, passes through the sample and propagates to the detector, where its intensity is recorded. Let $O(x, y)$ and $B(x, y)$ be the sample complex transmission function and the complex amplitude of the probe impinging on the sample, respectively. For a particular position in the scan, the wave exiting from the sample can be

expressed as:

$$\psi_j(x,y) = O(x,y)B(x - x_j, y - y_j), \tag{7.1}$$

where (x_j, y_j) is the relative position between the beam and the sample. After propagation in free space over a distance D, the wave on the detector plane will become:

$$\Psi(x,y) = \mathcal{P}_{xy}\left[\psi_j\right](x,y) = \psi_j(x,y) * H_D(x,y), \tag{7.2}$$

where $\mathcal{P}_{xy}$ is the operator describing the propagation, $*$ denotes two-dimensional convolution, and H_D is the Fresnel propagator:

$$H_D(x,y) = \frac{\exp\left(ikD\right)}{i\lambda D} \exp\left(ik\frac{x^2+y^2}{2D}\right), \tag{7.3}$$

where λ is the x-ray wavelength and $k = 2\pi/\lambda$. Neglecting the constant factor, Eq. (7.3) can be factorized in the product of two one dimensional functions:

$$H_D(x,y) \propto \exp\left(ik\frac{x^2}{2D}\right) \exp\left(ik\frac{y^2}{2D}\right) = h_D(x)h_D(y). \tag{7.4}$$

This allows us to rewrite Eq. (7.2) in the form:

$$\Psi(x,y) = \mathcal{P}_x\left[\mathcal{P}_y\left[\psi_j\right]\right](x,y), \tag{7.5}$$

where, if f is a generic function of two variables:

$$\mathcal{P}_x\left[f\right](x,y) = \int f(r,y)h_D(x-r)dr, \tag{7.6}$$

with an analogous definition for $\mathcal{P}_y$. The integral in Eq. (7.6) can be written in various mathematically equivalent forms, but since we will eventually have to deal with a discrete data matrix (as acquired by the detector pixels), it is important to choose one that enables avoiding numerical problems (such as for example undersampling). In particular, along the lines discussed in reference [72], we choose the following, different expressions for $\mathcal{P}_x$ and $\mathcal{P}_y$:

$$\mathcal{P}_x\left[f\right](x,y) = h_D(x)\mathcal{F}_r\left[f(r,y)h_D(r)\right]\left(\frac{x}{\lambda D}\right), \tag{7.7}$$

$$\mathcal{P}_y\left[f\right](x,y) = \mathcal{F}_\eta^{-1}\left[\mathcal{F}_s\left[f(x,s)\right](\eta)\hat{h}_D(\eta)\right](y), \tag{7.8}$$

where $\mathcal{F}_i$ and $\mathcal{F}_i^{-1}$ indicate the one dimensional Fourier and inverse Fourier transforms with respect to the i coordinate, respectively, and $\hat{h}_D$ is the Fourier transform of h_D. The distinction between the description of the propagation effects in the x and y directions arises from the extremely asymmetric shape of the x-ray probe. In the scanning direction (x), the beam is very narrow, resulting in a small field of view ($\approx$10 μm) that enables preventing sampling problems on the detector plane when Eq. (7.7) is implemented numerically. In the y direction, instead, the field of view is much larger ($\approx$1 mm), and a different numerical implementation is needed. Referring to the Fresnel number $N_F = W^2/(\lambda D)$, where W is the lateral extent of the illumination [71], we found that, in the experimental conditions described in the following, $N_F \approx 1$ in the x direction, and $N_F \approx 10^4$ in the y direction. Equation (7.7) is actually a generalization to the Fresnel regime ($N_F \approx 1$) of the well-known equation $\mathcal{P}\left[f\right] = \mathcal{F}\left[f\right](x/(\lambda D))$ used to describe x-ray diffraction; indeed, in the far field condition $h_D(r) \approx 1$ and the propagated field is proportional to the Fourier transform of the initial field. Equation (7.8),

instead, uses the "angular spectrum propagation" method, which solves the convolution product in Eq. (7.2) in the Fourier space by means of the convolution theorem, and is numerically well-behaved in the near field regime ($N_F \gg 1$).

The 1D-PIE uses a modified version of the ePIE algorithm [36], with the key difference lying in the description of the forward propagation through Eqs. (7.5), (7.7) and (7.8). The ePIE algorithm can be summarized with the following scheme:

```
Start n cycle
  - Sample and probe functions initialization:
    O^(n)(x,y) = O^(n-1)(x,y);
    B^(n)(x,y) = B^(n-1)(x,y);
  Start j cycle
    - Wave function after the sample:
      ψ_j^(n)(x,y) = O^(n)(x,y) B^(n)(x - x_j, y - y_j);
    - Forward propagation:
      Ψ_j^(n)(x,y) = P_xy[ψ_j^(n)](x,y);
    - Modulus constrain:
      Ψ̄_j^(n)(x,y) = sqrt(I_j(x,y)) Ψ_j^(n)(x,y)/|Ψ_j^(n)(x,y)|;
    - Backward propagation:
      ψ̄_j^(n)(x,y) = P_xy^(-1)[Ψ̄_j^(n)](x,y);
    - Sample and probe function update:
      Ō^(n)(x,y) = O^(n)(x,y) + α[ψ̄_j^(n)(x,y) - ψ_j^(n)(x,y)] B_N^(n)(x - x_j, y - y_j);
      O^(n)(x,y) = Ō^(n)(x,y);
      B̄^(n)(x,y) = B^(n)(x,y) + β[ψ̄_j^(n)(x,y) - ψ_j^(n)(x,y)] O_N^(n)(x + x_j, y + y_j);
```

$B^{(n)}(x, y) = \bar{B}^{(n)}(x, y)$;

```
  End j cycle
End n cycle
```

The algorithm iteratively reconstruct the sample and probe functions $O(x, y)$ and $B(x, y)$. Starting guesses $O^{(0)}(x, y)$ and $B^{(0)}(x, y)$ are required for both these functions. The algorithm consists of a main loop (n cycle), which is usually stopped when the variation between two consecutive reconstructions of the sample is smaller that a certain threshold or after a certain number of iterations, and a sub-loop (j cycle), in which the index j runs over all the relative positions between the sample and the probe. At every step of the main cycle, the guesses $O^{(n)}(x, y)$ and $B^{(n)}(x, y)$ are updated from the previous iteration. Then, for each j value, the wave after the sample $\psi_j^{(n)}(x, y)$ is calculated and propagated at the detector plane to obtain $\Psi_j^{(n)}(x, y)$. The so called *modulus constrain* is applied: the amplitude of $\Psi_j^{(n)}(x, y)$ is set equal to the square root of the measured intensity $I_j(x, y)$. The new wave function $\bar{\Psi}_j^{(n)}(x, y)$ is back-propagated at the sample plane to obtain $\bar{\psi}_j^{(n)}(x, y)$. The back-propagation operator $\mathcal{P}_{xy}^{-1}$ is obtained by substituting $D \rightarrow -D$ in the expression of $\mathcal{P}_{xy}$. The cycle is concluded by updating the sample and probe functions with the formulas displayed above, where $B_N^{(n)}(x, y) = \text{conj}\left[B^{(n)}(x, y)\right] / \max\left[|B_N^{(n)}(x, y)|^2\right]$, $O_N^{(n)}(x, y) = \text{conj}\left[O^{(n)}(x, y)\right] / \max\left[|O_N^{(n)}(x, y)|^2\right]$, conj indicates the complex conjugate operation, and max takes the maximum value of the considered function. α and β are arbitrary constant that can be adjusted to alter the step-size of the update; their value is usually set to 1. Additionally, at each n iteration, the intensity of the propagated reconstructed beam can be set equal to a flat field im-

age (i.e. an intensity pattern acquired without the sample). This last feature can help decoupling the contribution of the probe and the sample to the diffraction pattern, and it also avoids possible twin solutions consisting, for example, of the sum of two opposite phase gradients in the sample and beam complex functions.

7.3 Simulations

The simulated system presents the same features as the experimental setup described in the following section: x-ray energy of 9.7 keV, sample to detector distance of 58 cm and detector pixel size of 0.8 μm. Figures 7.2 (a) and (b) show the sample amplitude and phase maps used in the simulations, with amplitude and phase values lying in the intervals [0.6, 1] and [-1, 0] rad, respectively. Figures 7.2 (c) and (d) show, instead, the amplitudes and the phases of the simulated probe, respectively. While the phase is constant, the amplitude assumes the shape distribution that would be caused by an inhomogeneous horizontal slit, i.e. a degree of inhomogeneity in the beam is created through a random variation, along the horizontal direction, of the vertical size and central position of the slit in the intervals 15$\pm$5 μm and 1.25$\pm$1.25 μm, respectively. This was introduced to enable a closer representation of the actual experimental conditions, where an imperfect slit was used. 136 scans were simulated with a 2.3 μm scanning step, resulting in an overlap between two subsequent probe positions of about 80%. It is important to note that there is no theoretical limitation for the horizontal extension of the beam, the only drawback being the increased computational time required to run the corresponding simulation. The presence of noise is included in the simulation in the following way: a constant offset of about 1/50 of the maximum recorded

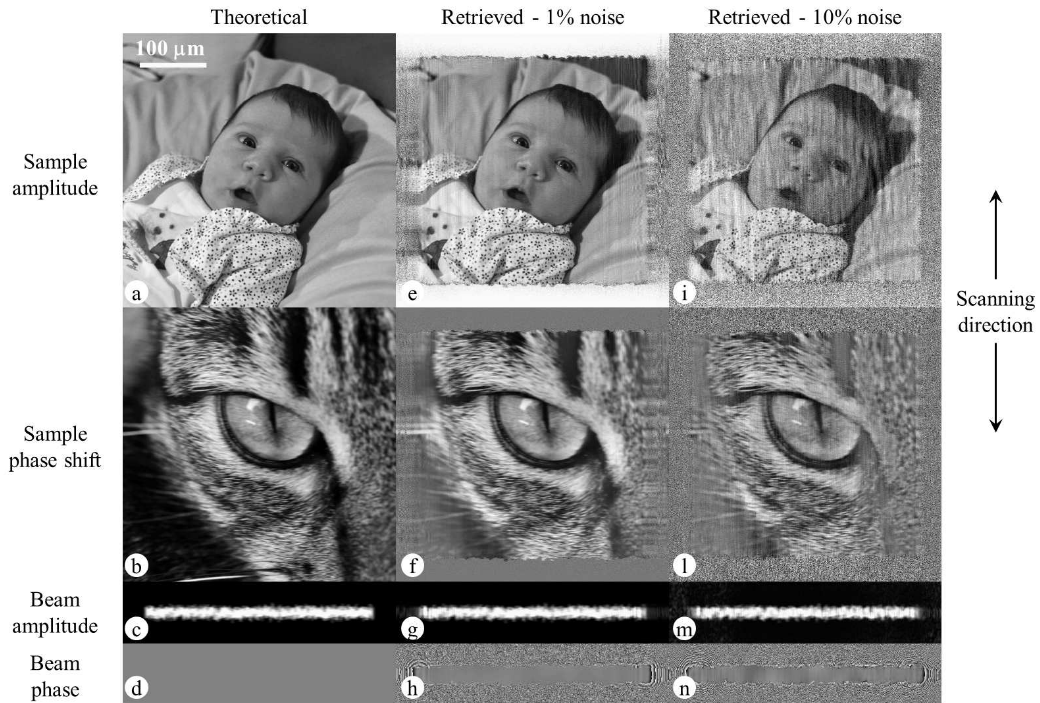

Figure 7.2: Simulated sample amplitude (a) and phase shift (b) maps. Simulated beam amplitude (c) and phase (d) maps. Retrieved sample (e, f) and beam (g, h) in the case of 1% Gaussian noise. Retrieved sample (i, l) and beam (m, n) in the case of 10% Gaussian noise. All the original photographs used to simulate the sample amplitude and phase shift maps were taken by the author.

intensity value, simulating the detector dark signal (i.e. the signal recorded when the source is off), is added to the theoretical diffraction patterns, and a 1-10% Gaussian noise is then generated. On top of this, the constant offset (which in the real case is measured experimentally) is then subtracted, and the negative intensity values are set to 0. The chosen offset and noise levels resemble the ones obtained in experimental data.

Figures 7.2 (e)-(n) show the results of the 1D-PIE reconstruction algorithm in the presence of 1% (Figs. 7.2 (e)-(h)) and 10% (Figs. 7.2 (i)-(n)) Gaussian noise, respectively. In both cases, the algorithm converges to the right solution, despite

the use of a wide laminar beam and scanning being performed in one direction only. The latter case, in particular, demonstrates the substantial robustness of the method against increasing noise levels, although these will inevitably lead to noisier reconstructed images. We found that introducing a degree of inhomogeneity in the probe is of primary importance for this method. Previous findings indicate that a "structured" illumination can improve the overall performance of ptychographic algorithms [73], and that this structuring of the probe becomes even more important when ptychography is applied in the near field regime [71], as in this case the illumination extends over most of the reconstructed field of view and its structure becomes the only source of diversity in the dataset. An additional advantage for the 1D-PIE brought by structuring the beam is that it helps coupling the effects of propagation in the vertical and horizontal directions, so that a strong degree of diversity is introduced in the diffraction pattern also in the horizontal direction by the vertical scan procedure.

We monitored the convergence of the algorithm [36] using the normalized root mean square error ϵ_n between the reconstructed and real sample transfer functions:

$$\epsilon_n = \frac{\sum_{x,y} |O(x,y) - O^{(n)}(x,y)|^2}{\sum_{x,y} |O(x,y)|^2}. \tag{7.9}$$

Figure 7.3 shows the evolution of ϵ_n over 1000 iterations of the algorithm for the two simulations previously described. The error continuously decreases with the number of iterations in both cases, reaching smaller values for lower noise level, as expected.

A closer analysis of the reconstructed images of the sample shows the presence of some artefacts. In particular, structured noise, in the form of vertical stripes, is

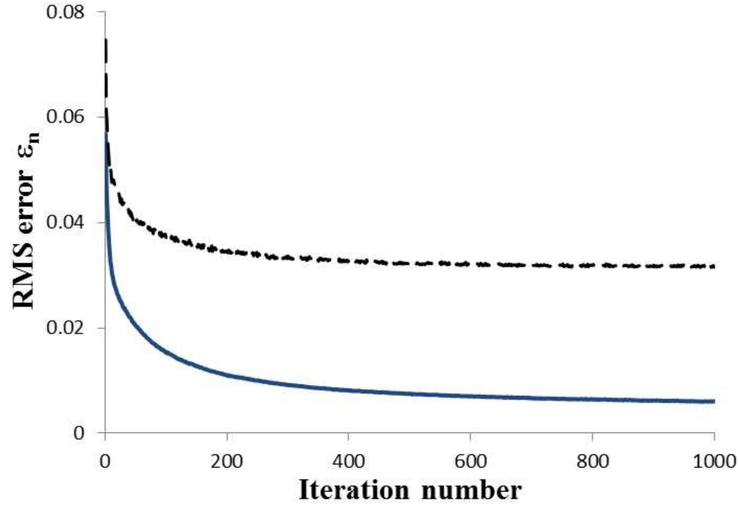

Figure 7.3: Evolution of the RMS error ϵ_n. The solid (blue) line refers to the case of 1% noise, the dashed (black) line refers to the case of 10% noise.

visible, especially in the amplitude image in the 10% noise case (Fig. 7.2(i)), and the value of the phase shift is not fully retrieved in the dark, bottom left part of the image (Fig. 7.2(f) and (l)). Similar considerations apply to the experimental images presented in the next section. In particular, structured noise can be seen both in Fig. 7.5, near the boundaries of the sample, and in Fig. 7.8 along the entire image. These problems will be discussed later in this chapter.

7.4 Experiments

Experimental data were acquired at the coherence branch of I13 at the Diamond Light Source (Didcot, UK). The source size of about 400×13 μm^2 (horizontal and vertical FWHM, respectively), jointly with the large source to sample distance of about 210 m, provide a high degree of coherence at the sample plane [48]. An x–ray energy of 9.7 keV was selected for the experiment using a Si(111) crystal

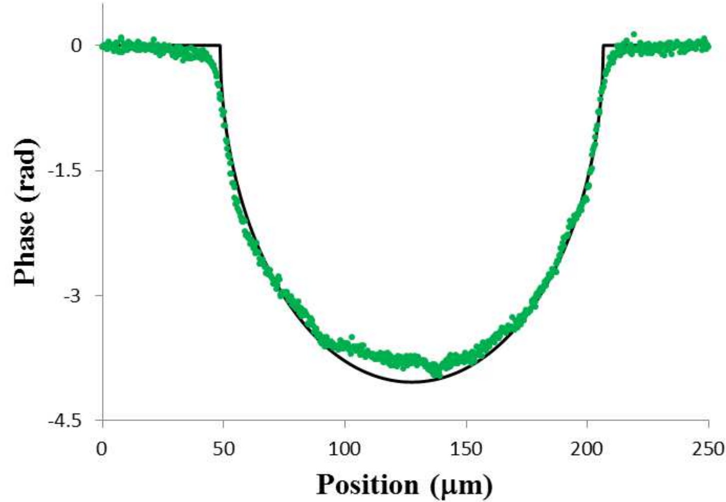

Figure 7.4: Reconstructed (dotted, green) and theoretical (solid, black) phase shift of a PEEK monofilament in water.

monochromator. For the first experiment, a 10 μm slit was used to define the beam in the vertical direction. The sample and the detector were placed 6.3 cm and 64.3 cm downstream of the slit, respectively. A scintillation microscope was used as detector, consisting of a scintillation screen, an 8× magnifying optics and a PCO Edge sCMOS camera with 2560×2160 (horizontal and vertical, respectively) pixels. The effective pixel size was 0.8 μm.

Our first experimental aim was to demonstrate that the proposed method is capable of retrieving phase values which are quantitatively correct. For this, we used a weakly perturbing sample consisting of a polyetheretherketone (PEEK) monofilament of 160 μm diameter immersed in 0.5 cm of water. Figure 7.4 shows the comparison between theoretical and experimentally retrieved phase shifts; a good quantitative agreement is obtained. Note that the corresponding sample absorption signal is practically negligible at this energy ($\approx$0.02%). For this sample, 500 scans were performed with scanning step of 1 μm and 2 s exposure time

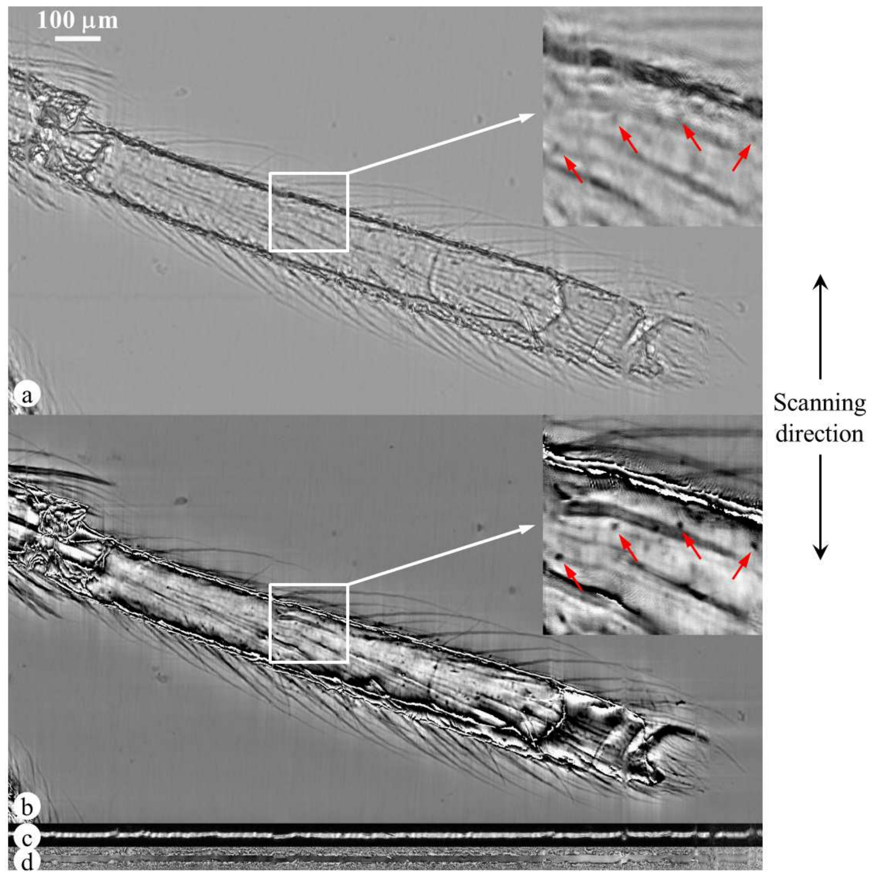

Figure 7.5: Reconstructed results of a spider leg. Retrieved sample amplitude (a) and phase shift (b) maps. Retrieved beam amplitude (c) and phase (d) maps. The lateral inserts show an enlargement of the regions in the white squares; red arrows show some small details (≈5μm) visible in the reconstructed images, and how these appear sharper in the phase image.

for each scan, for a total exposure time of about 17 minutes.

We then tested the method on a more complex biological sample, i.e. the leg of a tiny spider; the reconstructed amplitude and phase maps are shown in Fig. 7.5. In this case, since the real sample transfer function O is unknown, the error between the measured and reconstructed intensities on the detector plane was

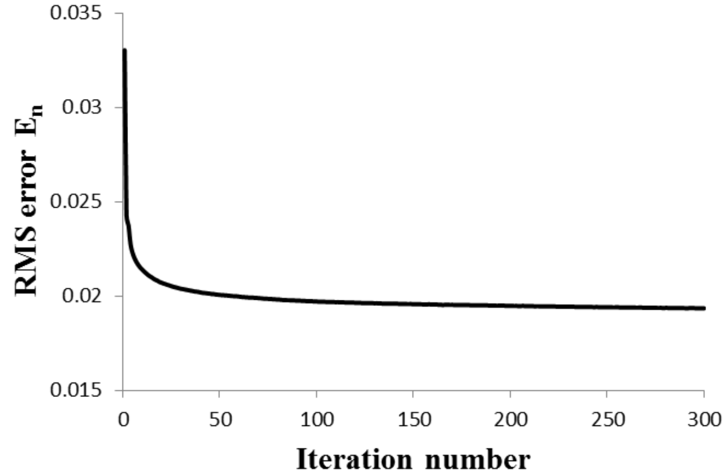

Figure 7.6: Evolution of the RMS error E_n.

computed as:

$$E_n = \frac{\sum_j \sum_{x,y} |\sqrt{I_j(x,y)} - |\Psi_j(x,y)||^2}{\sum_j \sum_{x,y} I_j(x,y)}. \tag{7.10}$$

Figure 7.6 shows E_n as a function of the iteration number. The results resemble those obtained in the simulations: the error continuously decreases, leading to a high final image quality. The phase image, in particular, presents a high level of detail, and very small features of the spider leg are resolved, as highlighted in the lateral insert in Fig. 7.5. For this sample, 688 scans were performed with scanning step of 1.6 μm and 0.5 s exposure time for each scan, for a total exposure time of about 6 minutes.

For this first proof-of-concept experiment, the structuring of the probe was implemented by using the slit imperfections on top of the beam inhomogeneities caused by imperfect optical transfer through the beamline. From simulations, an increase in robustness and image quality, together with a reduction of artefacts, can be predicted when a stronger degree of perturbation is introduced in the probe. The photon statistics was also limited in this case, resulting in relatively

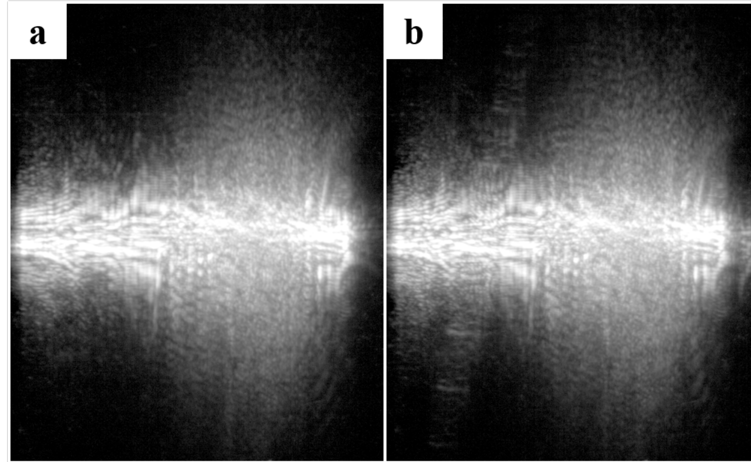

Figure 7.7: Logarithm of the intensity pattern recorded by the detector using a thin wood section to increase the beam inhomogeneity without (a) and with (b) a sample present in the beam.

high levels of noise (≈5-10%).

Following the above considerations, a second experiment was performed with a different experimental configuration, aimed at experimentally measuring the resolution of this method. In this case, a beam of approximately 20 μm in the vertical direction was defined through an absorbing slit. A compound refractive lens, placed close to the x-ray source, was used to increase the total flux in the slit aperture. To increase the beam inhomogeneity, a thin wood section was placed close to the slit, before the sample. The sample to detector distance was 94 cm. A scintillation microscope was used as detector, consisting of a scintillation screen, an 8× magnifying optics and a PCO 4000 CCD camera with 4008×2672 (horizontal and vertical, respectively) pixels. The effective pixel size was 1.1 μm. An example of the diffraction pattern acquired in this configuration is shown in Fig. 7.7. 180 scans were performed with scanning step of 0.5 μm. To increase the diversity in the dataset, the horizontal position of the probe was regularly varied

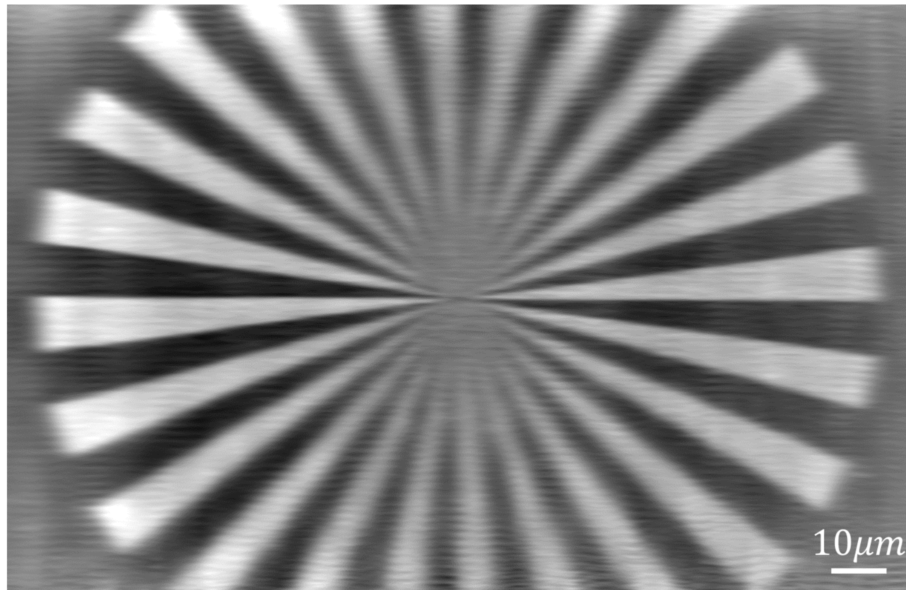

Figure 7.8: Reconstructed phase shift of the resolution star pattern.

by $[-33, 0, 55]$ μm along the scan. To reduce noise in the final data, 30 frames, each of 0.5 s exposure time, were acquired for each scan position, for a total exposure time of about 45 minutes. To correct for possible errors in the nominal position of the motor used to scan the sample across the beam, the procedure described in [74] was adopted in the reconstruction procedure. The sample was a resolution star pattern, and the result of the retrieval procedure is shown in Fig. 7.8. The asymmetry in the spatial resolution is evident in the central region of the image, where the period of the star pattern is smaller. Note that to reduce the scan and reconstruction time, only the central part of the star, from which the resolution can be measured, was illuminated and reconstructed.

7.5 Spatial resolution

The resolution achievable in 1D-PIE is different along the x (scanning) and y directions. In the x direction, it is limited by the maximum scattering angle for which diffraction data are collected above the noise level, as for any other CDI technique. In the y direction, where a near-field approach is used, the resolution is limited by the (demagnified) pixel size. Different approaches can be used to measure, or at least estimate, the resolution of the reconstructed images. In particular, for the simulated case, we compared the Fourier transforms of the simulated sample transfer function with the reconstructed one for both the 1% and the 10% noise cases, using the Fourier ring correlation (FRC) criterion [75]. To distinguish between the x and y directions, we selected two angular regions of the Fourier space along the x and y directions (Fig. 7.9(a)). The FRC was then computed in the first region (upper and lower parts of the Fourier space) to estimate the resolution in the x direction, and in the second region (left and right-hand parts) for the resolution in the y direction. We arbitrarily chose an angular width of 30° for the two regions: a larger angle would include a greater part of the Fourier spectrum, in which, however, the contribution of the x and y directions would be largely mixed. The maximum frequency for which the sample is reconstructed correctly was found using the 2σ criterion [75] (Fig. 7.9), and the results are shown in Table 7.1. This result shows that the 1D-PIE has the potential to offer an enhanced resolution, and therefore increased sensitivity to small details, in the x direction.

A similar approach could be used to estimate the resolution of the experimental data, when two independent reconstructions are available. For the ex-

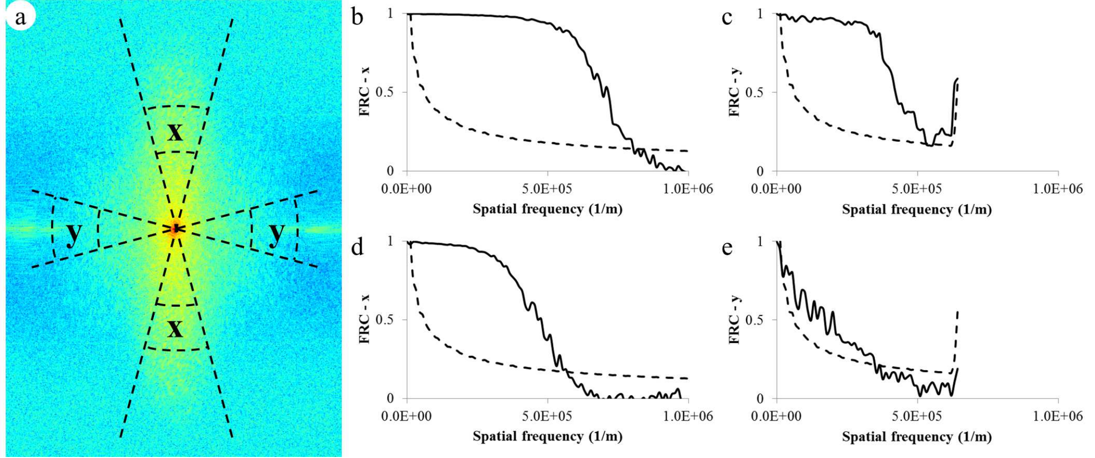

Figure 7.9: (a) Division of the Fourier space for the calculation of the FRC curves. FRC curves (solid) and 2σ criterion (dashed) for 1% noise along x (b) and y (c), and for 10% noise along x (d) and y (e).

Table 7.1: Estimated resolution values of the reconstructed sample transmission function for the simulated case, using the FRC and the 2σ criterion.

Noise	Resolution x (μm)	Resolution y (μm)	Detector pixel (μm)
1%	0.6	0.9	0.8
10%	0.9	1.4	0.8

perimental results shown in Fig. 7.5, however, only one dataset, and thus one reconstruction, was available. Nonetheless, a first estimation of the experimental resolution can be obtained by analysing the Fourier spectrum of the spider leg transmission function, and its noise level, in the same x and y regions indicated in Fig. 7.9(a). In the high frequency parts of the spectrum, in fact, noise dominates: we can therefore use these parts of the spectrum to estimate the mean noise value $\bar{n}$ and its standard deviation σ_n in the x and y regions of the spectrum. Assuming that all the frequency components above $\bar{n} + \sigma_n$ are correctly reconstructed, we can estimate the resolution along the x and y directions to be

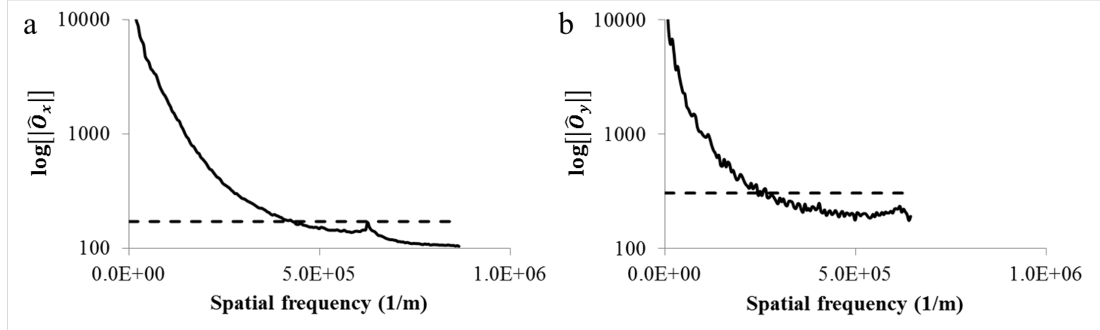

Figure 7.10: Mean radial Fourier spectrum of the spider leg transmission function (Fig. 7.5) along the x (a) and y (b) directions (solid lines) and relative thresholds (dashed lines) used to estimate the experimental resolution.

approximately 1.2 μm and 2.0 μm, respectively. This is done by comparing the radial integrations of the Fourier spectrum (Fig. 7.10, solid lines) in the x and y regions with the relative thresholds (Fig. 7.10, dashed lines) $\bar{n} + \sigma_n$, calculated in the same regions. Note that the values of σ_n are calculated from the two-dimensional Fourier spectrum, and thus they appear to be higher that the noise levels of the one-dimensional Fourier profiles in Fig. 7.10; this, however, only depends on the radial integration process that reduces the noise level of the resulting one-dimensional profiles. Note also that the thresholds for the two regions are different, since the noise level is higher in the y region than in the x region. Using a more conservative threshold of $\bar{n} + 2\sigma_n$, we obtain a resolution of 1.5 μm and 2.6 μm for the x and y direction, respectively.

The resolution obtained for the star pattern in Fig. 7.8, instead, can be directly measured from the reconstructed image. In particular, the phase modulation in the reconstructed image was measured as a function of the period of the star pattern (proportional to the distance from the centre of the star), along the horizontal and the vertical directions. The result is shown in Fig. 7.11. When the

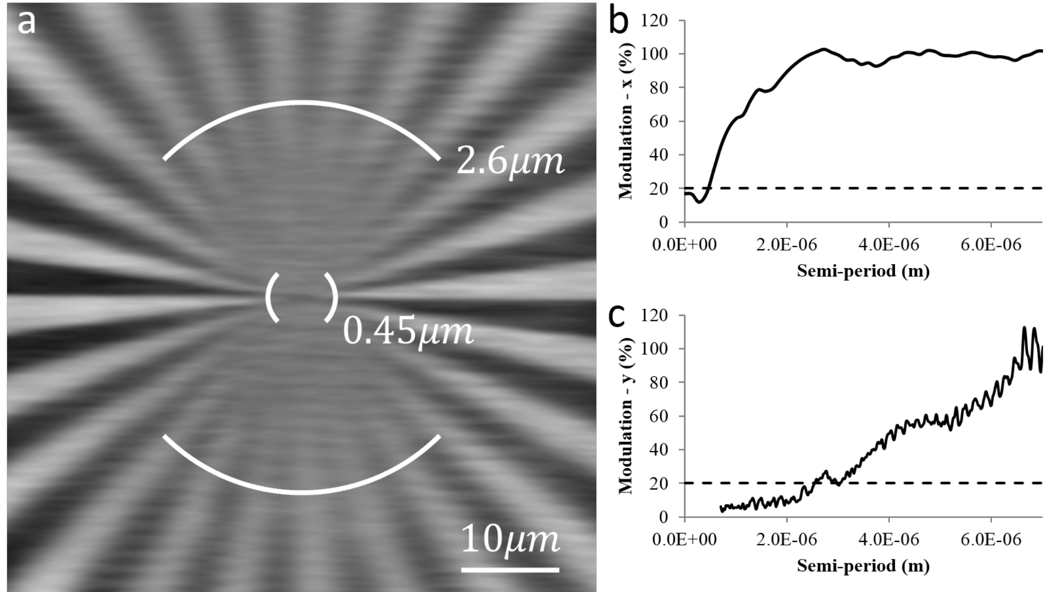

Figure 7.11: (a) Central region of the reconstructed image. Circles corresponding to a semi-period of the star pattern of 0.45 μm and 2.6 μm are shown, representing the final resolution in the x and y direction, respectively. Profiles of the phase modulation in the final reconstruction along the x (b) and y (c) directions (solid lines) and relative thresholds (dashed lines), used to estimate the experimental resolution, as a function of the semi-period of the star pattern.

period is much greater than the resolution, the modulation is maximum (100%); as the period decreases, the modulation approaches 0%. By using a threshold equal to 20%, a value of 0.45 μm and 2.6 μm for the resolution in the vertical and horizontal direction was found, respectively. Note that we define here the resolution equal to the semi-period of the pattern for which the modulation is equal to the chosen threshold (20%). The results obtained for the experimental resolution are summarized in Table 7.2. It is important to note how, by increasing the photon statistic and the probe inhomogeneity, a substantial improvement in the resolution in the vertical direction is observed in comparison with the results obtained for the spider leg. The same improvement is not found for the resolu-

Table 7.2: Estimated resolution values of the reconstructed sample transmission function for the experimental case.

Sample	Resolution x (μm)	Resolution y (μm)	Detector pixel (μm)
Spider leg	1.2	2.0	0.8
Star pattern	0.45	2.6	1.1

tion in the horizontal direction. In the two cases, in fact, the resolution in the y direction is 2.5 and 2.4 times larger than the pixel size, respectively. These values are compatible with the intrinsic resolution of the detector, which is larger than the pixel size, due to its point spread function.

7.6 Discussion

The presented results show how the 1D-PIE approach allows the reconstruction of the complex transmission function of relatively large samples, with enhanced resolution in the scanning direction. The technique has been applied to simulated data, showing excellent robustness against increasing noise levels, and to experimental data, confirming the method's ability to correctly reconstruct the quantitative values of amplitude and phase for large fields of view. A peculiar feature of the method is the intrinsic asymmetric resolution of the reconstructed images, and both simulation and experiment show that sub-pixel resolution is achievable along the scanning direction.

The images obtained through this approach, however, can present artefacts that need to be further investigated. In particular, some structured noise can appear in the reconstructed images. This can be attributed to an incorrect retrieval of the probe function. In fact, as this is scanned through the sample, an error

in the probe would induce a corresponding error in the retrieved sample transmission function, with a structure determined by the scan pattern. This problem can be seen in both simulated (Fig. 7.2(i)) and experimental (Figs. 7.5 and 7.8) results. Another limitation we observed is the slow convergence of the algorithm, as well as possible stagnations. This can result in regions of the object where the correct value of the transmission function is retrieved only after a high number of iterations, or where the value of the phase shift is not fully retrieved. This problem usually appears in uniform regions of the reconstructed images (see, for example, the background in Fig. 7.2(f) and (l)).

It is interesting to compare the 1D-PIE approach to beam tracking. In beam tracking, the resolution in the scanning direction is comparable to the aperture of the slit used to define the beam. For images of the star pattern, the resolution obtained with beam tracking would therefore be 20 μm, almost 45 fold the one obtained with 1D-PIE. Additionally, with the beam tracking approach only the gradient of the phase shift is directly reconstructed; while this signal enhances the borders of a sample structures, it provides limited "area" contrast. On the other hand 1D-PIE cannot be implemented with incoherent laboratory sources, and, in general, the convergence of the retrieval procedure is not guaranteed. If, for example, the overlap between subsequent scan positions in not sufficient, the algorithm can fail to converge. We found that this could also be the case if the distortion induced by the scattering element to the probe is too high. Further studies are therefore necessary to address the above problems, encountered in the development of the 1D-PIE method.

Conclusions

X-ray phase contrast imaging (XPCi) is an important tool in the study and characterization of specimens in different research fields. Its advantages in terms of image contrast and information content have been demonstrated in the last two decades and are currently exploited in different facilities around the world, both with synchrotron and laboratory setups. New techniques are currently being developed, aiming at increasing the performances of XPCi and gradually replacing absorption-based systems. To achieve this goal, it is of primary importance to develop techniques based on simple experimental configurations, which can be implemented with standard laboratory systems. At the same time, new synchrotron facilities are being built, and existing one updated, offering increased performances in terms of photon flux and coherence. This promotes the development of innovative imaging techniques that can achieve enhanced performance by benefiting from the above features. In this context, techniques such as edge illumination and ptychography represent an excellent example of how XPCi is exploited in laboratory and synchrotron environments. While edge illumination has demonstrated high phase sensitivity also with laboratory sources, ptychography, and more in general coherent diffraction imaging, currently allows the achievement of extremely high resolutions with coherent sources.

Based on recent achievements in the field of XPCi, two new methods have been presented in this work: beam tracking and one dimensional ptychography (1D-PIE). Beam tracking allows the quantitative reconstruction of absorption, refraction and ultra-small-angle scattering signals. In its first implementation, it relied on a high resolution detector to analyse the variations induced by a sample to a reference beam. The complementary nature of the above three signals, together with the simple experimental setup, makes beam tracking a valuable tool for multi-modal x-ray imaging of specimens in a large variety of fields. A deeper analysis of the method showed its very significant analogies with edge illumination: the role played by detector mask apertures in edge illumination is replaced by the pixel point spread function in beam tracking. This opens the possibility to implement beam tracking with laboratory setups and standard detectors, and to adopt phase retrieval methods already developed in the context of edge illumination. Removing the detector mask results in a more efficient use of the radiation dose delivered to the sample, and in a reduction of the total exposure time. On the other hand, unlike in edge illumination, the sensitivity to the refraction and scattering signal in beam tracking strongly relies on the detector performances. While this poses restrictions in terms of suitable detector technology, it leaves promising room for improvement, related to the development of improved photon-counting, direct conversion detector systems, currently a very active area of research. The last step in the development of beam tracking presented in this work is its implementation in computed tomography (CT). The first experimental demonstration of beam tracking CT was obtained using synchrotron radiation. Results demonstrate the quantitative nature of CT reconstructions obtained with this technique, its applicability to complex samples, and

suggest steps for further improvements.

The second method presented here, 1D-PIE, has been developed with the aim to maximize the amount of informations extracted from the intensity patterns recorded with a beam tracking setup. In beam tracking, the extracted parameters refer to average properties of the sample refractive index within the aperture. Conversely, 1D-PIE aims at retrieving the variations of the complex refractive index within the aperture, rather than average quantities. To achieve this result the x-ray beam, the sample, and their interaction need to be described by means of the wave theory of x-ray propagation. This allows us to relate variations of the complex refractive index of the sample within the aperture to variations in the detected intensity pattern. However, the inverse problem of reconstructing the sample refractive index from a measured intensity pattern is challenging, and several approaches to its solution have been developed over the years. Ptychography is one of them, and presents some similarities with our first implementation of beam tracking, with a single absorbing slit placed before the sample. 1D-PIE combines beam tracking and ptychography, leading to a significant improvement in terms of image resolution with respect to the former. 1D-PIE reconstructions, however, are more complex than the phase retrieval method used in beam tracking, and some problems are still open that need to be addressed. If properly developed, however, 1D-PIE could provide an important improvement of the beam tracking approach when coherent radiation and high resolution detectors are available.

It is finally important to point out some of the possible future developments of the two techniques presented here. In beam tracking, a Gaussian beam assumption has been used for all the results presented in this work. This assump-

tion, however, is merely a tool to simplify the retrieval procedure, and can be relaxed: alternative, and more general retrieval methods should therefore be investigated. This is particularly important in the synchrotron implementation, where the diffracted beam profile can significantly vary from a Gaussian function. Concerning the laboratory implementation, different geometries, allowing the use of "standard", non micro-focal, sources should be studied. This should allow a substantial reduction in exposure time, due to the much greater flux available, thus making for example laboratory based CT implementations simpler and faster. In both configurations, refined optimisation of the experimental parameters (such as propagation distances, mask period and aperture size) should be pursued. Finally, the possibility of using iterative reconstruction algorithm for beam tracking CT should be investigated.

Future studies on one dimensional ptychography should be focused on the convergence properties of the algorithm, and in particular on how this is affected by parameters such as scan geometry, degree of overlap between probe positions, and degree of inhomogeneity of the probe. At the same time, a direct comparison of 1D-PIE with the more conventional far-field approach of ptychography and with its recently presented near-field implementation should be conducted, to understand its potential advantages and disadvantages. 1D-PIE would also benefit from a detailed study of the optimization of the experimental setup, which would enable understanding how parameters such as propagation distance, slit aperture size, and detector pixel size affect the method's performances. Finally, the CT implementation of 1D-PIE, together with its advantages and disadvantages with respect to similar techniques, should be investigated.

References

[1] P. R. T. Munro, K. Ignatyev, R. D. Speller, and A. Olivo. **The relationship between wave and geometrical optics model of coded aperture type x-ray phase contrast imaging systems**. *Opt. Express*, **18**:4103–4117, 2010. 13, 14, 61, 72, 73, 76

[2] H. H. Wen, E. E. Bennett, R. Kopace, A. F. Stein, and V. Pai. **Single-shot x-ray differential phase-contrast and diffraction imaging using two-dimensional transmission gratings**. *Opt. Lett.*, **35**:1932–1934, 2010. 16, 84, 101, 106, 108

[3] D. M. Paganin. *Coherent X-ray Optics*. Oxford University Press, 2006. 25, 26, 31, 38, 48, 49

[4] J. W. Goodman. *Introduction to Fourier Optics*. McGraw-Hill, 1996. 25

[5] M. Born and E. Wolf. *Principles of Optics*. Pergamon Press, 1980. 25

[6] F. Zernike. **How I discovered phase contrast**. *Science*, **121**:345–349, 1955. 41

[7] M. Pluta. **Nomarski's DIC microscopy: a review**. *Proc. SPIE*, **1846**:10–25, 1994. 41

[8] G. Morrison, W.J. Eaton, R. Barrett, and P. Charalambous. **STXM imaging with a configured detector**. *J. Phys. IV France*, **104**:529–534, 2003. 41

[9] M. Feser, C. Jacobsen, P. Rehak, and G. DeGeronimo. **Scanning transmission X-ray microscopy with a segmented detector**. *J. Phys. IV France*, **104**:529–534, 2003. 41

[10] A. Gianoncelli, G. R. Morrison, B. Kaulich, D. Bacescu, and J. Kovac. **Scanning transmission x-ray microscopy with a configurable detector**. *Appl. Phys. Lett.*, **89**:251117, 2006. 41

[11] A. Menzel, C. M. Kewish, M. Dierolf, P. Thibault, P. Kraft, O. Bunk, K. Jefimovs, C. David, and F. Pfeiffer. **Hard X-ray scanning transmission microscopy with a 2D pixel array detector**. *J. Phys.: Conf. Ser.*, **186**:012054, 2009. 41

[12] B. Kaulich, P. Thibault, A. Gianoncelli, and M. Kiskinova. **Transmission and emission x-ray microscopy: operation modes, contrast mechanisms and applications**. *J. Phys.: Condens. Matter*, **23**:083002, 2011. 41

[13] A. Snigirev, I. Snigireva, V. Kohn, S. Kuznetsov, and I. Schelokov. **On the possibilities of x-ray phase contrast microimaging by coherent high-energy synchrotron radiation**. *Rev. Sci. Instrum.*, **66**:5486–5492, 1995. 45

[14] S. W. Wilkins, T. E. Gureyev, D. Gao, A. Pogany, and Stevenson A. W. **Phase-contrast imaging using polychromatic hard x-rays**. *Nature*, **384**:335–338, 1996. 45

[15] D. Paganin and K. A. Nugent. **Noninterferometric Phase Imaging with Partially Coherent Light**. *Phys. Rev. Lett.*, **80**:2586–2589, 1998. 45

[16] P. Cloetens, W. Ludwig, J. Baruchel, D. V. Dyck, J. V. Landuyt, J. P. Guigay, and M. Schlenker. **Holotomography: Quantitative phase tomography with micrometer resolution using hard synchrotron radiation x rays**. *Appl. Phys. Lett.*, **75**:2912–2914, 1999. 45

[17] D. Paganin, S. C. Mayo, T. E. Gureyev, P. R. Miller, and S. W. Wilkins. **Simultaneous phase and amplitude extraction from a single defocused image of a homogeneous object**. *J. Microsc.*, **206**:33–40, 2002. 45

[18] T. E. Gureyev, A. Pogany, D. M. Paganin, and S. W. Wilkins. **Linear algorithms for phase retrieval in the Fresnel region**. *Opt. Commun*, **231**:53–70, 2004. 45

[19] C. David, B. Nohammer, H. H. Solak, and E. Ziegler. **Differential x-ray phase contrast imaging using a shearing interferometer**. *Appl. Phys. Lett.*, **81**:3287–3289, 2002. 47

[20] A. Momose, S. Kawamoto, I. Koyama, Y. Hamaishi, K. Takai, and Y. Suzuki. **Demonstration of x-ray Talbot interferometry**. *Jpn. J. Appl. Phys.*, **42**:L866–L868, 2003. 48

[21] F. Pfeiffer, T. Weitkamp, O. Bunk, and C. David. **Phase retrieval and differential phase-contrast imaging with low-brilliance x-ray sources**. *Nat. Phys.*, **2**:258–261, 2006. 48

[22] E. Förster, K. Goetz, and P. Zaumseil. **Double crystal diffractometry for the characterization of targets for laser fusion experiments**. *Krist. Tech.*, **15**:937945, 1980. 51

[23] T. J. Davis, D. Gao, T. E. Gureyev, A. W. Stevenson, and S. W. Wilkins. **Phase-contrast imaging of weakly absorbing materials using hard X-rays**. *Nature*, **373**:595–598, 1995. 51

[24] D. Chapman, W. Thomlinson, R. E. Johnston, E. Washburn, D. ans Pisano, N. Gmür, Z. Zhong, R. Menk, F. Arfelli, and D. Sayers. **Diffraction enhanced x-ray imaging**. *Phys. Med. Biol.*, **42**:2015–2025, 1997. 51

[25] A. Olivo, F. Arfelli, G. Cantatore, R. Longo, R. H. Menk, S. Pani, M. Prest, P. Poropat, L. Rigon, G. Tromba, E. Vallazza, and E. Castelli. **An innovative digital imaging set–up allowing a low–dose approach to phase contrast applications in the medical field**. *Med. Phys.*, **28**:1610–1619, 2001. 53, 84

[26] A. Olivo and R. Speller. **A coded-aperture approach allowing x–ray phase contrast imaging with conventional sources**. *Appl. Phys. Lett.*, **91**:074106, 2007. 53

[27] P. R. T. Munro, C. K. Hagen, M. B. Szafraniec, and A. Olivo. **A simplified approach to quantitative coded aperture X-ray phase imaging**. *Opt. Express*, **21**:11187–11201, 2013. 53, 75, 76, 79, 84

[28] P. C. Diemoz, C. K. Hagen, M. Endrizzi, and A. Olivo. **Sensitivity of laboratory based implementations of edge illumination X-ray phase-contrast imaging**. *Appl. Phys. Lett.*, **103**:244104, 2013. 53, 79, 84

[29] P. R. T. Munro, K. Ignatyev, R. D. Speller, and A. Olivo. **Source size and temporal coherence requirements of coded aperture type x-ray phase contrast imaging system**. *Opt. Express*, **18**:19681–19692, 2010. 53, 94

[30] M. Endrizzi, F. A. Vittoria, G. Kallon, D. Basta, P. C. Diemoz, A. Vincenzi, P. Delogu, R. Bellazzini, and A. Olivo. **Achromatic approach to phase-based multi-modal imaging with conventional X-ray sources**. *Opt. Express*, **23**:16473–16480, 2015. 53

[31] J. R. Fienup. **Reconstruction and synthesis applications of an iterative algorithm**. *Proc. SPIE*, **0373**:147–160, 1984. 55

[32] M. S. Smyth and J. H. J. Martin. **X ray crystallography**. *Mol. Pathol.*, **53**:8–14, 2000. 55

[33] J. R. Fienup. **Phase retrieval algorithms: a comparison**. *Appl. Opt.*, **21**:2758–2769, 1982. 56, 126

[34] S. Marchesini. **Invited Article: A unified evaluation of iterative projection algorithms for phase retrieval**. *Rev. Sci. Instrum.*, **78**:011301, 2007. 56, 126

[35] P. Thibault, M. Dierolf, O. Bunk, A. Menzel, and F. Pfeiffer. **Probe retrieval in ptychographic coherent diffractive imaging**. *Ultramicroscopy*, **109**:338–343, 2009. 56, 126

[36] A. M. Maiden and J. M. Rodenburg. **An improved ptychographical phase retrieval algorithm**. *Ultramicroscopy*, **109**:1256–1262, 2009. 56, 126, 131, 135

[37] Y. Takahashi, Y. Nishino, R. Tsutsumi, N. Zettsu, E. Matsubara, K. Yamauchi, and T. Ishikawa. **High-resolution projection image reconstruction of thick objects by hard x-ray diffraction microscopy**. *Phys. Rev. B*, **82**:214102, 2010. 57

[38] M. Dierolf, A. Menzel, P. Thibault, P. Schneider, C. M. Kewish, R. Wepf, O. Bunk, and F. Pfeiffer. **Ptychographic X-ray computed tomography at the nanoscale**. *Nature*, **467**:436–439, 2010. 57

[39] M. Guizar-Sicairos, A. Diaz, M. Holler, M. S. Lucas, A. Menzel, R. A. Wepf, and O. Bunk. **Phase tomography from x-ray coherent diffractive imaging projections**. *Opt. Express*, **19**:21345–21357, 2011. 57

[40] M. W. M. Jones, G. A. van Riessen, B. Abbey, C. T. Putkunz, M. D. Junker, E. Balaur, D. J. Vine, I. McNulty, B. Chen, B. D. Arhatari, S. Frankland, K. A. Nugent, L. Tilley, and A. G. Peele. **Whole-cell phase contrast imaging at the nanoscale using Fresnel Coherent Diffractive Imaging Tomography**. *Sci. Rep.*, **3**:2288, 2013. 57

[41] S. Cipiccia, F. A. Vittoria, M. Weikum, A. Olivo, and D. A. Jaroszynski. **Inclusion of coherence in Monte Carlo models for simulation of x-ray phase contrast imaging**. *Opt. Express*, **22**:23480–23488, 2014. 59

[42] F. A. Vittoria, P. C. Diemoz, M. Endrizzi, L. Rigon, F. C. Lopez, D. Dreossi, P. R. T. Munro, and A. Olivo. **Strategies for efficient and fast wave optics simulation of coded-aperture and other phase-contrast imaging methods**. *Appl. Opt.*, **52**:6940–6947, 2013. 59

[43] A. V. Oppenheim, R. W. Schafer, and J. R. Buck. *Discrete-Time Signal Processing*. Prentice Hall, 1999. 64

[44] B. Henke, E. Gullikson, , and J. Davis. **X-Ray Interactions: Photoabsorption, Scattering, Transmission and Reflection at E = 50-30,000 eV, Z = 1-92**. *At. Data Nucl. Data Tables*, **54**:181–342, 1993. 75

[45] F. A. Vittoria, M. Endrizzi, P. C. Diemoz, U. H. Wagner, C. Rau, I. K. Robinson, and A. Olivo. **Virtual edge illumination and one dimensional beam tracking for absorption, refraction, and scattering retrieval**. *Appl. Phys. Lett.*, **104**:134102, 2014. 77, 94, 100

[46] P. C. Diemoz, M. Endrizzi, C. E. Zapata, Z. D. Pesic, C. Rau, A. Bravin, I. K. Robinson, and A. Olivo. **X-ray phase-contrast imaging with nanoradian angular resolution**. *Phys. Rev. Lett.*, **110**:138105, 2013. 79, 83, 84

[47] M. Endrizzi, P. C. Diemoz, T. P. Millard, J. Louise Jones, R. D. Speller, I. K. Robinson, and A. Olivo. **Hard X-ray dark-field imaging with incoherent sample illumination**. *Appl. Phys. Lett.*, **104**:024106, 2014. 80, 85, 100, 105

[48] C. Rau, U. Wagner, Z. Pešić, and A. De Fanis. **Coherent imaging at the Diamond beamline I13**. *Phys. Status Solidi A*, **208**:2522–2525, 2011. 82, 119, 136

[49] S. W. Wilkins. *Improved x-ray optics, especially for phase contrast imaging.* WO 1995005725 A1, 1995. 84

[50] F. Krejci, J. Jakubek, and M. Kroupa. **Single grating method for low dose 1-D and 2-D phase contrast X-ray imaging**. *J. Instrum.*, **6**:C01073, 2011. 84, 101

[51] K. S. Morgan, D. M. Paganin, and K. K. W. Siu. **X-ray phase imaging with a paper analyzer**. *App. Phys. Lett.*, **100**:124102, 2012. 84, 100, 122

[52] S. Bérujon, E. Ziegler, R. Cerbino, and L. Peverini. **Two-dimensional x-ray beam phase sensing**. *Phys. Rev. Lett.*, **108**:158102, 2012. 84, 100

[53] K. S. Morgan, P. Modregger, S. C. Irvine, S. Rutishauser, V. A. Guzenko, M. Stampanoni, and C. David. **A sensitive x-ray phase contrast technique for rapid imaging using a single phase grid analyzer**. *Opt. Lett.*, **38**:4605–4608, 2013. 84, 100

[54] I. Zanette, T. Zhou, A. Burvall, U. Lundström, D. H. Larsson, M. Zdora, P. Thibault, F. Pfeiffer, and H. M. Hertz. **Speckle-based x-ray phase-contrast and dark-field imaging with a laboratory source**. *Phys. Rev. Lett.*, **112**:253903, 2014. 84, 100, 122

[55] F. A. Vittoria, G. K. N. Kallon, D. Basta, P. C. Diemoz, I. K. Robinson, A. Olivo, and M. Endrizzi. **Beam tracking approach for single-shot retrieval of absorption, refraction and dark-field signals with laboratory x-ray sources**. *App. Phys. Lett.*, **106**:224102, 2015. 90, 124

[56] V. E. Cosslett. **X-ray microscopy**. *Rev. Prog. Phys.*, **28**:381, 1965. 91

[57] D. Basta, M. Endrizzi, F. A. Vittoria, G. K. N. Kallon, T. P. M. Millard, P. C. Diemoz, and A. Olivo. **Note: Design and realization of a portable edge illumination X-ray phase contrast imaging system**. *Rev. Sci. Instrum.*, **86**:096102, 2015. 93

[58] F. Pfeiffer, M. Bech, O. Bunk, P. Kraft, E. F. Eikenberry, C. Brönnimann, C. Grünzweig, and C. David. **Hard-X-ray dark-field imaging using a grating interferometer**. *Nat. Mater.*, **7**:134, 2008. 105

[59] P. C. Diemoz, F. A. Vittoria, and A. Olivo. **Spatial resolution of edge illumination X-ray phase-contrast imaging**. *Opt. Express*, **22**:15514–15529, 2014. 105

[60] M. Endrizzi, F. A. Vittoria, P. C. Diemoz, R. Lorenzo, R. D. Speller, U. H. Wagner, R. Christoph, I. K. Robinson, and A. Olivo. **Phase-contrast microscopy at high x-ray energy with a laboratory setup**. *Opt. Lett.*, **39**:3332–3335, 2014. 105

[61] F. A. Vittoria, M. Endrizzi, P. C. Diemoz, A. Zamir, U. H. Wagner, C. Rau, I. K. Robinson, and A. Olivo. **X-ray absorption, phase and dark-field tomography through a beam tracking approach**. *Sci. Rep.*, **5**:16318, 2015. 113

[62] F. Natterer. *The Mathematics of Computerized Tomography.* Teubner, 1986. 113

[63] A. Kak and M. Slaney. *The Principles of Computerized Tomography.* Society for Industrial and Applied Mathematics USA, 1987. 113

[64] T. Feeman. *The Mathematics of Medical Imaging.* Springer, 2010. 113

[65] G. W. Faris and R. L. Byer. **Three-dimensional beam-deflection optical tomography of a supersonic jet**. *Appl. Opt.*, **27**:5202–5212, 1988. 118

[66] F. Pfeiffer, C. Kottler, O. Bunk, and C. David. **Hard x-ray phase tomography with low-brilliance sources**. *Phys. Rev. Lett.*, **98**:108105, 2007. 118

[67] L. Rigon, A. Astolfo, F. Arfelli, and R. Menk. **Generalized diffraction enhanced imaging: Application to tomography**. *Eur. J. Radiol.*, **68S**:S3–S7, 2008. 118

[68] F. A. Vittoria, P. C. Diemoz, M. Endrizzi, L. De Caro, U. H. Wanger, C. Rau, I. K. Robinson, and A. Olivo. **Phase retrieval through a one-dimensional ptychographic engine**. *Opt. Express*, **22**:17281–17291, 2014. 126

[69] V. Elser. **Phase retrieval by iterated projections**. *J. Opt. Soc. Am. A*, **20**:40–55, 2003. 126

[70] B. Abbey, K. A. Nugent, G. J. Williams, J. N. Clark, A. G. Peele, M. A. Pfeifer, M. de Jonge, and I. McNulty. **Keyhole coherent diffractive imaging**. *Nat. Phys.*, **4**:394–398, 2008. 126

[71] M. Stockmar, P. Cloetens, I. Zanette, B. Enders, M. Dierolf, F. Pfeiffer, and P. Thibault. **Near-field ptychography: phase retrieval for inline holography using a structured illumination**. *Sci. Rep.*, **3**:1927, 2013. 127, 130, 135

[72] J. D. Schmidt. *Numerical Simulation of Optical Wave Propagation with Examples in MATLAB*. SPIE Press, 2010. 130

[73] M. Guizar-Sicairos, M. Holler, A. Diaz, J. Vila-Comamala, O. Bunk, and A. Menzel. **Role of the illumination spatial-frequency spectrum for ptychography**. *Phys. Rev. B*, **86**:100103(R), 2012. 135

[74] F. Zhang, I. Peterson, J. Vila-Comamala, A. Diaz, F. Berenguer, R. Bean, B. Chen, A. Menzel, I. K. Robinson, and J. M. Rodenburg. **Translation position determination in ptychographic coherent diffraction imaging**. *Opt. Express*, **21**:13592–13606, 2013. 141

[75] N. Banterle, K. Huy Bui, E. A. Lemke, and M. Beck. **Fourier ring correlation as a resolution criterion for super–resolution microscopy**. *J. Struct. Biol.*, **183**:363–367, 2013. 142